

Universidade do Minho
Escola de Engenharia

Maria do Carmo Braga da Cruz Guimarães

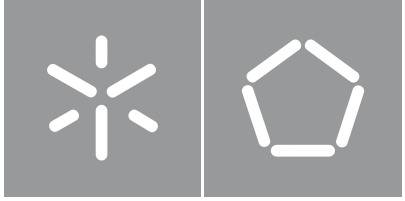
Development of a 3D *in vitro* bioprinted spheroid model to study the foreign body reaction

june 2026

Development of a 3D *in vitro* bioprinted spheroid model to study the foreign body reaction

Maria do Carmo Braga da Cruz Guimarães

UMinho | 2026



Universidade do Minho
Escola de Engenharia

Maria do Carmo Braga da Cruz Guimarães

Development of a 3D *in vitro* bioprinted spheroid model to study the foreign body reaction

Master's Dissertation
Biomedical Engineering
Clinical Engineering

Dissertation supervised by
Professor Dr. Lígia Rodrigues
Professor Dr. Theo van Kooten

june 2026

Copyright and Terms of Use for Third Party Work

This dissertation reports on academic work that can be used by third parties as long as the internationally accepted standards and good practices are respected concerning copyright and related rights.

This work can thereafter be used under the terms established in the license below.

Readers needing authorization conditions not provided for in the indicated licensing should contact the author through the RepositóriUM of the University of Minho.

License granted to users of this work:



CC BY-NC-ND

`https://creativecommons.org/licenses/by-nc-nd/4.0/`

Acknowledgements

I would like to express my sincere gratitude to the University of Minho and the University of Groningen for providing the academic environment and resources essential to this research.

A special thank you to the Biomaterial and Biomedical Technology group at the University of Groningen for welcoming me into such an inspiring atmosphere for scientific growth. I am deeply grateful to my daily supervisor, Liliana Agresti, for her unwavering support, patience, and invaluable guidance through every stage of this project.

I also wish to thank my supervisors, Professor Theo van Kooten and Professor Lígia Rodrigues. Their expertise, encouragement, and feedback were crucial to the realization of this research.

For my family, a heartfelt hug for your unwavering support and understanding throughout this journey.

Finally, to my childhood friends who set me on this path, to the friends I have made through every activity and project, and to my university friends who have become so much more than that — I am immensely grateful for each and every one of you. Every moment, every conversation, every laugh and every tear made it possible to get here, and for that, a simple thank you will never be enough.

According to *Dicionário Priberam da Língua Portuguesa*:

Obrigado

(*o·bri·ga·do*)

adjectivo

1. Que se sente devedor por ter sido alvo de uma atenção, de uma gentileza ou de um favor. = *AGRADECIDO, GRATO*

Statement of Integrity

I hereby declare having conducted this academic work with integrity. I confirm that I have not used plagiarism or any form of undue use of information or falsification of results along the process leading to its elaboration.

I further declare that I have fully acknowledged the Code of Ethical Conduct of the University of Minho.

University of Minho, Braga, june 2026

Maria do Carmo Braga da Cruz Guimarães

Assinado por: Maria do Carmo Braga da Cruz Guimarães
Num. de Identificação: BI14844951
Data: 17-06-2026 23:09:13 +01:00

CHAVE MÓVEL

Declaration on the use of artificial intelligence (AI) tools

I hereby declare having acted this academic work with integrity and confirm that I have not resorted to any form of undue use of AI tools, nor to the falsification or omission of information, sources, data, results or processes in any of the stages leading to its elaboration.

I further declare that any use of AI tools was done in a transparent and responsible manner, being duly noted in the work, and that I critically verified the accuracy of the content produced with their support, assuming full responsibility for what I submit.

I further declare that I have fully acknowledged the Code of Ethical Conduct of the University of Minho, as well as the applicable standards of academic integrity and data protection.

University of Minho, Braga, june 2026

Maria do Carmo Braga da Cruz Guimarães

Assinado por: Maria do Carmo Braga da Cruz Guimarães
Num. de Identificação: BI14844951
Data: 17-06-2026 23:10:19 +01:00

CHAVE MÓVEL

Resumo

Introdução: O aumento da esperança média de vida global levou a uma maior prevalência de condições degenerativas associadas à idade que exigem implantes de biomateriais. Isto intensificou a necessidade de modelos *in vitro* mais adequados para estudar a reação ao corpo estranho (foreign body reaction (FBR)). Atualmente, os modelos 2D convencionais não reproduzem a complexidade das interações célula-célula, enquanto que os modelos 3D ainda carecem de reprodutibilidade e relevância imunológica.

Objetivo: Este trabalho teve como objetivo desenvolver e otimizar um modelo *in vitro* 3D bioimpresso baseado em esferoides da linha celular monocítica humana (human monocytic cell line (THP-1)), tanto isoladamente como em co-cultura com fibroblastos dérmicos humanos primários (primary human dermal fibroblasts (HDF)), com o objetivo de estudar a FBR.

Métodos: Os esferoides de THP-1 foram produzidos em moldes de agarose não aderente e otimizados quanto à densidade celular, tamanho, morfologia e viabilidade. Os esferoides mistos de THP-1/HDF foram formados usando diferentes rácios de fibroblastos para macrófagos. Os esferoides foram incorporados em biotinta de gelatina metacrilada (gelatine methacrylate-based bioink (GelMA)) e bioimpressos em estruturas com geometria em grelha. A viabilidade celular e a integridade estrutural foram avaliadas por coloração *Live/Dead*, *DAPI* e análise com *Rhodamine/Phalloidin*.

Resultados e impacto: Os esferoides de THP-1 otimizados foram reprodutíveis, compactos e com diâmetro inferior a 200 μm, reduzindo o risco de formação de um núcleo necrótico. Quanto aos esferoides combinados, o rácio 16:1 de fibroblastos/macrófagos apresentou o melhor equilíbrio entre viabilidade, morfologia e integridade estrutural. Após a bioimpressão, os esferoides mantiveram-se viáveis e preservaram a sua arquitetura. Em conclusão, este modelo revelou-se uma plataforma promissora para reproduzir interações intercelulares relevantes para a FBR e para futuros estudos sobre biomateriais e a resposta inflamatória.

Palavras-chave Bioimpressão 3D, esferoides, modelos *in vitro* 3D, reação ao corpo estranho

Abstract

Background: Increased global life expectancy has led to a higher prevalence of age-related degenerative conditions that require biomaterial implants. This has intensified the need for better *in vitro* models to study the FBR. Conventional 2D models fail to reproduce the complexity of cell-cell interactions, while many 3D models still lack reproducibility and immune relevance.

Objective: This work aimed to develop and optimize a 3D bioprinted *in vitro* model based on THP-1 spheroids both alone and in co-culture with HDF, with the objective of studying the FBR.

Methods: THP-1 spheroids were produced in non-adhesive agarose molds and optimized for cell density, size, morphology, and viability. Mixed THP-1/HDF spheroids were formed using different fibroblast to macrophage ratios. The spheroids were embedded in GelMA and bioprinted into grid-shaped constructs. Cell viability and structural integrity were assessed by Live/Dead staining, DAPI, and Rhodamine/Phalloidin analysis.

Results and impact: The optimized THP-1 spheroids were reproducible, compact, and smaller than 200 µm, reducing the risk of necrotic core formation. Among the mixed spheroids, the 16:1 fibroblast/macrophage ratio provided the best balance of viability, morphology, and structural integrity. After bioprinting, the spheroids remained viable and preserved their architecture. In conclusion, this model proved to be a promising platform to reproduce intercellular interactions relevant to FBR and for future studies on biomaterials and inflammatory response.

Keywords 3D bioprinting, 3D *in vitro* models, foreign body reaction, spheroids

Contents

I Introduction **1**

General Introduction **2**

Motivation and problem statement . . . 2

Common cases of FBR . . . 3

Problem statement . . . 6

Goals and research questions . . . 6

Contribution to knowledge . . . 7

MsC thesis outline . . . 7

Tasks . . . 8

Schedule . . . 8

State of the Art **9**

Foreign body reaction . . . 9

Macrophages and fibroblasts . . . 13

3D *in vitro* models . . . 16

Organ-on-a-chip . . . 17

Organoids . . . 20

Scaffold- based 3D culture . . . 21

Spheroids models . . . 23

3D Bioprinting . . . 29

Bioprinting methods . . . 29

Bioink . . . 33

Overview of 3D bioprinted models . . . 40

Methods **42**

THP-1 cell culture . . . 42

HDF cell culture 42
Spheroids formation 43
3D Bioprinting 45
Live/Dead assay 46
DAPI and Rhodamine/Phalloidin staining 47
Fluorescence and confocal microscopy 47
Statistical analysis 48

Results **49**

THP-1 spheroids optimization 49
THP-1 spheroid structural integrity and morphological analysis 51
Bioprinting 54
THP-1 and HDF combined spheroids development 58
THP-1 and HDF spheroids structural integrity and morphological analysis 59
Viability assay of THP-1 and HDF combined spheroids 62

Discussion **64**

THP-1 spheroids 64
Good printability of spheroids 66
Combined spheroids 67
Study limitations 68

Conclusions and suggestions for further research **70**

List of Figures

Figure 1: Global distribution of the population aged 65 and older 2
Figure 2: Ten most common chronic health condition 3
Figure 3: Pacemakers implantations 4
Figure 4: Total hip arthroplasty and total knee arthroplasty procedures distributed by age . . . 5
Figure 5: Phases of the FBR 9
Figure 6: Macrophage maturation 11
Figure 7: Monocyte maturation and functions of the macrophage 13
Figure 8: Different functions of fibroblasts 14
Figure 9: Fibroblasts, macrophages and the foreign body 15
Figure 10: Organ-on-a-chip system 18
Figure 11: Multi-organ-on-chip platform 19
Figure 12: Development of organoid models 20
Figure 13: Biomedical applications of organoid models 21
Figure 14: Synthetic and natural scaffold-based 3D models 22
Figure 15: Scaffolds structures for tumour models 23
Figure 16: Hanging drop technique 24
Figure 17: Rotary cell culture technique 25
Figure 18: Magnetic levitation technique 26
Figure 19: Microfluidic system for spheroid development 26
Figure 20: Development of a non-adhesive hydrogel structure 27
Figure 21: Inkjet-base bioprinting 30
Figure 22: Laser-base bioprinting 31
Figure 23: Kenzan bioprinting 31
Figure 24: Biogripper bioprinting method 32
Figure 25: Extrusion-based bioprinting 33
Figure 26: Different types of crosslinking hydrogels 36

Figure 27: Printability index and pore geometry 37
Figure 28: Chemical composition of GelMA 39
Figure 29: THP-1 spheroids formation 44
Figure 30: Combined spheroids formation 45
Figure 31: Bioprinting process 46
Figure 32: Development and observation of spheroids of THP-1 49
Figure 33: Diameter comparison between spheroids of THP-1 with and without phorbol 12-myristate13-acetate (PMA) at different initial cellular seeding 50
Figure 34: Removal of the THP-1 spheroids 51
Figure 35: Diameter distribution of the spheroids of 0.5 million, 1 million and 2.5 million cells/mL cell densities with PMA 52
Figure 36: Solidity, compactness, and circularity evaluation for the groups with 0.5 million, 1 million and 2.5 million cells/mL cell densities and PMA, after removal 53
Figure 37: Bioprinting of THP-1 spheroids with tyramine-conjugated alginate granular ink and GelMA 54
Figure 38: Printability index of GelMA 55
Figure 39: Fluorescence imaging of the bioprinted constructs 55
Figure 40: Live/Dead assay of the printed THP-1 spheroids at day 1, 5 and 7 56
Figure 41: DAPI and Rhodamine/Phalloidin staining of the printed spheroids at day 1, 5 and 7 57
Figure 42: Development and observation of combined spheroids of THP-1 and HDF 58
Figure 43: Comparison of the diameters between combined spheroids of THP-1 and HDF developed with different ratios of fibroblasts and macrophages 58
Figure 44: Removal of combined spheroids of THP-1 and HDF 59
Figure 45: Diameter distribution of the combined spheroids of THP-1 and HDF for 8:1, 16:1 and 32:1 ratio 60
Figure 46: Solidity, compactness, and circularity analysis for the combined spheroids of THP-1 and HDF for 8:1, 16:1 and 32:1 ratio 61
Figure 47: Fluorescence imaging of the removed spheroids 62
Figure 48: Live/Dead assay of the combined spheroids after removal 62

List of Tables

Table 1: Activities Plan 8

Table 2: Advantages and limitations of 2D and 3D *in vitro* models. 17

Table 3: Advantages and limitations of different 3D *in vitro* models. 24

Acronyms

ASCs adult stem cells

DMEM-HG high-glucose dulbecco's modified eagle medium

ECM extracellular matrix

ESCs embryonic stem cells

FBGCs polynucleate foreign body giant cells

FBR foreign body reaction

FBS fetal bovine serum

GelMA gelatine methacrylate-based bioink

HA hyaluronic acid

HDF primary human dermal fibroblasts

hMSC human mesenchymal stromal cell

IMD implantable medical devices

iPSCs induced pluripotent stem cells

LAP lithium phenyl-2,4,6-trimethylbenzoylphosphinate

LPS lipopolysaccharide

M0 unpolarized macrophages

M1 proinflammatory macrophages

M2 anti-inflammatory macrophages

MAA methacrylic anhydride

OoC organ-on-a-chip

PBS phosphate-buffered saline

PCL polycaprolactone

PEG polyethylene glycol

Pen/Strep penicillin streptomycin

PFA paraformaldehyde

PLA poly(l-lactic) acid

PLGA poly(lactic-co-glycolic) acid

PMA phorbol 12-myristate13-acetate

Pr printability index

PVP polyvinylpyrrolidone

ROI region of interest

ROS reactive oxygen species

RPMI roswell park memorial institute

SD standard deviation

SoA state of the art

THA total hip arthroplasty

THP-1 human monocytic cell line

TKA total knee arthroplasty

XG xanthan gum

Part I
Introduction

Chapter 1
General Introduction

1.1 Motivation and problem statement

Nowadays, the advances in healthcare have led to an increase in the global life expectancy, resulting in a pronounced demographic shift. According to the US Census Bureau and National Institutes of Health, from 2015 to 2050 the percentage of population over 65 years is expected to double, becoming 16,7% of the world, as seen in Figure 1 [1].

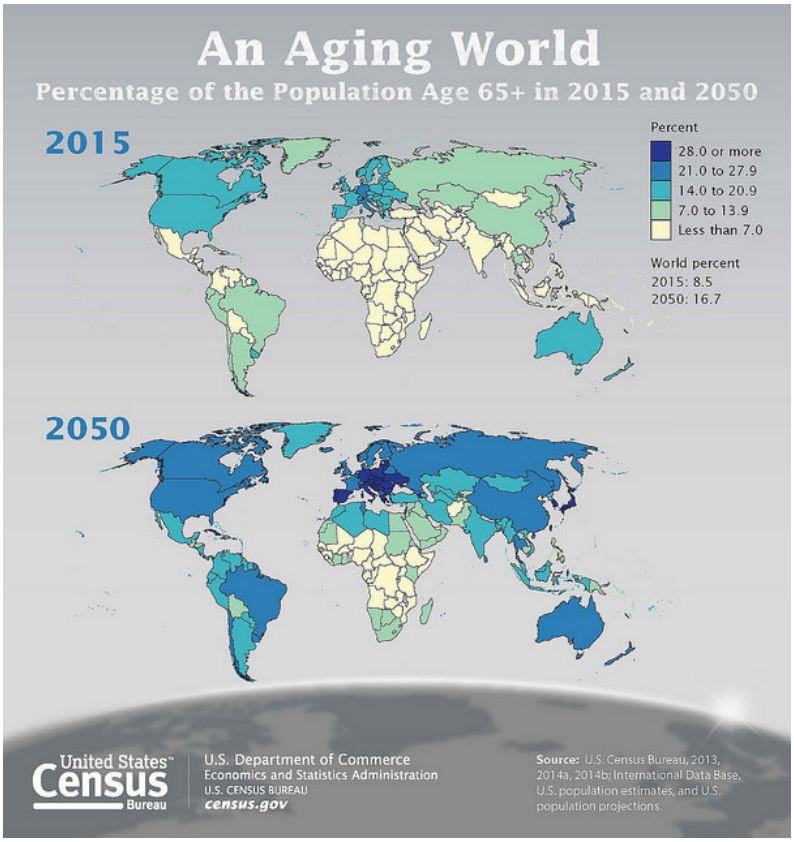


Figure 1: **Global distribution of the population aged 65 and older.**
Global distribution of the population aged 65 and older in 2015 (top) and projected for 2050 (bottom). Taken from [1].

This change escalates the prevalence of age-related degenerative conditions, including osteoarthritis

and chronic skeletal defects, affecting approximately 50% of the population over 65, cardiovascular diseases, affecting 60% of the elderly population, and diabetes, targeting 24% of them, among other chronic diseases, as portrait in Figure 2 [2].

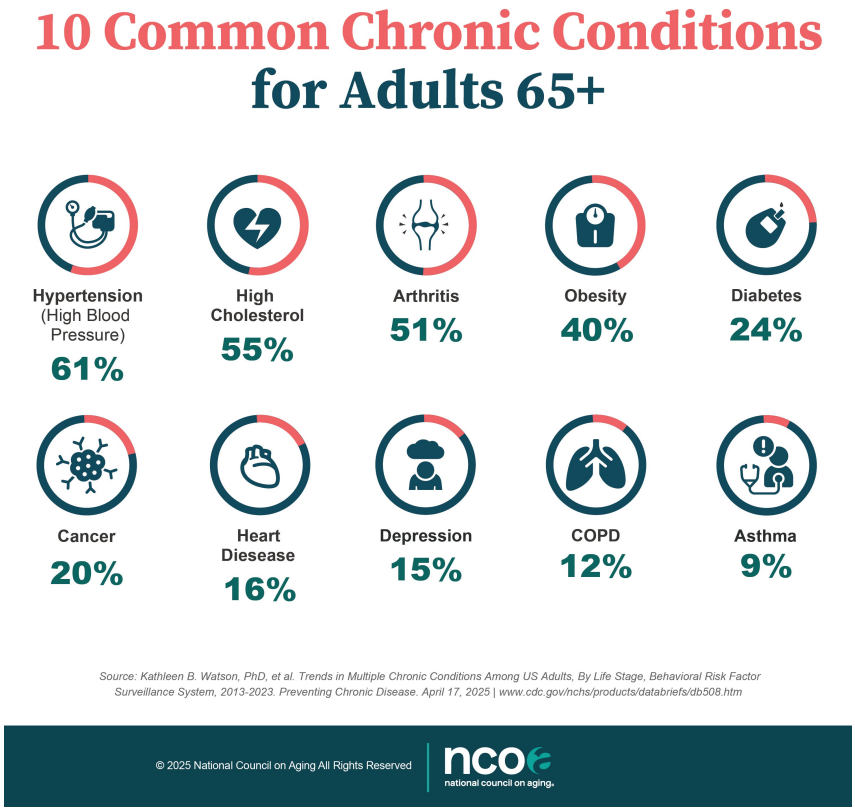


Figure 2: **Ten most common chronic health condition.**
Prevalence of the ten most common chronic health conditions among adults aged 65 and older. Hypertension is the most prevalent condition, affecting 61% of the demographic, followed by high cholesterol (55%) and arthritis (51%). Taken from [2].

Consequently, there is a significant and continuous demand for biomaterials intended for therapeutic purposes, such as joint replacements, bone fixation devices, insulin and cardiac devices and dental prostheses. These implants must ideally exhibit long-term reliability without provoking adverse biological reactions. However, this is not always the case since the implantation of foreign materials often precipitates the FBR [3, 4].

1.1.1 Common cases of FBR

Starting with cardiac devices, according to the European Society of Cardiology, in 2024, more than 900 pacemakers per million people were implanted in most European countries such as Portugal, Italy, France, and Sweden, as shown in Figure 3 [5].

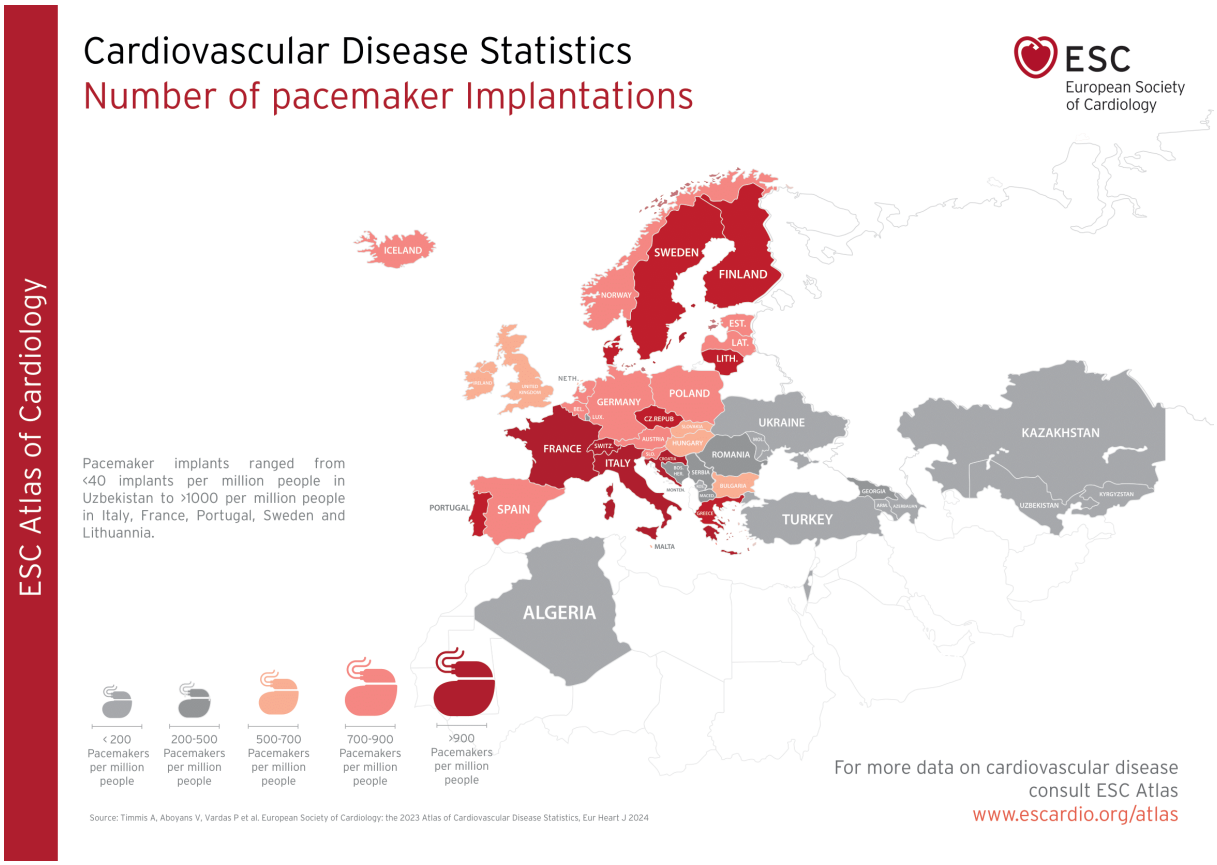


Figure 3: **Pacemakers implantations.**
Number of pacemakers implantations, in 2024, in Europe. Taken from [5].

Even though pacemakers and other implantable medical devices (IMD) are supposed to be biocompatible, there is a certain level of biocompatibility that is never truly reach. This means that despite the major need of these devices, the FBR and consequent fibrotic capsule formation lead to many health complications, such as following surgeries for removal of the implant, medication to avoid symptoms, among others [6].

The same thing applies to insulin pumps or devices used in diabetic patients. According to the World Health Organization, in 2022, 14% of adults aged 18 years and older were living with diabetes, an increase from 7% in 1990. This relates to the need of devices capable of controlling insulin levels (e.g. insulin pumps). However, these devices do not always move from the experimental phase into the *in vivo* trials due to the activation of the host immune response which results in implant failure [7, 8].

Regarding skeletal implants, these range from dental prosthetic treatments to hip or knee replacements, also known as arthroplasty. As shown in Figure 4A, total hip arthroplasty (THA) is predominantly performed in older age groups, with a peak distribution between approximately 60 and 75 years. The percentage values shown correspond to the relative distribution of procedures within each age group for this specific surgery type. The same can be seen in Figure 4B, regarding total knee arthroplasty (TKA), emphasizing

the importance of research within this area. It is also important to consider the occurrence of revision arthroplasties, which involve additional surgical procedures to replace or correct a previously implanted device. This underscores the need for improved preventive strategies, the management of implant-related complications, and the development of more durable and long-lasting implants [9–12].

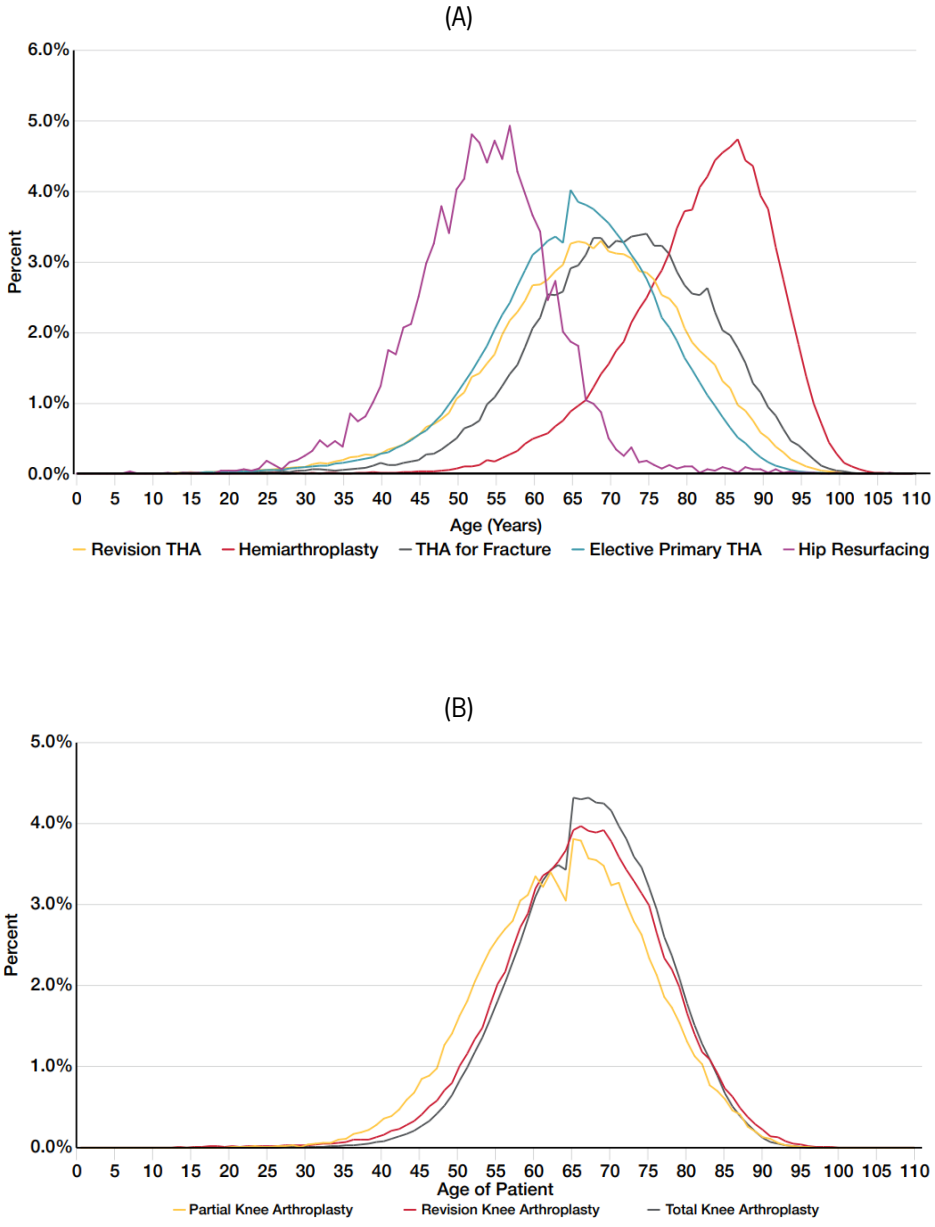


Figure 4: **THA and TKA procedures distributed by age.**
Percentage distribution of THA and TKA procedures reported in the American Joint Replacement Registry (2024). (A) Age distribution of THA procedures performed between 2012-2023 (N=1,533,846). (B) Age distribution of TKA procedures performed between 2012-2023 (N=2,181,469). Taken from [12]

Overall, from replacement implants to implantable medical devices, today's medicine is deeply connected to the use of biomaterials that have one crucial requirement, biocompatibility. This tricky aspect

leads to the need to develop proper structures capable of mimicking the human body reaction to these foreign materials. This must be done in the prospect of taking into consideration the FBR during the clinical research period to prevent health complications later on, get more accurate results, save resources and progress into more evolved and efficient technics [3, 13].

Despite the already existing *in vitro* models, those usually need a compromise between accessibility, physiological similarities, and handling difficulty. Due to these aspects, the importance of *in vitro* platforms more optimized and with 3D properties could be beneficial to a more in-depth analysis in this area of research [14].

1.1.2 Problem statement

Current 2D *in vitro* models, as promising as they sound, still carry a long list of disadvantages, such as lack of complexity in terms of replicating the tested environment, low capacity to accurately represent the efficacy of the drug or the adverse effects it has, inability to account for the production of extracellular matrix (ECM) and its impact on cell morphology and behavior and lack of cell-cell interactions. All these aspects profoundly affect the results and accuracy obtained [15, 16].

Due to these problems the need for an improved model has risen and influenced a novel approach, a 3D *in vitro* model. Still the 3D models have their own limitations, such as lack of reproducibility, complicate biofabrication procedures and strict regulatory frameworks [16].

Moreover, the exclusion of immune cells in most 3D *in vitro* platforms remains a significant limitation. This omission hinders the optimal replication of human physiology, since the immune system plays a major role in the pathophysiology of almost every disease and reaction to foreign bodies, know as the FBR. Therefore, it often leads to models that do not fully reflect the immune system [17].

1.2 Goals and research questions

Considering all the points made previously this project proposes the development of a new 3D structure with the goal of minimizing the problems and disadvantages illustrated beforehand.

In this way, the main goal is to combine spheroids with the bioprinting process. The aim is to create THP-1 only spheroids and combined THP-1 and HDF spheroids followed by the bioprinting of the spheroids with GelMA. Afterwords, the spheroids and cell viability must be analysed to guaranty that the model is a viable option.

Taking this into consideration the main questions of this project focus on the production of the spheroids in terms of cell density, the process of self-assembly, the reproducibility and sphericity of them. Furthermore,

the possibility of printing the spheroids without disaggregation is also important to assess and the viability of the cells after the process.

To reach more complex structures, is also fundamental to test if the formation of mixed spheroids (different cell types combined) is a possibility.

Overall, this study proposes a reproducible 3D bioprinted spheroid model that prioritizes intercellular crosstalk, particularly immune-related interactions, addressing a gap in conventional *in vitro* models regarding the FBR.

1.3 Contribution to knowledge

With the work re-laid in this project the main contributions meant to be achieved are:

- An academic review of the previous 3D models available at the moment and their advantages and disadvantages complemented by a detailed explanation of the different techniques used to achieve the final results.
- Production of reproducible, spherical and viable spheroids though a simple and optimized process though testing and data analysis.
- Bioprinting the spheroids in a sterile environment and taking into consideration the production, testing and optimization of this process and the final structure.
- Production of the mixed spheroids focusing on the optimization of the best cell densities.

1.4 MsC thesis outline

In terms of the outline planned for this Master Thesis, the second chapter will be focused on the state of the art (SoA), regarding the FBR and the cells involved in this process, overview of existing 2D and 3D models, with special focus on the formation of THP-1 and HDF spheroids, the diverse ways to obtain them and the ones already in use.

Moreover, the bioprinting will also be one of main subjects specially regarding different ways to bioprint, different materials possible to use and the models already made using GelMA.

In Chapters 3, 4, and 5, the methods, results, and discussion of the project are presented, respectively.

Finally, Chapter 6 is an overview of the conclusions and suggestions for future research.

1.5 Tasks

T1: Analysis of the SoA regarding FBR, *in vitro* models, spheroids formation and 3D bioprinting with the respective results. Experimental planning and organization regarding the tests, materials and preparations required. Outlining different hypotheses and plans accordingly.

T2: Starting the culture of the THP-1 cell line and production of the devices required for the spheroid formation. This step includes the seeding of the cells inside the devices and data collection during the growing period. Consequently, the evaluation of the integrity and cell viability, followed by adjustments to the different variables is also expected.

T3: Bioprinting of the spheroids using different bioinks. Moreover, the analysis of the cell viability after the printing is also required.

T4: Combination and optimization of two different cell types (THP-1 and HDF) in the spheroid production, followed by the analysis of the viability of both cell types after the removal. In this step the selection of the right proportions and procedure is the main goal.

T5: Analysis of the all the data collected.

T6: Writing the thesis.

1.6 Schedule

Table 1: **Activities Plan.**

Task	Sep	Oct	Nov	Dec	Jan	Feb	Mar	Apr	May	Jun
T1	●	●								
T2	●	●								
T3		●	●							
T4				●	●					
T5			●	●	●	●				
T6				●	●	●	●	●	●	●

Chapter 2
State of the Art

2.1 Foreign body reaction

The FBR is the name given to the human body cascade of reactions in response to a foreign body considered harmful for the organism. As shown in Figure 5 , it can be divided in 5 different phases: implantation, protein adsorption, macrophage adhesion and attack, matrix deposition and fibrous encapsulation [18].

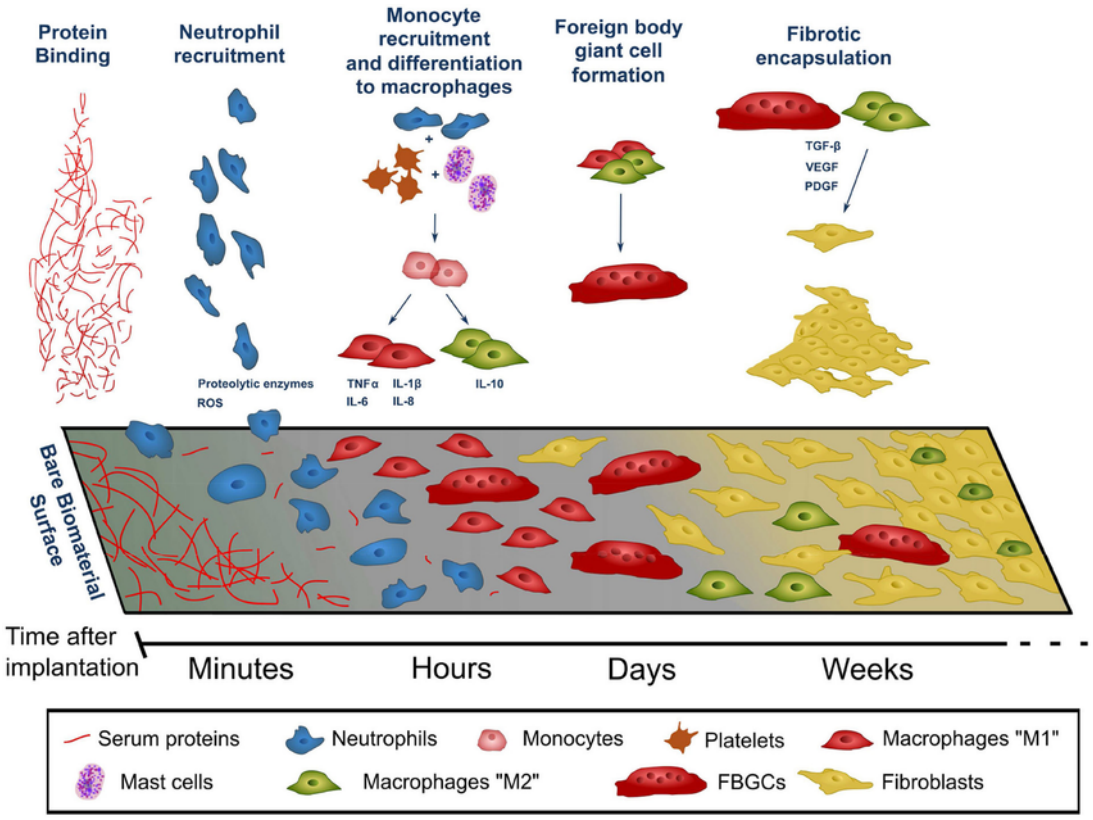


Figure 5: **Phases of the FBR.**
Phases from minutes to weeks of the FBR development. Taken from [4].

- **1st phase:** Blood and foreign body interaction

Firstly, there needs to be an interaction between cells of the immune system and the foreign body. This can occur during surgeries for implantation of medical devices, for example. In these cases, the direct implantation of the device will be registered by the body as a threat. Consequently, the immune cells are signalled to the location and start the immune response. Normally occurs within an hour of implantation and leads to the 2nd phase [4].

- **2nd phase:** Protein adsorption

From 30 minutes up to two days of interaction, the foreign body adsorbers proteins. These proteins, such as albumin and fibrinogen, are derived from extravasated blood and can become non-specifically adsorbed to the surface of the implant. This leads to the formation of a temporary matrix around the foreign body [4].

Throughout this step, the matrix is subjected to a dynamic process of adsorption and desorption of proteins, known as the Vroman effect, where smaller proteins are replaced by bigger proteins leading to the formation of a progressively more complex structure [4].

In addition, as first responders, neutrophils are immediately recruited to the site of implantation and adhere to the protein layer and release factors (such as reactive oxygen species (ROS) and proteolytic enzymes). These factors can recruit other immune cells, which leads to the progression of the immune reaction [4].

- **3rd phase:** macrophage adhesion and attack

Furthermore, due to both the neutrophils action and the thrombus formation, the body recognizes the difference in the connective tissue and begins the innate immunity response, in other words, initiates a series of inflammatory reactions. This leads to further development of the thrombus and, consequently, the recruitment of monocytes to the location [4].

The monocytes, because of cytokines, growth factors, and other bioactive agents within the provisional matrix, differentiate into macrophages. Nevertheless, the modulation of the macrophage activity is dependent on these components from the provisional matrix, which means that different foreign bodies, form different matrix leading to distinct monocytes differentiations [18, 19].

Regarding this, the macrophages, with their important role of inflammatory mediation, can either have a proinflammatory or anti-inflammatory effect depending on the differentiation that occurred, as relayed in Figure 6 [19, 20].

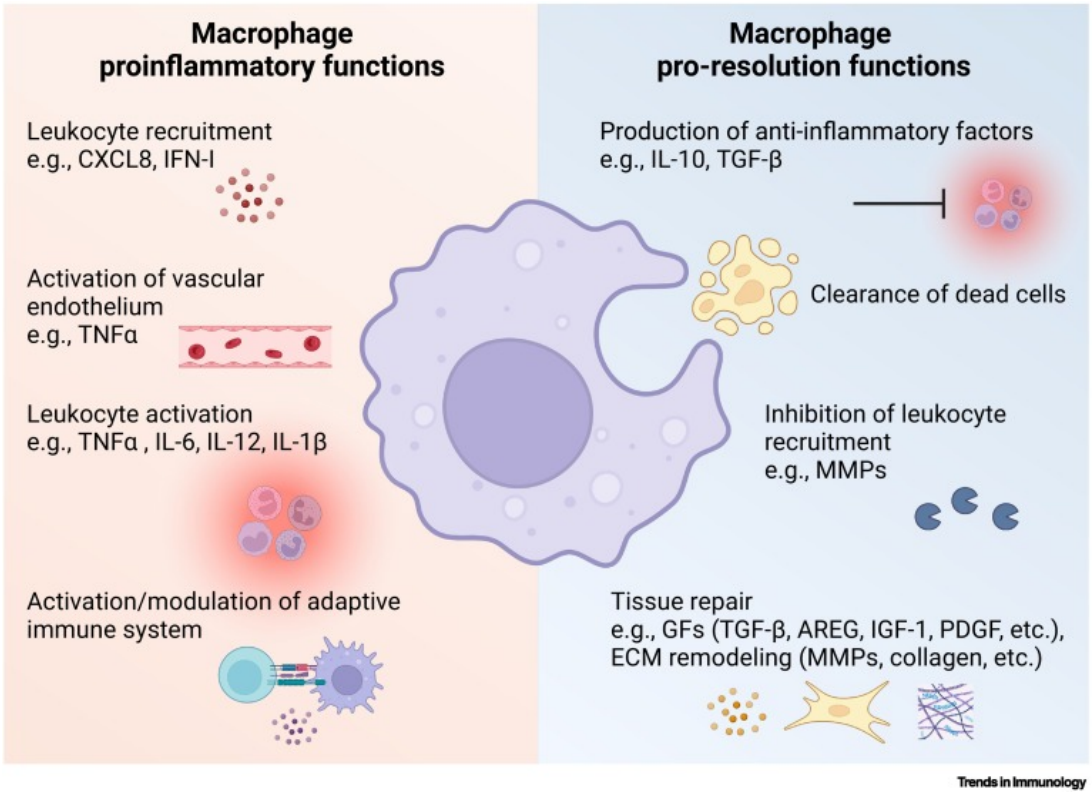


Figure 6: **Macrophage maturation.**
Macrophage maturation into proinflammatory macrophages (M1) and anti-inflammatory macrophages (M2) and their different functions. Taken from [21].

In this phase, when they are in contact with, for example, lipopolysaccharide (LPS) and interferon-γ (INF-γ) they differentiate into M1 leading to leukocyte activation and recruitment (production of IL-6, TNF-α, ROS and IL-12), hence furthering the proinflammatory process. However, further down the line they can differentiate into M2 anti-inflammatory polarization [19, 20].

In addition, the growing amount of plasma and extracellular matrix proteins on the surface of the foreign body allow for the macrophages to adhere to the surface, due to receptors such as integrins. Consequently, the macrophages undergo cytoskeletal remodeling, they progressively try to cover more of the surface by expanding podosomes as a way of engulfing the foreign body, known as phagocytosis [4, 19].

Afterwards, the macrophages can be successful and degrade the foreign body, allowing the reaction to diminish and eventually stop, but they might not be able to phagocyte or destroy the foreign body leading into a chronic stage of the FBR [4].

- **4rd phase:** Matrix deposition

When phagocytosis is not possible, the FBR is no longer just an acute inflammatory reaction but turns into chronic inflammation including fibrosis. One of the signs of the chronic inflammation is the transition

from M1 into M2, which are anti-inflammatory and responsible for repairing the tissue [4].

These phenotype transition happens as part of the wound healing process, where no longer is necessary to attack the foreign body but rather repair the damaged tissue, even if the inflammation is still present [4].

The transition happens in the presence of interleukins such as IL-4, IL-13 and T-helper 2 cells, that lead to the secretion of IL-10 and TGF-β (anti-inflammatory cytokines). These cytokines attract fibroblasts and activate them, leading to the transition from fibroblasts into myofibroblasts. The myofibroblasts have a complex of microfilaments acting as a contractile mechanism that enables these cells to generate force to the surrounding extracellular matrix. Consequently, adhesion to the surface is promoted and layers of ECM proteins are formed [18, 20, 22]

- **5th phase:** Fibrous encapsulation

In this last phase, the macrophages begin to merge forming polynucleate foreign body giant cells (FBGCs) around the surface of the implant, to be able to phagocyte bigger particles, this is known as frustrated phagocytosis [4, 19].

However, this fusion might not be always the case, since it doesn't depend just on the molecules present but also on surface characteristics, if it allows fusion or not, which means that the FBGCs formation is dependent on the surface of the foreign body [19].

In addition, the combination of the FBGCs, fibroblasts and proteins from the ECM results in the FBR capsule. This capsule is a new tissue, where new blood vessels develop and provide oxygen and nutrients to its entirety [4].

The new tissue, throughout the following weeks and then months, maintains cell proliferation and ECM, resulting in the augmentation of the capsule and further separation of the foreign body from the rest of the body. This, in most cases, is a negative consequence since it completely separates the implant from the body, compromising the implant function. On the other hand, in cases of drug delivery systems, such as subcutaneous hormonal implants, the FBR is taken into consideration in the development of the product. This means that the FBR is a necessity for the correct functioning of the implant. Overall, despite the possibility of taking the FBR into consideration and playing it in favour of the final product, it still is an undesirable reaction to implantation of medical devices [23].

2.2 Macrophages and fibroblasts

Regarding macrophages, as explained beforehand, they are considered innate immune cells. The monocytes are originated from pluripotent hematopoietic stem cell in the bone marrow and through maturation they reach the macrophage stage. The maturation process, also known as polarization, leads to different macrophages with distinct functions, as seen in Figure 7. This maturation can lead to M1 and M2 and unpolarized macrophages (M0), known as the precursors of M1 and M2 phenotypes. However, the maturation happens in a spectrum, so they cannot be evaluated in just 3 groups, but should be classified in terms of the prevalence of characteristics. This characterization can be made through known surface markers, which facilitate the assessment of the maturation process [24–26].

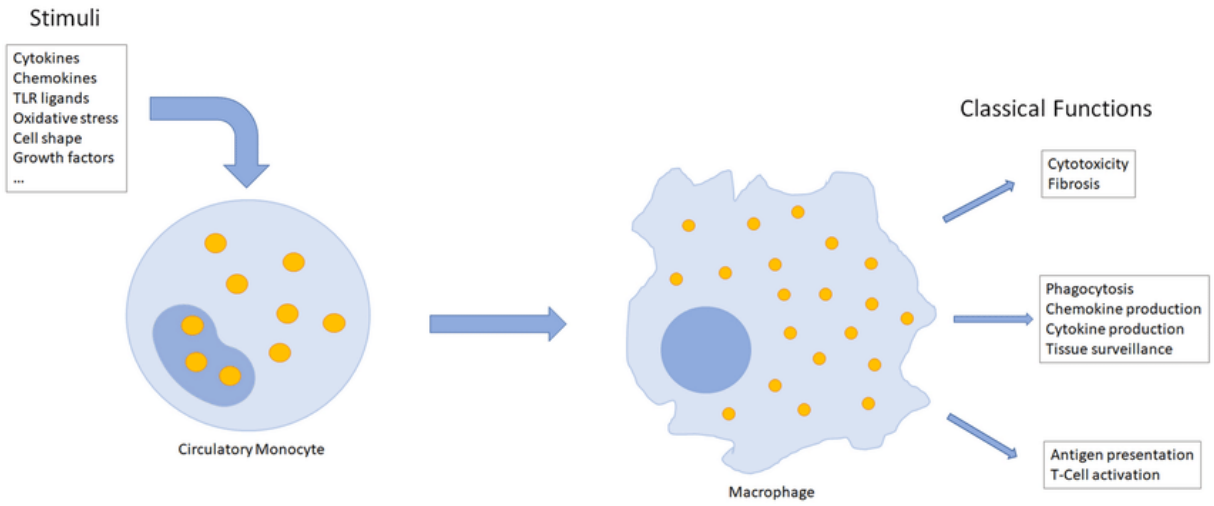


Figure 7: **Monocyte maturation and functions of the macrophage.**
Monocyte maturation into macrophages; different stimuli applied and functions of the macrophage. Taken from [25].

Moreover, the roles that macrophages populations have in phagocytosis, fibrosis, tissue repairing and regeneration, their significant presence in blood (monocytes correspond between 2% and 8% of the white blood cell count) and their high adaptability to different environments make them crucial cells in the immune reaction and, consequently, in the *in vitro* models that aim to replicate the human immune system [25].

However, since macrophages are harder to isolate and grow, it is common to use monocytic cell lines, such as THP-1, and induce the differenciation. In order to achieve this, PMA is normally used as an inducer of differentiation. PMA is a chemical compound similar to diacylglycerol, a molecule responsible for activating protein kinase C. Therefore, PMA activates the signalization cascade, altering the expression of macrophage specific markers, resulting in induced macrophages. This chemical can be used in different

concentrations, normally between 5 ng/mL and 200 ng/mL, and with different induction times (24h to 48h) [27].

In terms of fibroblasts, these are mesenchymal cells responsible for producing extracellular matrix (Figure 8A, C and F), consequently, signalling and activating neighbour cells (8B, G and H). They are also able to differentiate into different cells from the mesenchymal origin (8E).

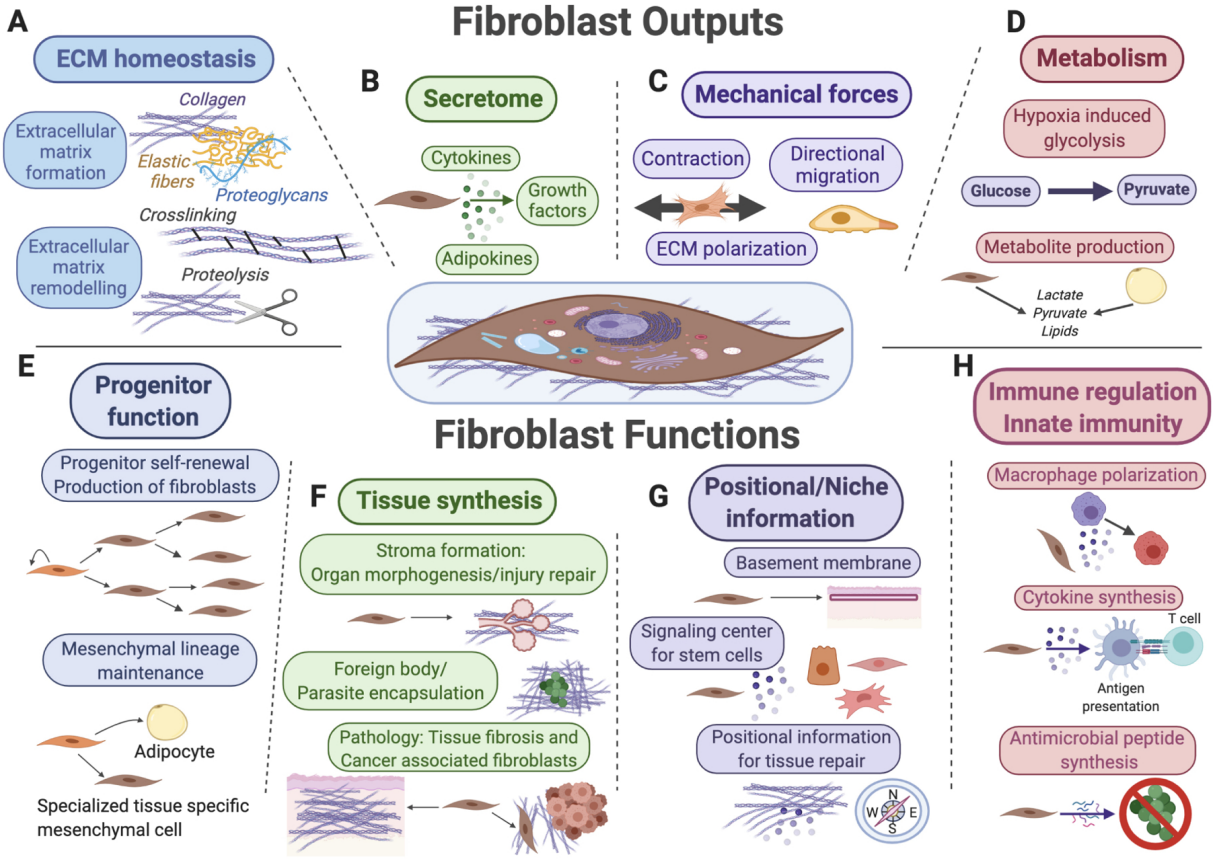


Figure 8: **Different functions of fibroblasts.**
Fibroblasts outputs and functions across the body. Taken from [28].

The ECM production starts with the deposition of collagen, proteoglycans, elastin, fibronectin, microfibrillar proteins and laminins. Afterwards, fibroblasts secret cytokines and growth factors (controlled by the ECM) responsible for signalling the body accordingly. However, the ECM is not a static structure, it is in constant change because of its surroundings and the fibroblast ability to regulate modifying enzymes [28].

Overall, the plasticity of both macrophages and fibroblasts make them susceptible to the environment they are inserted in. As depicted in Figure 9, the macrophages binding to difference surfaces lead to different fibroblasts reactions, due to distinct cytokines and, consequently, distinct fibroblast differentiation [26].

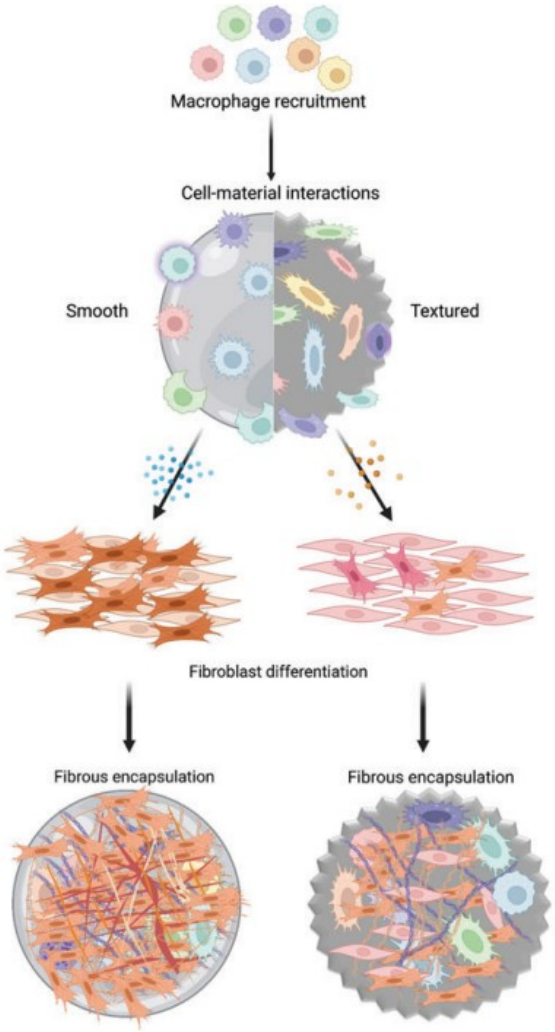


Figure 9: **Fibroblasts, macrophages and the foreign body.**
Effects on the fibroblast differentiation and response because of macrophages and the foreign body. Taken from [26].

This reveals that the FBR is affected by the characteristics of the implant (for example, its surface) and by the macrophages recruited. The macrophages can influence fibroblast migration and differentiation, leading to a different FBR. In addition, there is evidence *in vivo* that the relation between macrophages and fibroblasts influence the FBR which leads to the importance of the inclusion of both cell types in *in vitro* models [26].

2.3 3D *in vitro* models

Today's medical research relies deeply on the *in vitro* and *in vivo* models for either pharmacological test, specialized medicine, anticancer therapies and many other applications.

However, the use of animals, for *in vivo* testing, has raised concerns in ethical and sustainable matters. In Europe, the 3Rs legislation (replacement, reduction, refinement) aims to replace animals in the scientific field and protect their application, emphasizing the need to come up with different technologies capable of providing similar results, as the *in vitro* models [29, 30].

The 2D *in vitro* models are two-dimensional *in vitro* cell culture systems where the adherent cells grow on a flat surface (petri dishes, flasks, plates, to name some examples). These models have some advantages such as easier observation of the cells, high reproducibility, possible up-scaling, low complexity, good cost-effectiveness relation and easier screening and high-throughput evaluation. However, since they are 2D, the cells have a higher contact with the surface of culture flasks than with each other, which means the cell-cell interaction, the ECM formation and the blood and nutrient flow are neglected leading to models that lack physiological accuracy [31, 32].

Because of this, the development of 3D models has been on the rising. These models, characterized as "lab-grown biological structures that mimic human tissues more accurately than traditional 2D cultures", [33], are taking over the *in vitro* studies due to their ability to form complex 3D biological structures [34].

This allows them to take into consideration the cells interactions, ECM production and the diffusion gradients of oxygen, nutrients, blood and drugs, depending on the model. However, they still present some disadvantages, such as complex biofabrication procedures, lack of reproducibility, and strict regulatory frameworks [34].

Table 2: **Advantages and limitations of 2D and 3D *in vitro* models.**

Advantages (on the left) and limitations (on the right) of 2D and 3D *in vitro* models. Adapted from [16, 31–34]

	Advantages	**Limitations**
2D models	High reproducibility	Low cell-cell interactions
	Low complexity and possible up-scaling	Lack of ECM formation
	Easier observation, screening and high-throughput evaluation	Blood and nutrient flow are neglected
	Good cost-effectiveness relation	Lack of physiological accuracy
3D models	Complex 3D biological structures	Lack of reproducibility
	Relevant intercellular interactions and high ECM production	Complicated biofabrication procedures
	Possible diffusion gradients of oxygen, nutrients, blood and drugs	Strict regulatory frameworks

2.3.1 Organ-on-a-chip

The organ-on-a-chip (OoC) is a microfluidic device with promising biomedical applications. These platforms were adapted from computer microchips and engineered for cell and tissue culturing under dynamic conditions. Due to their microchannels, they allow better perfusion and fluidic control, which further them as a technology able to simulate *in vivo* settings while having the control and precision required *in vitro* [35].

These devices are able to control cell microenvironments and allow the user to guarantee the tissue-cells specific functions in any organ or tissue of the body. The applications cover human pathophysiology, cancer research and pharmacological therapeutics analysis (Figure 10) [35].

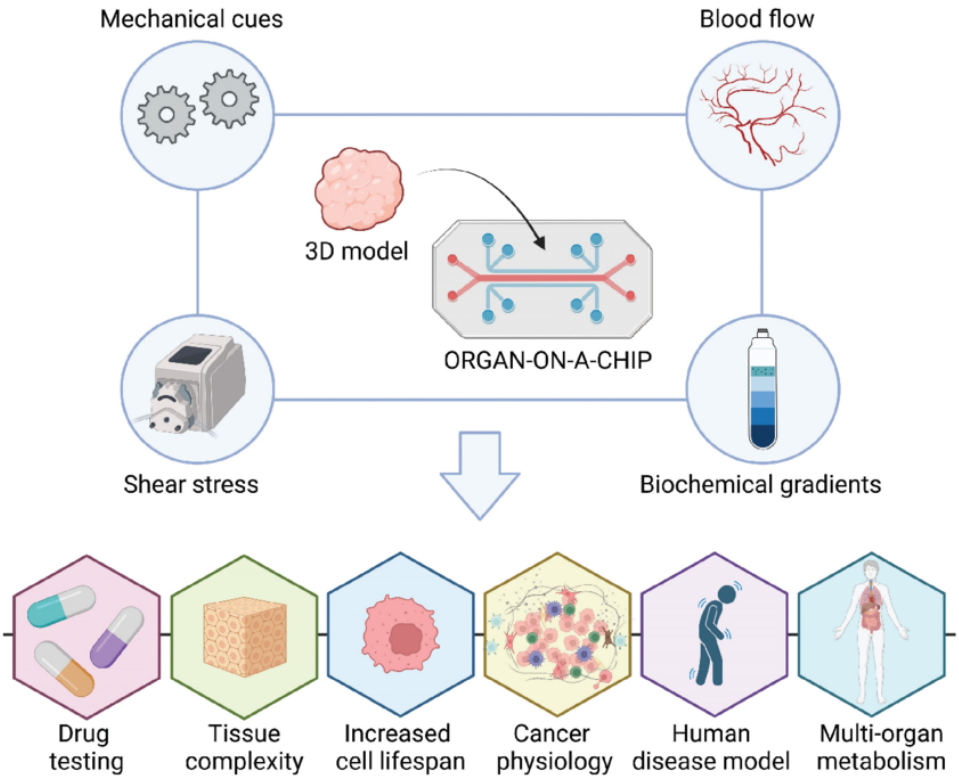


Figure 10: **Organ-on-a-chip system.**
Functioning and applications of an organ-on-a-chip system. Taken from [36].

One example of a big application of the organ on a chip is the case of the immunocompetent multi-organ-on-a-chip (multi-OoC). These structures, seen in Figure 11, are able to replicate the systemic immunological processes in an *in vitro* environment by not only mimeting different organs but by including immune cells in the development of each replicated organ. However, they are limited by the incomplete maturation status of the differentiated cells [17].

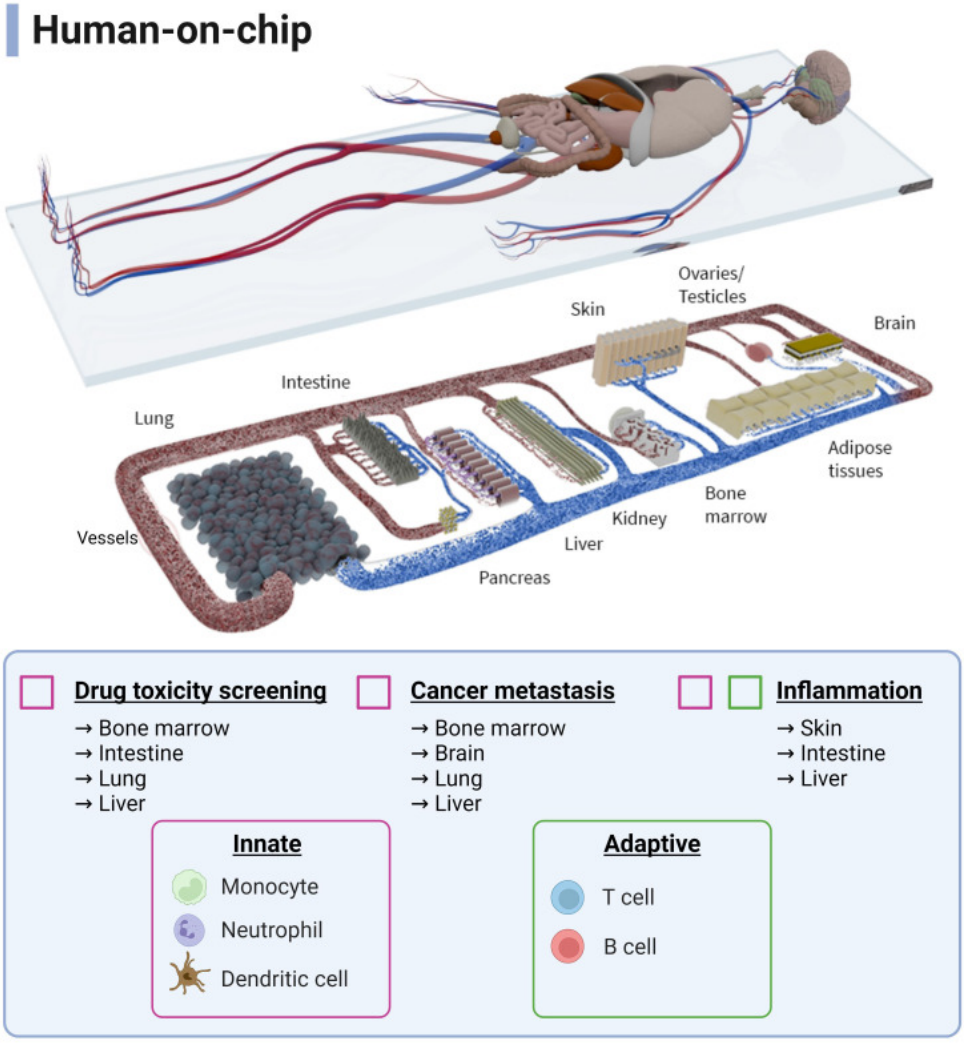


Figure 11: **Multi-organ-on-chip platform.**
Multi-organ-on-chip platform integrating vascular networks and immune system effectors (innate and adaptive) for advanced toxicological and pathological studies. Taken from [17].

Once more, this model is not without its disadvantages, the difficulty of use and costly electrical components of the OoC, allied with the complex development of these structures take them further away from general acceptance [35].

2.3.2 Organoids

The organoid 3D models, consists of a cluster of stem cells, with the ability to "self-organize and differentiate into functional cell types" [37]. They are cultured with either induced pluripotent stem cells (iPSCs), embryonic stem cells (ESCs), adult stem cells (ASCs) or cancer stem cells from healthy donors or patients, depending on the application. The cells then, through self-organization, a supporting ECM and signal factors, develop into complex tissues and organoids, as shown in Figure 12 [38].

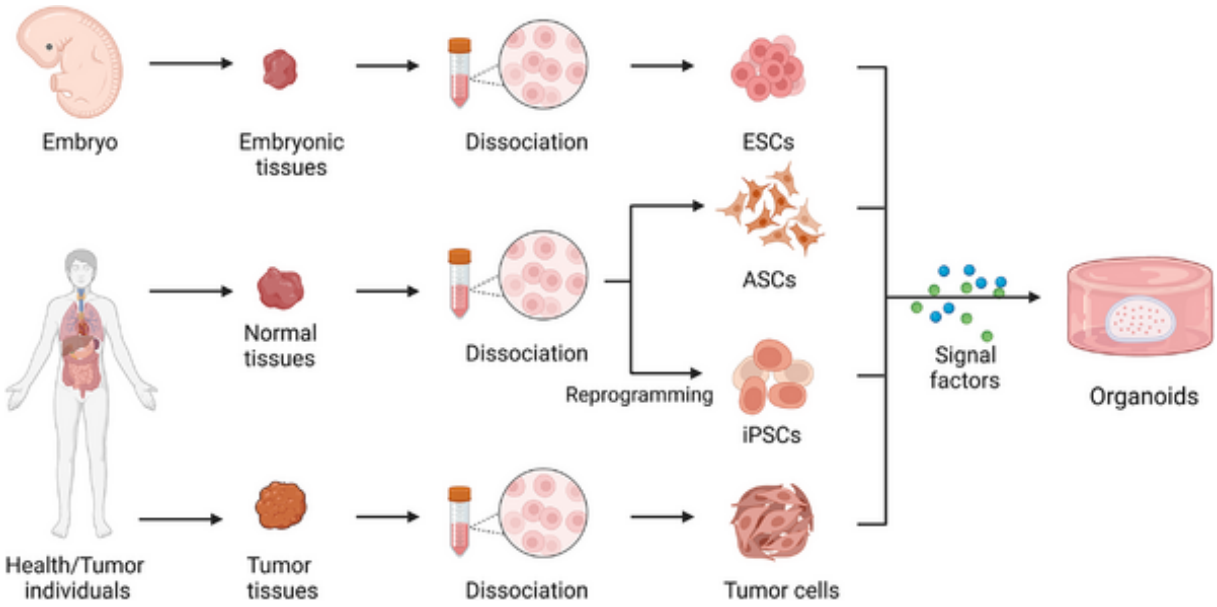


Figure 12: **Development of organoid models.**
Different process of organoids formation. Taken from [38].

They differ from other 3D *in vitro* models in use, due to their similar function to the organs they aim to mimic, providing great use in toxicology, drug screening or personalized disease evaluation [16].

Moreover, as seen in Figure 13, the biomedical applications can vary. Since organoids are able to conserve gene expression and genetical mutations of the parental cells, they also have a strong application in terms of replicating hereditary and genetic diseases. Furthermore, they are highly efficient and do well in large-scale screening [38].

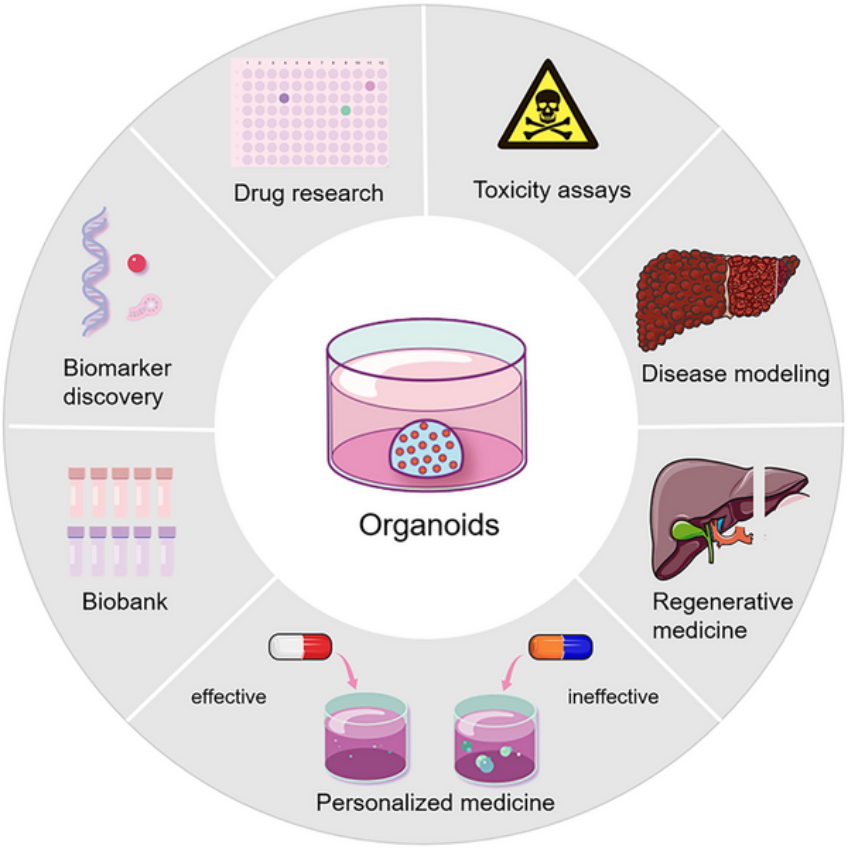


Figure 13: **Biomedical applications of organoid models.**
Different biomedical applications of organoids. Taken from [38].

However, they present some problems such as lack of communication with surrounding cells, for example, the lack of interaction with immune cells makes the organoid uncapable of mimicking an immune response [16].

In addition, the reproducibility between different laboratories is low, leading to varying results, which could be solved by "establishing procedures and quality control standards to increase the popularity of organoid technologies and the reproducibility of organoid generation." [38].

2.3.3 Scaffold- based 3D culture

In this case, cell culture is performed on the scaffolds, which mimics the ECM, with the goal of assessing the interactions between both. The structure can either be natural or synthetic. Hydrogels of natural (e.g. sodium alginate, gelatine or collagen) or synthetic (e.g. polyethylene glycol (PEG)) provenience are shown in Figure 14. However, these models are limited to certain cell types, culture conditions, and designs, making them harder to customize [16, 32].

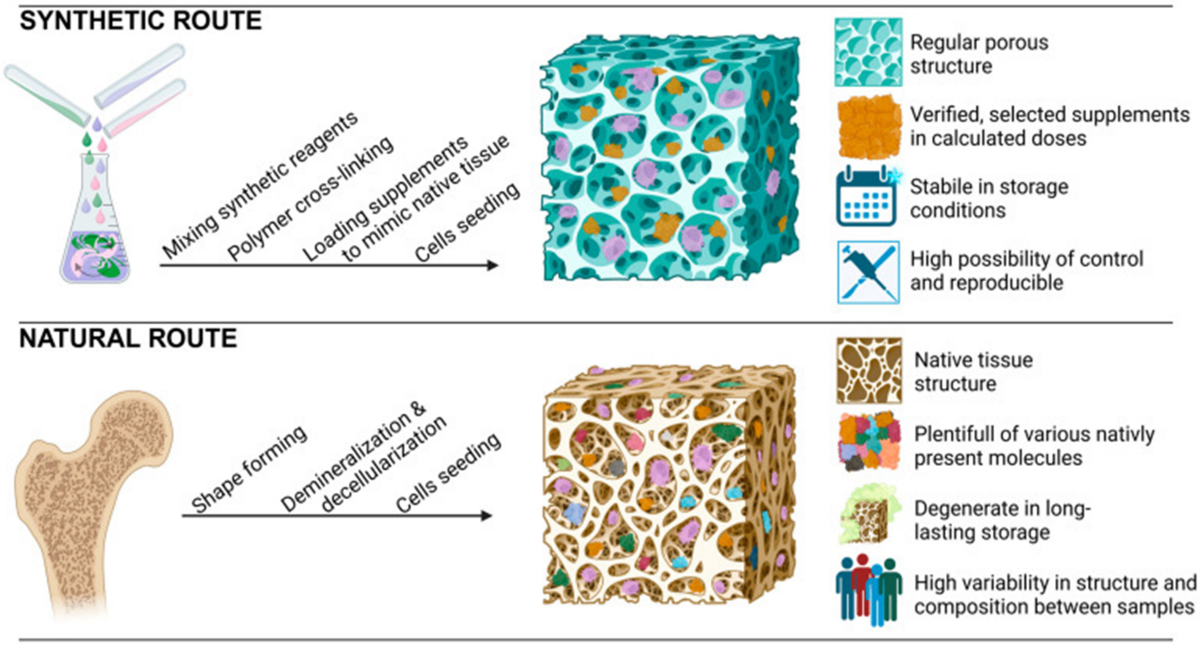


Figure 14: **Synthetic and natural scaffold-based 3D models**
Development of synthetic and natural scaffold-based 3D models and their applications. Taken from [39].

Cells, when encapsulated in the scaffold, make it possible for observation of their behaviour and then application in tissue engineering. While scaffolds play a crucial role in supporting cell seeding in damaged organs or vessels and tissue regeneration, their primary application in tissue engineering means that they are often optimized for structural support rather than for reproducing physiological conditions. Therefore, these models may exhibit limited physiological relevance [39, 40].

Scaffolds have gained a growing interest, specially in cancer research, due to the possibility of study the behaviour, drug response, cell interactions, matrix alterations, and relation to the environment. The variety of materials used to build the scaffold makes this model extremely versatile in terms of mimicking different mechanical and rheological properties of different human tissues (Figure 15) [40].

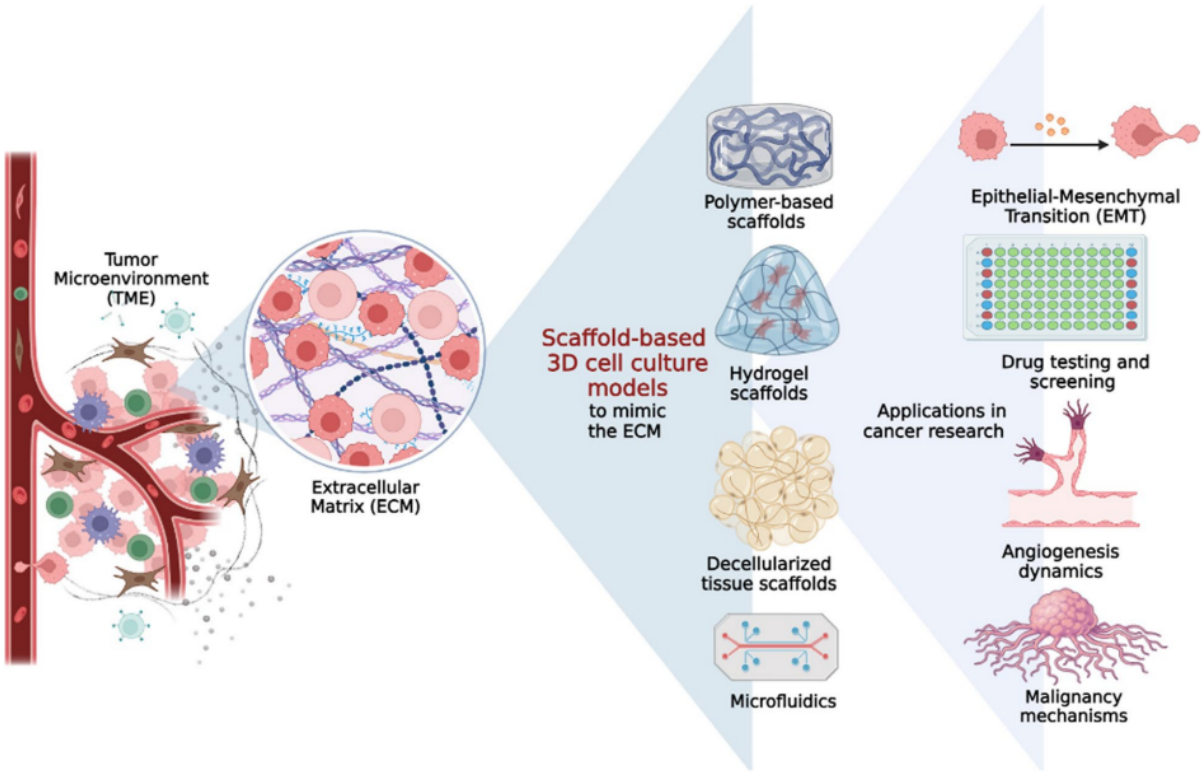


Figure 15: **Scaffolds structures for tumour models.**
Application of scaffold structures to replicate tumor microenvironments and its applications in cancer research. Taken from [40].

2.3.4 Spheroids models

Spheroids are characterized as cells self-assembling aggregates because of extracellular matrix and membrane proteins, as integrins, for example. Therefore, spheroids are recognized for their stable morphology and accurate replication of *in vivo* interactions, especially cell-cell interactions and ECM expression [41].

However, due to their growing compact structure, the oxygen and nutrients distributions must be guaranteed to assure the cells in the center of the spheroid do not lose viability, leading to the formation of a necrotic core. To prevent this from occurring, even though there are larger successful spheroids, it is recommended not to exceed the 200 μm of diameter. Moreover, currently the techniques available for characterization have been designed for 2D models, making the characterization process more complex [41, 42].

Table 3: **Advantages and limitations of different 3D *in vitro* models.**

Advantages and limitations of different 3D *in vitro* models (organ-on-a-chip, organoids, scaffold-based 3D culture and spheroids models).

	Advantages	**Limitations**
Organ-on-a-chip [37]	Good perfusion and fluidic control	Complex development
	Good control and precision	Costly electrical components
Organoids [16, 38]	Similar replica of organs	Lack of communication with immune cells
	Efficient in large-scale screenings	Low reproducibility between laboratories
Scaffold-based [39, 40]	Good cell observation and application in tissue engineering	Limited physiological responses
	Good replica of different human tissues	Less customizable in terms of cell types, culture conditions and designs
Spheroids [41]	Stable morphology	Size limitations to guarantee oxygen and nutrient distribution
	Accurate replica of *in vivo* interactions	Difficult characterization

Spheroids formation

- **Hanging Drop**

The hanging drop method is one of the most used techniques since it only requires the application of a drop of cells inside a culture plate, inversion of said plate and through gravity the cells concentrate at the bottom of the drop, leading to the formation of the spheroids, as seen in Figure 16 [42].



Figure 16: **Hanging drop technique.**
Representation of the hanging drop technique for spheroid formation. Figure created with BioRender, 2025.

This method is then recognized for its simple use and low cost. Nevertheless, this is not applicable to all cell types, presents low throughput and involves small volumes of cells presenting some of the

disadvantages of its use [42, 43].

- **Rotary cell culture**

This technique is based on the spheroids production by mechanical stimuli inside a bioreactor. In these cases, and according to Figure 17, the cell collision due to the connective forces leads to aggregation between cells, leading to the spheroids aggregation [41].

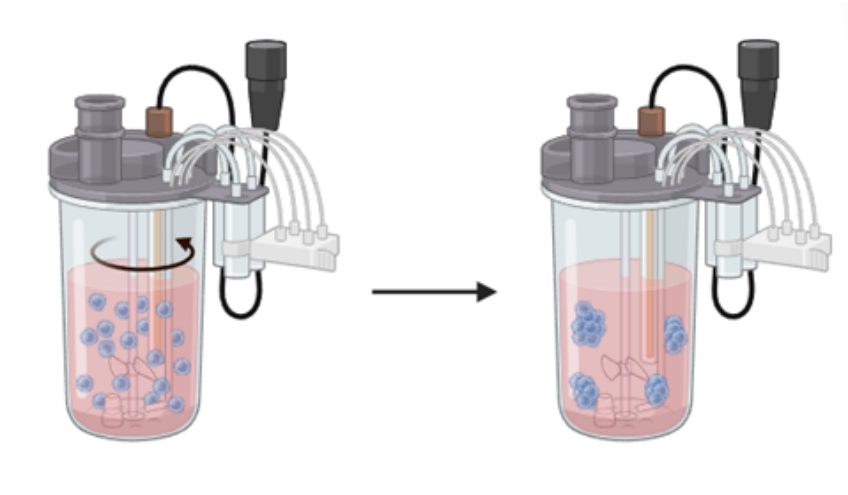


Figure 17: **Rotary cell culture technique.**
Representation of the rotary cell culture technique for spheroid formation. Figure created with BioRender, 2025.

Bioreactors are mostly used when a larger scale of spheroids is needed, since it creates greater variations in spheroids sizes and damage to the cells due to the mechanical force. Moreover, special equipment is required, and obliges production of spheroids with same characteristics which is not advantageous for this project [42, 44].

- **Magnetic levitation method**

Regarding the magnetic method, the cells are first treated with paramagnetic iron oxide nanoparticles to make them responsive to the magnetic force. After applying the magnet, the cells are pulled up, since the magnetic field is stronger than the gravitational force, allowing for the spheroids formation, as seen in Figure 18 [42, 45].

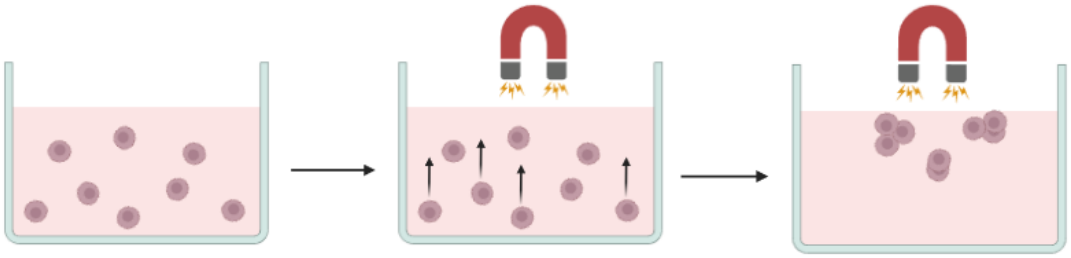


Figure 18: **Magnetic levitation technique.**
Representation of the magnetic levitation technique for spheroid formation. Figure created with BioRender, 2025.

In addition, this method has shown some similar features to *in vivo* models, and reduced the development of a necrotic core which suggests good potential. However, the magnetic force can lead to changes on cellular morphology resulting in apoptosis or necrotic core formation, which is more desirable in oncology studies [45, 46].

- **Microfluidic system**

Microfluidics or lab-on-a-chip techniques try to replicate *in vivo* structures in microscale dimensions. In these systems, the microwells are connected by microfluidic channels allowing a microfluidic flow of cells, oxygen or nutrients (Figure 19). In this way, the mixing and culturing of cells is integrated allowing different spheroids sizes, selected beforehand and depending on the channel size, with just one cell density and preventing hypoxia [42, 47].

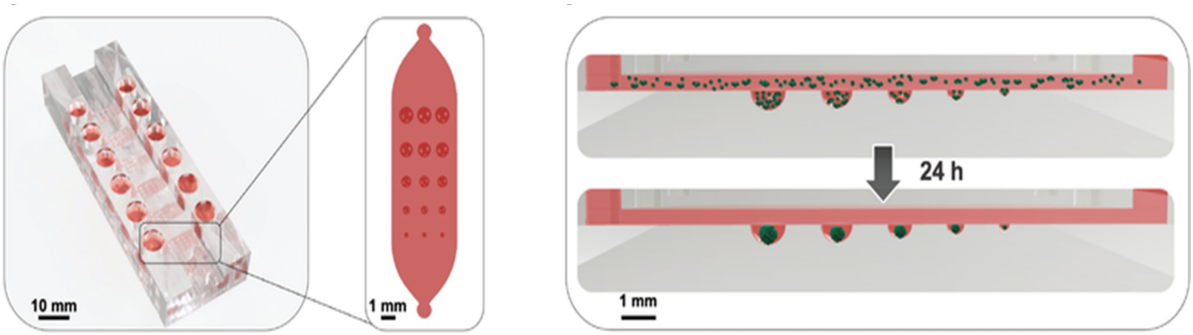


Figure 19: **Microfluidic system for spheroid development.**
Representation of the microfluidic array for spheroid formation. Taken from [47].

Despite the various advantages, these systems are expensive, the results can be affected by the device material (normally PDMS), the design used and they are not high throughput [48].

- **Non-adhesive hydrogels**

Lastly, in this kind of cell culture, the cells are seeded in devices with texture (wells, indentures, microwells or recesses) where they can sink and self-assemble in other to create the 3D spheroids structures. Due to the non-adhesive nature of the hydrogel adhesion between cells is promoted, leading to more cell-cell interactions [42].

This technique is widely recognised due to its simplicity of usage and monitorization, lower cost and control of the geometry of the spheroids allowing high reproducibility and uniformity [41].

Taking these advantages into consideration, non-adhesive hydrogels devices were chosen for this project with the aim of obtaining uniform spheroids with a diameter smaller than 200 µm through a simple process of production, control and analysis of the results. In this way, the ideal structure is a "mold with multiple arrays of micropillars that will later be used to cast microwells of well-defined dimensions and shapes in biocompatible non-adhesive hydrogel" [41]. As seen in Figure 20, this mold is first designed using CAD software to precisely set the dimensions of the micropillars and then 3D printed, allowing reusable molds, which emphasizes the sustainability of this process [41].

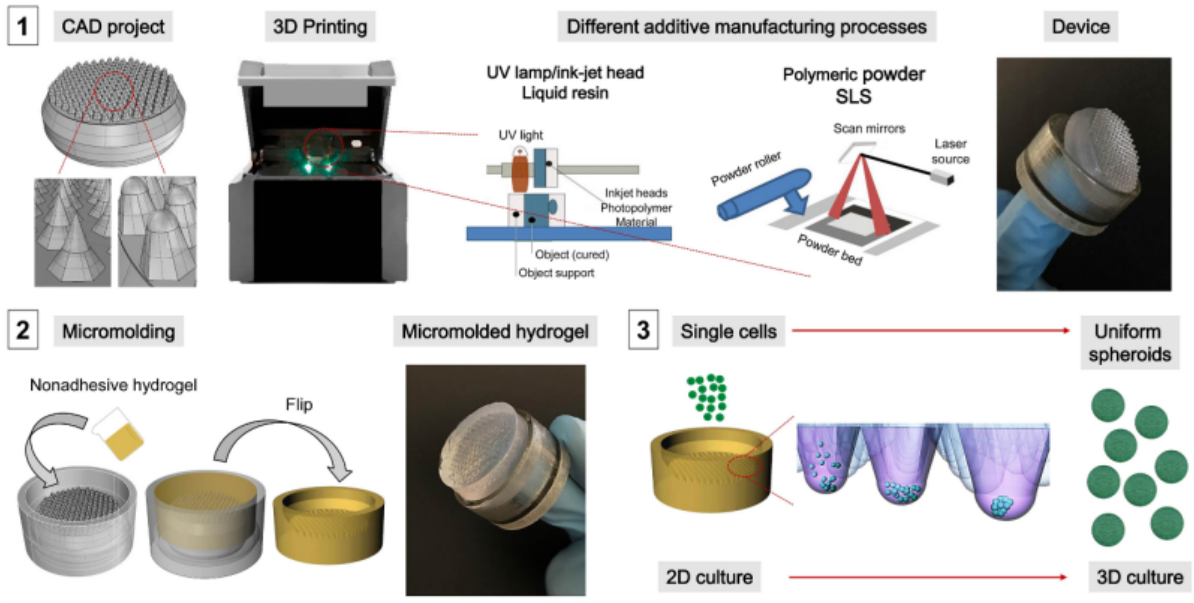


Figure 20: **Development of a non-adhesive hydrogel structure.**
Three step process of develpoing non-adhesive hydrogel structures, from printing, micromolding and spheroid formation. Taken from [41].

When utilizing the mold, the hydrogel used must be non-adherent, not toxic, biocompatible, sterile and, preferably, transparent, so it is possible to monitor. Accordingly, agarose or polyacrylamide are usually chosen for the devices, in this case agarose [41, 49]. As a disadvantage, this process can be time

consuming since a long-term culture is required, at least 1 week to reach the spheroid conformation [48].

Overview of existing spheroids

Due to their growing potential, spheroid production has been done with different techniques and aims.

For example, 3D spheroids of 4 cell types, with THP-1 cells, HepG2 cells, PUMC-HUVEC-T1 cells and human hepatic stellate cells, have been developed for a liver spheroid model to predict hepatotoxicity. These spheroids were grown in a 96-well ultra-low attachment surface spheroid microplates, did not present a necrotic core and could accurately replicate critical features of drug-induced liver lipid dysregulation, cholestasis, and fibrosis, thus indicating the corresponding risks [50].

Another case is the development of spheroids for testing anti-tuberculosis drug response in cases of an HIV infection with the use of THP-1 cells infected with mCherry-expressing Bacillus Camille Guérin (BCG), to model a tuberculosis infection. In this experiment they used a 96-well ultra-low attachment plate and were able to produce the spheroids capable of monitoring in real time the immune system reaction, including the formation of the granuloma [51].

In line with the previous example, another tuberculosis spheroid model was developed with THP-1 cells infected with mycobacteria, not for HIV cases but to better understand disease pathogenesis and drug response. In this case, a non-adherent hydrogel was also used, but in a format of *Aggrewell™ 400 wells*, and the formation of a necrotic core was observed, which was considered a positive sign that replicates the immune system response to the infection, allowing a deep dive into the reasoning behind this occurrence [52].

Moving to a cancer model, a 3D co-culture model to study pancreatic ductal adenocarcinoma through activated pancreatic stellate cells (aPSCs), THP-1 cells in type I collagen and pancreatic tumour spheroids in a microfluidic channel chip was developed. This led to a model capable of analysing anti-cancer agents in cancer and stromal cells [53].

With the aim of better understanding fibrosis and the FBR, a 3D model using fibroblasts and monocytes, later differentiated into macrophages, was created. The results showed high cell viability and abundant collagen deposition for an *in vitro* fibrosis model, leading to a model capable of efficiently testing drugs and testing designs for better medical devices [54].

Taken together, these studies highlight the potential of the development of spheroids as 3D *in vitro* models for a better understanding of the immune response and the FBR. Nevertheless, beyond their use as models, bioprinting may further enhance their handling, reproducibility and applicability [41].

2.4 3D Bioprinting

3D bioprinting, known as the process of printing living cells in a predefined pattern using an appropriate ink, is a technique that first appeared in 2004 with a system of ejectors capable of printing biological materials. From that point onwards different milestones have been conquered, from bioprinted heterogeneous aortic valve using alginate-gelatine hydrogels, to 3D-printed HeLa cells to generate an *in vitro* cervical tumour model or bioabsorbable airway splint created to treat tracheobronchomalacia [55].

This technique can be used to study infectious diseases and tumours, to tackle tissue regeneration or for pharmacokinetic studies [56]. In all these cases the goal is to obtain a model capable of simulating the disease/body reaction or a model for high-throughput drug testing. Accordingly, in this way it is possible to solve some of the problems other models have, regarding low vascularization, nutrients and oxygen supplementation and control over chemical flow and mechanical forces. Besides these promising characteristics, 3D bioprinting also presents some problems, in terms of associated costs, biocompatible bioinks, uniformity of cell distribution within the printed structure and difficulty of standardization. These disadvantages vary depending on the method chosen for the bioprinting [34, 36, 55–57].

2.4.1 Bioprinting methods

- **Inkjet-based bioprinting**

In inkjet-based technique, droplets of bioink are rapidly ejected from a nozzle into a substrate to create a defined structure. This happens through either a piezoelectric actuator or an electric heater that creates a pressure pulse allowing the droplets to be ejected (Figure 21) [58].

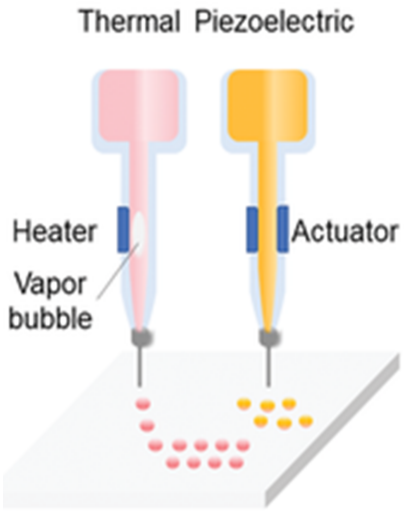


Figure 21: **Inkjet-base bioprinting.**
Representation of inkjet-base bioprinting method. Taken from [59].

This method offers a high speed and high-resolution model with precise control over the droplets making it a better solution in cases of low cell number. On the other hand, the choosing process of the bioink must also be taken into consideration since the surface tension and too high viscosity of the bioink might led to clogging of the nozzle and compromise the final structure [34, 58].

- **Laser-based bioprinting**

The laser-based system uses a laser pulse to transfer the bioink. In this way, the upper slide (donor layer) of the system is in contact with the bottom one (energy adsorbing layer) that responds to laser stimulation, followed by the bioink layer, as represented in Figure 22. Because of the laser, a vapor droplet is created on the upper layer that pushes a bioink droplet downwards. This process is repeated the number of times needed to obtain the desired structure [59].

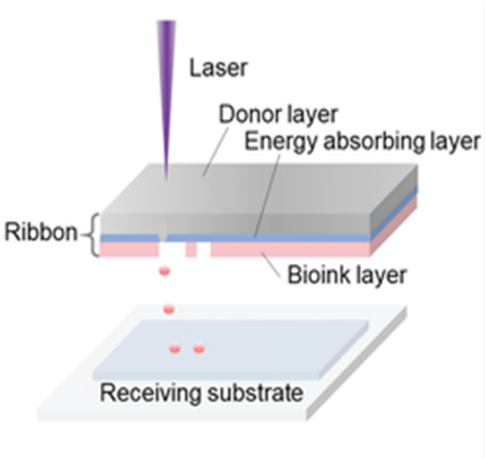


Figure 22: **Laser-base bioprinting.**
Representation of laser-base bioprinting method. Adapted from [59].

By saving the cells from passing through the nozzle, this mechanism results in high cellular viability and is less restrictive in terms of the bioink choosing process, since it works with different viscosities. However, the technique can be complex, time consuming, expensive and the laser might damage the cells [34, 58, 60].

- **Kenzan method**

This method differs from the others since its only used for bioprinting of spheroids. In this case, the spheroids are placed in a needle array for temporary support, to allow tissue formation and maturation. When the desired structure is reached it is removed from the bioprinter and ready to use (Figure 23) [61].

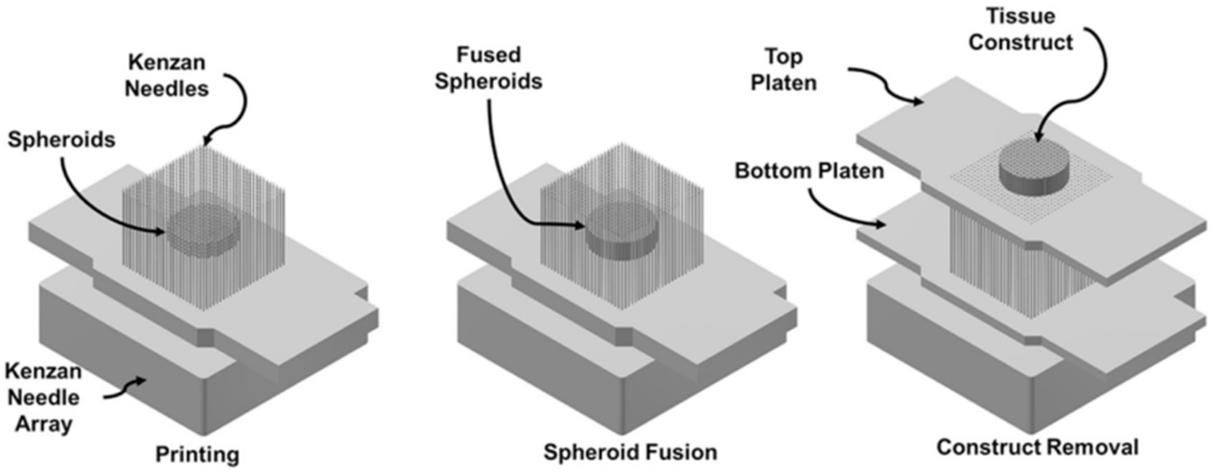


Figure 23: **Kenzan bioprinting.**
Representation of the Kenzan bioprinting method. Taken from [62].

Accordingly, this strategy enables precise control over spheroid positioning and provides adequate mechanical properties for handling within a scaffold-free system, which may be beneficial for clinical transplantation. Nevertheless, important challenges remain, particularly regarding geometric constraints, procedural complexity, and construct removal from the needle array. Furthermore, spheroids must exhibit high size uniformity to function properly [61, 63].

- **Biogripper method**

The biogripper method is based on three steps: pick up, place and perfuse. Therefore, the machine first picks the cells or spheroids, places them on top of the previous ones and allows the communication between cells, as shown in Figure 24 [64].

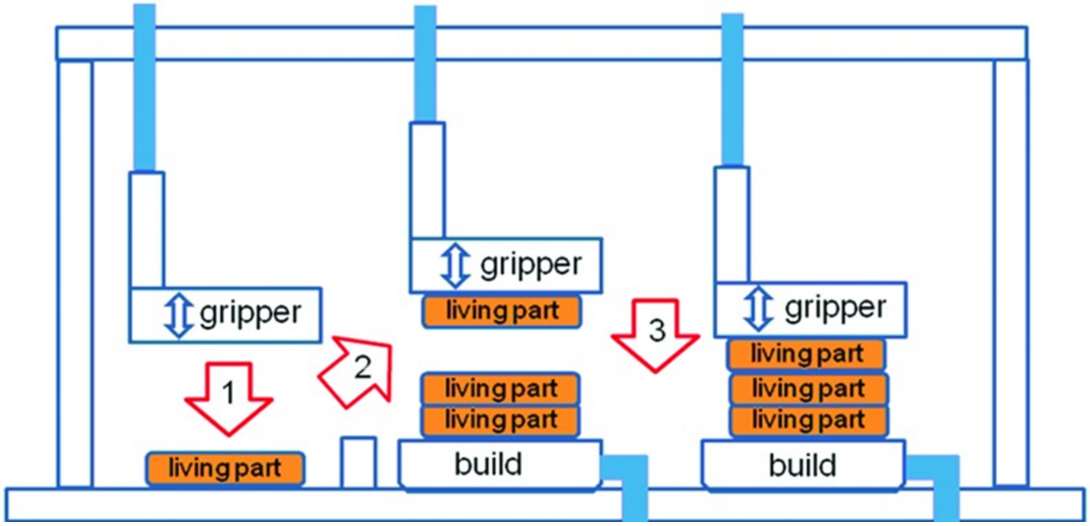


Figure 24: **Biogripper bioprinting method.**
Representation of the biogripper bioprinting method. Taken from [65].

In this way the perfusion of the cell media is facilitated, and precise application of the spheroids is possible leading to the strong ability of scaling up. However, the performance is limited to bigger spheroids and automation would be necessary for it to be considered in the tissue engineering field [61, 63].

- **Extrusion-based bioprinting**

This method consists of the extrusion of a bioink (cells and biomaterial combined) through a nozzle or needle, by pneumatic or mechanical pressure, as seen in Figure 25. Afterwards, it might need a crosslinking step by UV light or ionic solution to guarantee the stability of the structure produced. An important requirement is choosing the right biomaterial, since they need to have a degree of viscosity, to

maintain the structural integrity, but also need to be able to be extruded (with shear-thinning behaviour) and be biocompatible [34].

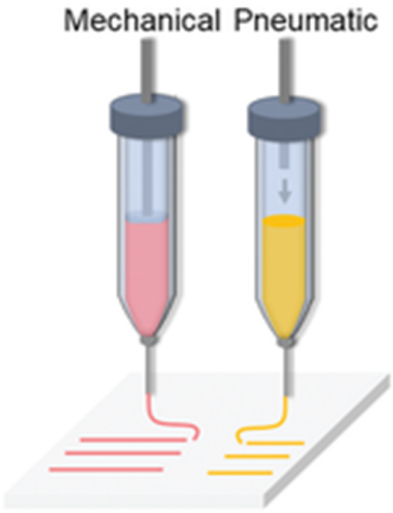


Figure 25: **Extrusion-based bioprinting.**
Representation of the extrusion-based technique, using pneumatic or mechanical pressure. Taken from [59].

Overall, this technique was chosen for this project because of its versatility, low cost, scale-up possibility and simple application. However, it must be taken into consideration that during extrusion a lot of pressure is exerted which might impact the cells or spheroids [34].

In addition, the bioprinting was done in a grid like structure since it supports bigger aggregates, allowing better oxygen and nutrients transfusion and higher cell growth [66].

2.4.2 Bioink

As previously stated, choosing the appropriate biomaterial to form the bioink can be a challenging step. It must take into consideration the biophysical and biochemical properties of both the biomaterial and the cells, in this case the cellular spheroids. More than just biocompatibility and viscosity, shear-thinning, yield stress, printability and recoverability must also be evaluated [67].

Characteristics

- **Viscosity**

Viscosity describes the resistance to motion between the internal layers of a material, meaning that materials have different forces of interaction (dipole-dipole and hydrogen bonds) that divide them into high-viscous and low-viscous materials. For extrusion-based bioprinting the viscosity of the bioinks is usually

from 30 mPa·s to 6×10^7 mPa·s. This indicates that the viscosity of the material chosen must respect this printability window. Conversely, materials with higher viscosity might incapacitate the bioink flow, leading to the deposition of droplets instead of a continuous filament. The opposite can also happen when materials with low viscosity flow too quickly which results in loss of conformation after extrusion due to quick spreading which reduces the precision of the method. In this way, filaments are preferred, since they form a high-fidelity 3D structure instead of an amorphous structure [67].

- **Shear-thinning ability**

To complement the viscosity analysis, shear thinning needs to be taken into consideration. This parameter evaluates the behaviour of non-Newtonian fluids, materials whose viscosity decreases as the shear rate increases [68]. The power-law model (2.1),

$$\eta = K\gamma^{n-1} \tag{2.1}$$

η = viscosity

K= consistency index

γ = shear rate

n = flow behaviour index

is used to describe the relation between the viscosity of the material and the shear rate applied, allowing classification into Newtonian (n = 1), shear thinning (n < 1) or shear-thickening (n > 1). If the fluid is shear thinning its viscosity lowers when the shear rate increases. If the fluid is shear thickening, then the viscosity increases with the increase of the shear rate [69].

This evaluation is important to predict if the material is appropriate for bioprinting. When it comes to extrusion-based bioprinting, ideally, the material should become less viscous when passing the nozzle to facilitate the printing process. This happens in materials with shear thinning behaviour due to the shear stress that the bioink is subjected to (i.e. physical crosslinks are broken and chains are aligned), making it less viscous and able to pass the nozzle. In addition, after passing the nozzle, the shear rate decreases, increasing the viscosity, which helps the printed structure to maintain its shape and prevents spreading or collapsing. Therefore, it must have a shear-thinning behaviour, n < 1, making these types of fluids better for extrusion-based bioprinting [67, 69].

- **Yield stress**

This factor evaluates the minimum force required so a material can maintain a continuous flow. Therefore, materials with low yield stress (2-10 Pa) pass the nozzle with almost no force application,

preventing cell damage. However, the construct does not hold as well and there is a separation of the cells and the hydrogel. On the other hand, materials with high yield stress (50-300+ Pa) require a higher application of force to be printed which can affect cell viability but are able to maintain their shape after printing. Consequently, the biomaterial chosen, ideally, should have a low to medium yield stress or be adapted to do so [67, 70–72].

- **Shear recoverability**

The recoverability is evaluated by the viscosity changes after printing. The bioink after passing the nozzle, where it was subjected to stress, must be able to regain its initial properties. When the bioink does not have a good recovery, lower than 80%, it can have a low resolution and accuracy, which means the chosen bioink should have high recoverability. In this way, comfort to encapsulated cells and maintenance of the geometric fidelity can be provided [73, 74].

- **Crosslinking**

Crosslinking is a crucial step in the bioprinting process, responsible for making 3D structures more stable, especially at 37°C and in media, the conditions required by the cells to survive. This step can affect the mechanical and physicochemical characteristics of the bioprinted constructs and the cellular behaviour. As seen in Figure 26, it can be done by photocrosslinking, click chemistry, self-assembly and ionic crosslinking, for example [67, 75].

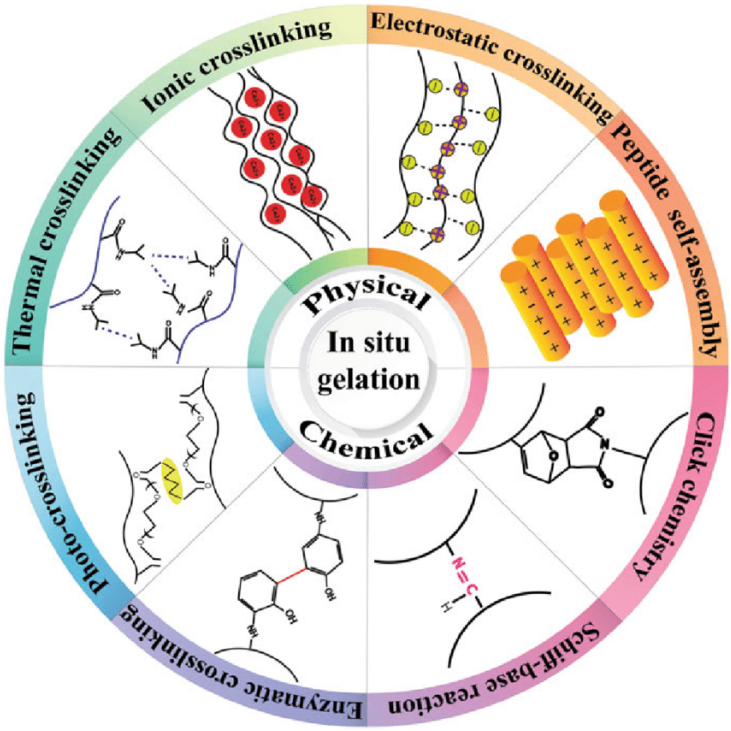


Figure 26: **Different types of crosslinking hydrogels.**
Examples of physical and chemical types of crosslinking. Taken from [75].

This choice depends on the end-groups of the polymers. So, polymers with acrylate end groups undergo photocrosslinking, thiol groups use a thiol-ene chemical crosslinking, cases with added cations suffer ionic crosslinking and, lastly, self-assembling peptides whose crosslinking happens spontaneously by themselves [67, 76].

- **Printability**

After printing the final structure, the printability can be tested. The printability corresponds to the quality of the extrudate, in other words, is the comparison of the extruded experimental dimensions and the theorical ones, leading to a relative evaluation of the pore geometry [69]. This parameter can be calculated through Equation 2.2:

$$Pr = \frac{P^2}{16A} \tag{2.2}$$

Pr = Printability Index

P = Perimeter

A = Area

If the Pr value = 1, the printed structure exactly matches the model design. If Pr < 1 indicates an enlarged

and curve structure, while if Pr > 1 the construct has an irregular or rough shape, as pictured in Figure 27 [67, 72].

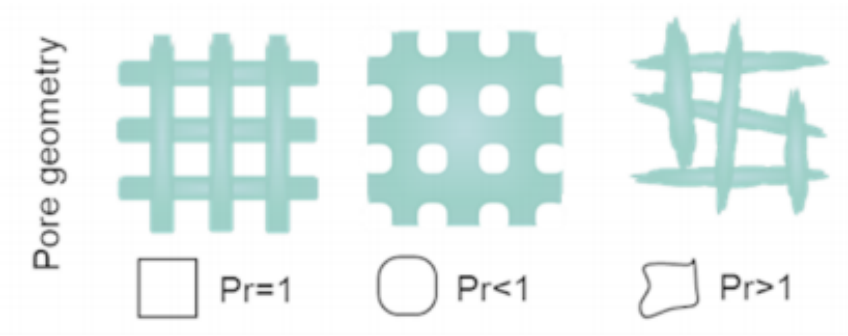


Figure 27: **Printability index and pore geometry.**
Examples of different constructs depending on the printability index. Taken from [69].

- **Biocompatibility**

Biocompatibility is the ability of one material to be in direct contact with a biological component without adversely or significantly affecting it [77].

Accordingly, both the interactions between cells, the material, and the degradation by-products require evaluation. This evaluation is done with cytotoxicity and viability assays. Moreover, it is important to assess if the crosslinking required by the material affects the cell viability [67].

Types of bioink

In terms of origin of the bioink, it can be categorised as synthetic, natural or hybrid.

The major advantage of synthetic bioinks is their capacity to be precisely modified to meet the specific requirements of different cell types or tissues. Nonetheless, they are limited by the difficulty of cell encapsulation due to lack of sites for cellular recognition. In this way, cell proliferation and differentiation can be compromised, which leads to the need of functionalization in order to improve their biological properties. PEG, polyvinylpyrrolidone (PVP), poly(l-lactic) acid (PLA) and poly(lactic-co-glycolic) acid (PLGA) are just some examples of synthetic polymers currently being used in 3D bioprinting [78].

Natural bioinks are known for their optimal environment for cell growth since they present good biocompatibility and biodegradation properties. However, they lack mechanical properties making it difficult to bioprint and offering less support for the cells in the structure. Some examples are agarose, alginate, collagen, decellularized extracellular matrix, fibrin, among others [79].

Because of the disadvantages exposed, hybrid bioinks have become a growing solution. These materials integrate two or more components of inorganic/synthetic or organic/natural origin, assuring that the ideal

structural support is guaranteed while maintaining biological functionalities. As examples there is blended GelMA and hyaluronic acid (HA), collagen – agarose, polycaprolactone (PCL) – fibrin and collagen, PCL – alginate, among others [80].

Taking into consideration the parameters and characteristics presented above, this section will be focused on the most used biomaterials for bioprinting and their properties.

- **Poly(ethylene glycol) (PEG)**

This synthetic polymer, produced through the polymerisation of ethylene oxide, is well recognised for its adaptable mechanical properties, its ability to be chemically tailored, and its non-cytotoxicity. However, as it is a bioinert material it has a low cell attachment. To surpass this limitation, some modifications to the PEG structure can be made with gelatine, fibrinogen, collagen, among others making it a very attractive option for bioprinting [80].

- **Decellularized extracellular matrix-based materials**

As the name suggests, this material is the isolated extracellular matrix of a tissue from inhabiting native cells. As expected, is very tissue specific choice and has a high biological relevance for printing. Despite this, it is not very stable, lacks consistency and a defined composition [80].

- **Alginate**

This natural material is a biopolymer from brown algae, very similar to the glycosaminoglycans found in the native ECM of the human body, with the advantage of being highly biocompatible, having mild crosslinking conditions and a low cost. On the other hand, it has a slow degradation rate and poor cell adhesion, since it is a biologically inert material [80].

- **Collagen**

This biological compound is the main structural protein of the ECM of mammalian cells, which leads to a high biological relevance for usage. Even though is possible to use pure collage for bioprinting, it requires high concentrations of collagen and low temperatures, making it harder to use. However, since collagen can be crosslinked, the strength, stability and mechanical properties increase. On the other hand, crosslinking can affect cell viability because of the new components, and their possible cytotoxicity. In this way, a careful analysis and balance of the advantages and disadvantages must be made [80, 81].

- **Gelatine**

This protein is derived from partial hydrolysis of collagen and is widely used for its biocompatibility, water solubility, and thermally dependent gelation. As it is thermosensitive, at lower temperatures forms a hydrogel and at high temperatures has a more viscous or liquid behaviour. Moreover, it has strong cell affinity, making it a good option for bioprinting. However, there is still a need to improve the cells encapsulation, differentiation, and migration within this material. In addition, prolonged gelation time due to its temperature sensibility is also one of the most common problems [80, 82, 83].

- **Gelatine modifications**

Consequently, since gelatine has accessible active groups, it can be easily modified to improve printability. In this way, a modified gelatine with photopolymerizable methacryloyl groups (GelMA) is commonly used. This change allows photocrosslinking with UV light enabling the maintenance of the structure [83]. GelMA or gelatin methacryloyl, is the result of the reaction of gelatin and methacrylic anhydride (MAA). In this way, the amino groups of the gelatin are replaced by methacryloyl groups, from the MAA, as explained in Figure 28 [83].

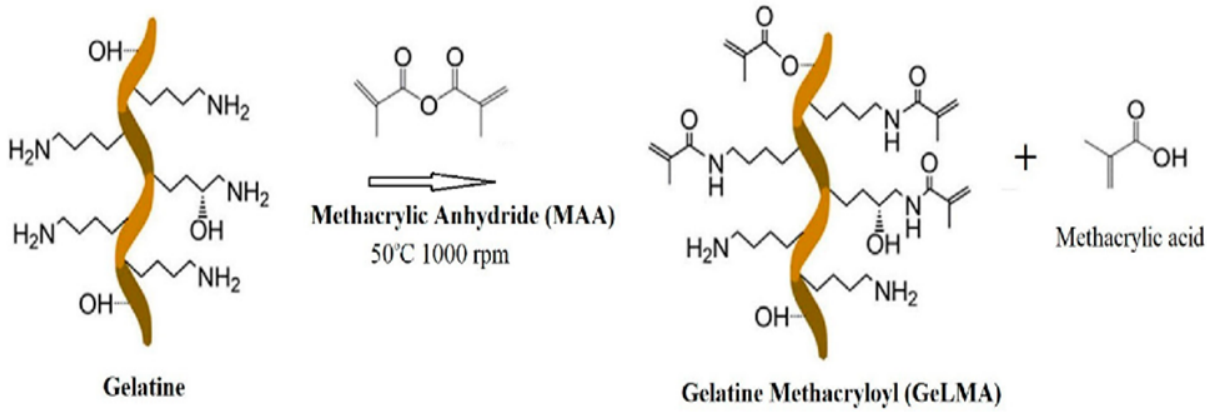


Figure 28: **Chemical composition of GelMA.**
Chemical transformation of gelatine into GelMA. Taken from [84].

This modified gelatine is still highly influenced by temperature and biocompatible because of the gelatine properties, is susceptible to photocrossilinking due to the added groups and is flexible to other changes to meet specific requirements [85].

The production process of GelMA can vary depending on the final application. In this project the GelMA used was derived from porcine gelatin with enhanced printability and crosslinking through the incorporation of methacrylate groups with 0.25% lithium phenyl-2,4,6-trimethylbenzoylphosphinate (LAP) as a photoinitiator. In terms of the parameters to take into consideration, the optimal temperature is

considered between 25 – 32 °C and the recommended photocrosslinking irradiation is either 365 nm or 405 nm. Furthermore, most studies showed good printability index with GelMA structures, emphasizing its promising application for bioprinting [86–89].

2.4.3 Overview of 3D bioprinted models

As explained, bioprinting is a not a new technique, however, the work previously done varies from cell types, to methods and different applications, emphasizing the diversity of this technique.

In one of the models, a 3D printed structure of THP-1 single cells was made with the purpose of modelling the inflammatory response and evaluating the efficacy of ibuprofen as an anti-inflammatory agent. In this case, an analysis of the macrophage differentiation and polarization was made, inside the bioprinted structures. However, the authors revealed that further investigations regarding a more accurate model of human tissue, would be important to investigate. The incorporation of different types of cells and the relation between them, would be a step towards a more comprehensive replica of a target tissues [90].

In terms of printing spheroids, they present a bigger problem to print when compared to single cells. Since the spheroids are self-assemble agglomerates of cells, they can reach a much bigger diameter which could be a disadvantage during the printing process. Thus, the importance of also evaluating the current SoA about bioprinted spheroids has a pivotal role.

One example is the bioprinting of human mesenchymal stromal cell (hMSC) spheroids in a xanthan gum (XG)-alginate hydrogel. The goal of this project was to differentiate the stem cells spheroids into cartilage after bioprinting. In this way, alginate and XG, which are two natural polysaccharides, were combined with the spheroids and, after printing, ionically crosslinked. In this manner, a viable bioprinted structure was obtained and had good evidence of chondrogenic differentiation of hMSC spheroids, leading to a possible 3D model for different cartilage diseases [91].

In a similar case, human bone marrow-derived mesenchymal stem cells (hBM-MSC) were used to form spheroids and printed in a different hydrogel, GelMA, with an extrusion-based technique. In this case, the spheroids were still viable and were able to differentiate into cartilage microtissue, even after bioprinting. These results accentuated the possibility of developing a model with GelMA capable of encapsulating viable spheroids [92].

Overall, considering the major role of macrophages and fibroblasts in the inflammatory and immune response, the FBR and, consequently, in fibrosis, the development of mixed spheroids, from THP-1 and HDF, is a more biologically relevant approach to model these cellular interactions within a 3D environment.

To give structure to the spheroids, a bioprinting process through an extrusion-based technique al-

lows a controlled deposition of the spheroids. In this regard, GelMA stands out as a biocompatible, photocrosslinkable, and rheologically suitable hydrogel for bioprinting

All in all, the present project aims to develop and characterize a bioprinted model that includes THP-1 spheroids and co-cultured THP-1 and HDF spheroids, embedded in GelMA, to establish a 3D *in vitro* model able to mimic the human inflammatory response.

Chapter 3
Methods

3.1 THP-1 cell culture

THP-1 human monocytic cells were culture in roswell park memorial institute (RPMI) 1640 Medium (RPMI 1640; Gibco, Thermo Fisher Scientific, Waltham, Massachusetts, USA) supplemented with 10% fetal bovine serum (FBS), 1% penicillin streptomycin (Pen/Strep) (Pen/Strep; Gibco, USA) and 1% glutamine (GlutaMAX; Gibco, Thermo Fisher Scientific, Waltham, Massachusetts, USA) and incubated in 5% CO_2 at 37°C.

The cells were passaged when the stationary stage of growth was achieved. The cell suspensions of the T75 culture flasks were pipetted out and centrifuged at 1000 rpm for 1 minute. The pellet was resuspended in RPMI 1640 medium, in a dilution of 1:3, and added to a new culture flask (Figure 29A). To count the number of cells, the pellet was diluted 1:20 and trypan blue was also added in 1:2 ratio. 10 µL was then loaded into each chamber of a Bürker-Türk counting chamber, two quadrants were counted, and the final number of cells was obtained through Eq. 3.1:

$$N = \frac{(N_t + N_b)}{2} \times 2 \times dilution factor \times 10^4 \tag{3.1}$$

N = Number of cells

N_t = Number of cells in the top quadrant

N_b = Number of cells in the bottom quadrant

3.2 HDF cell culture

The HDF were culture in high-glucose dulbecco's modified eagle medium (DMEM-HG) (DMEM-HG; 4.5 g/L glucose, sodium pyruvate, and GlutaMAX; Gibco, USA) supplemented with 10% FBS and 1% Pen/Strep. They were incubated in 5% CO_2 at 37°C in T75 flasks.

At 70%-90% of confluency the cells were passaged. Firstly, the media was removed, and the cells were washed in 3 ml of phosphate-buffered saline (PBS) for 5 minutes, afterwards, 3 ml of prewarmed

trypsin (Trypsin-EDTA (0.05%), Gibco, Thermo Fisher Scientific, Waltham, Massachusetts, USA) was added and the cells were incubated for 3 minutes at 37°C and 5% CO_2. Then, they were observed under the microscope (Leica DM IL LED Fluo, Leica, Wetzlar, Germany) and if necessary, the flask was gently tapped to ensure proper detachment. Subsequently, the trypsin was quickly deactivated by adding 6 ml of fresh medium. After centrifuging at 1000 rpm for 5 minutes, the cells were resuspended in 1 ml of DMEM-HG medium and counted following the same procedure reported previously for THP-1.

3.3 Spheroids formation

The mold used for the spheroid's growth and the methods applied were previously described by Decarli et al. [91]. The molds were first washed with 70% ethanol for 5 min, after removing the ethanol they were washed two times with autoclaved demi-water. After removing the demi-water, the two parts of the molds were put together with sterile tweezers. Afterwards, 3% agarose (Sterile agarose, High EEO, Sigma-Aldrich, St. Louis, MO, USA) was added to a previously autoclaved flask with 0,9% NaCl saline solution (NaCl; 106404; Sigma-Aldrich, St. Louis, MO, USA), under sterile conditions. Accordingly, the devices were obtained by adding around 5 ml of the pre-warmed agarose solution to each mold. After 10 minutes, the devices were carefully removed from the molds with sterile tweezers, placed in a 6 well-plate with 2 ml of RPMI 1640 medium inside each of them to test for possible leakage. Afterwards, 2 ml of RPMI 1640 medium were placed outside of each device to guarantee proper hydration (Figure 29B).

After 24 hours, the medium inside the devices was removed and 1 ml of the THP-1 cell suspension was placed in each device. The seeding was done in 3 different concentrations (0.5 million cells/mL; 1 million cells/mL and 2.5 million cells/mL), following a drop-by-drop technique in a circular motion (Figure 29C). The cells were left still for 10 minutes to guaranty proper deposition inside the pins of the devices. Afterwards, 2nM of PMA was carefully added to the molds and they were left for 48h. As a negative control group, seeding of 1 million cells/mL and 2.5 million cells/mL without addition of PMA was also performed. After that, 1 ml of RPMI 1640 media was added in each device. The devices containing the cells were incubated in 5% CO_2 at 37°C (Figure 29D). The media inside the device was changed every other day using the same media employed to cultivate THP-1, apart from the first media change, made after 48h, which also included 2 nM of PMA.

The spheroids were observed, and pictures were taken every day for 7 days to measure the spheroids diameter using ImageJ software. The spheroids were removed at day 7, to evaluate their ability to remain compact outside the culture devices (Figure 29E). For this, the media was removed, and the devices were washed in a vertical motion for 3 times with 1 ml of fresh media for each time and lastly, they were left

upside down for 10 minutes to allow the spheroids to fully descend.

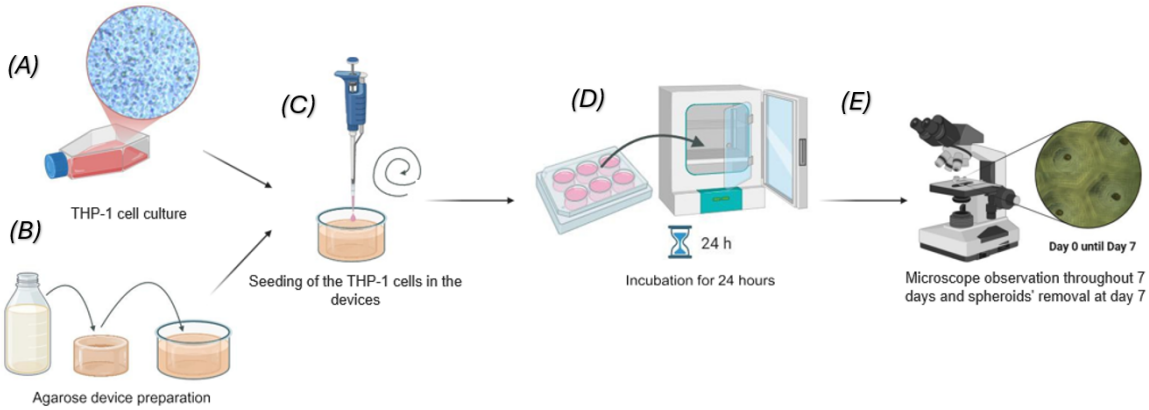


Figure 29: **THP-1 spheroids formation.**
(A) Culture of THP-1 cells; (B) Preparation of agarose devices; (C) Seeding of THP-1 cells into the devices using a circular motion; (D) Incubation at 37°C and 5% CO_2; (E) Microscope monitoring for 7 days followed by spheroid removal.

Mixed spheroids of HDF and THP-1 were also prepared with the aim of analysing the cellular behaviour and identifying the optimal ratio between the two different cell types to obtain spheroids suitable for 3D bioprinting, while maintaining a cell density of 0,5 million cells/mL. For this, both cell types were removed from their culture flasks (Figure 30A), resuspended in RPMI 1640 medium, and added in different ratios of fibroblasts and macrophages (8:1, 16:1 and 32:1), as shown in Figure 30B. Each group was seeded (Figure 30C), and 2 nM of PMA was added to each device for THP-1 differentiation. The media change was done every other day with RPMI 1640 media, apart from the first change that also included 2nM of PMA. Pictures of the spheroids were taken every day for a period of 7 days as before.

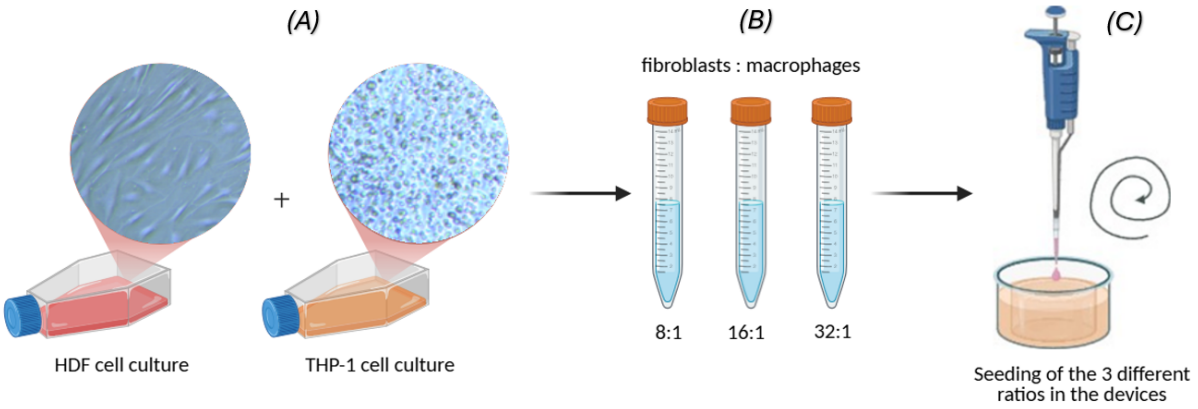


Figure 30: **Combined spheroids formation.**
(A) Culture of HDF and THP-1 cells; (B) Preparation of fibroblast-to-macrophage ratios (8:1, 16:1, and 32:1); (C) Seeding of the three ratios into the devices.

The spheroids morphological parameters (solidity, circularity and compactness) were evaluated according to Decarli et al. [41], through ImageJ software for the measurement of diameter, area, perimeter and shape descriptors. Finally, GraphPad Prism version 8.4.2 (GraphPad Software, San Diego, CA, USA) was used for the data analysis.

3.4 3D Bioprinting

For the bioprinting of the spheroids, the BIO X 3D Version 2 – Extrusion based printer (Cellink, BICO, Gothenburg, Sweden) was used inside a class II laminar flow cabinet. For a preliminary assessment of the printability of the spheroids, they were printed using a tyramine-conjugated alginate granular ink (kindly provided from Prof. Santos group) in non-sterile conditions. Firstly, the removed spheroids were centrifuged for 1 minute at 1000 rpm and the supernatant was carefully pipetted out with a cut blue pipette tip (Figure 31B). By connecting one syringe with 2 ml of the hydrogel and one other syringe with the suspension containing the spheroids, the hydrogel and the spheroids were gently mixed several times with two syringes method, forming a homogeneous bioink (Figure 31C). The bioink was then placed into an UV-shielded cartridge inside the bioprinter. The following parameters were used: 22 Gauge nozzle, printing speed of 8 mm/second, 20% infill density, printing pressure of 30-35 kPa, and the structure selected had a 20x20x1 mm square geometry (Figure 31D).

After this test, the spheroids were printed under sterile conditions with GelMA. In this experiment, one cartridge of GelMA (Gelatine Methacryloyl, 0,25% LAP; CELLINK, BICO, Gothenburg, Sweden) was preheated to maintain the liquid state. The removed spheroids were centrifuged for 1 minute at 1000

rpm and the supernatant was carefully discarded (Figure 31B). To form the bioink, one syringe with 2 ml of GelMA and one syringe with the suspension containing the removed spheroids were mixed (Figure 31C). The bioink was then placed inside an UV-shielded cartridge. Afterwards, the cartridge was placed in a temperature controlled printhead for 15 minutes to acclimatize. The temperature used was 15°C for the printing bed and 24°C for the temperature controlled printhead. The nozzle used was 22 Gauge, the preflow delay was set at 300 ms, printing speed of 8 mm/second with 20% infill density. The starting pressure was of 18 kPa, and the structure selected had a 20x20x1 mm square geometry. UV crosslinking was performed after printing at 405 nm for 10 seconds at 5 cm of distance (Figure 31D). After having the structure fully printed, 20 ml of RPMI 1640 medium were added and the construct was incubated for 24 hours, in 5% CO_2 at 37°C.

The printability index (Pr), used to evaluate the printing resolution, was calculated through Eq. 2.2. In this equation, P is the perimeter of a square void space, considered as a region of interest (ROI), of the printed structure and A is the area of the square selected. The perimeter and area of 9 ROIs were calculated with ImageJ software. GraphPad Prism version 8.4.2 was used for the data analysis. Afterwards, the structure was cut in 4 parts with a blade and a spatula, and each quarter was moved into a 12 well-plate.

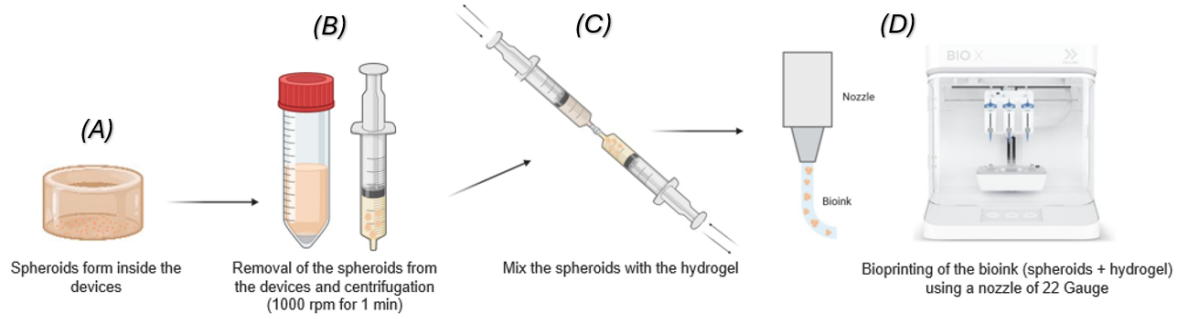


Figure 31: **Bioprinting process.**
(A) Formation of spheroids inside the agarose device; (B) Collection of the spheroids, followed by centrifugation and loading into a syringe; (C) Connection of two syringes, one containing the spheroids and the other one containing the hydrogel, and gentle mixing of the contents; (D) Loading the bioink into the bioprinter and printing the final construct.

3.5 Live/Dead assay

With the aim of assessing the spheroids cell viability after printing, the Live/Dead assay was performed at 3 different timepoints (day 1, 5 and 7). This allowed observation of the cell viability and provided a temporal assessment of the cells ability to recover and proliferate after the printing process. The working solution for the Live/Dead assay was prepared with LIVE/DEAD™ Viability/Cytotoxicity Assay

Kit (Green/Deep Red; L32250; Thermo Fisher Scientific, Waltham, MA, USA). Accordingly, the working solution consisted of 0,25 μM of SYTOX™ Deep Red Nucleic Acid Stain and 2 μM of Calcein AM diluted in pre-warmed serum-free RPMI medium. The media was removed from the well, and the construct was washed in 2ml of PBS to remove serum debris. Afterwards, 2 ml of the working solution was added, and the sample was incubated for 30 minutes in the dark with 5% CO_2 at 37°C. Lastly, the staining was removed, and pre-warmed FBS-free RPMI 1640 media was added.

For the combined spheroids, the working solution was prepared in the same way. The media was removed from the devices and 2ml of the working solution was added directly inside the devices, without removing the spheroids. The sample was incubated for 30 minutes in the dark with 5% CO_2 at 37°C. Lastly, the staining was removed, and pre-warmed FBS-free RPMI 1640 media was used to remove the spheroids from the devices and place them inside an 8-well chambered slide (Cell-culture chamber slide; Sigma-Aldrich, Merck KGaA, St. Louis, MO, USA).

3.6 DAPI and Rhodamine/Phalloidin staining

With the goal of studying the spheroids morphology and structural organization after printing and the progression through time, the DAPI and Rhodamine/Phalloidin staining was also performed at 3 different timepoints (day 1, 5 and 7). DAPI was used for the staining of the nuclei of the cells, and the Rhodamine/Phalloidin was used for the staining of actin filaments. Firstly, the cells were fixed with 3.7% paraformaldehyde (PFA) for 45 minutes, then extracted by adding 0.5% of Triton X-100 Solution (ab286840; Abcam, Cambridge, UK) and incubated for 10 minutes. The working solution of 2 μg/mL of Rhodamine phalloidin reagent (ab235138; Abcam, Cambridge, UK) and 4 μg/mL of DAPI staining solution (ab228549; Abcam, Cambridge, UK) diluted in pre-warmed RPMI medium was added and the sample was left at room temperature for 120 minutes, protected from light. Afterwards, the construct was washed 2 times in PBS for 30 minutes each time.

3.7 Fluorescence and confocal microscopy

Zeiss Celldiscoverer 7 (ZEISS, Carl Zeiss AG, Oberkochen, Germany) was used to image the constructs. For the THP-1 spheroids, fluorescence imaging of the sample was firstly performed to find the proper locations of the spheroids inside the structure, followed by confocal imaging using 5x and 10x magnifications. For the combined spheroids, since they were not bioprinted, the imaging was done inside the 8-well chamber. The locations of the spheroids were found with fluorescence imaging followed by confocal imaging using 10x magnification. The images were analysed with ImageJ software.

3.8 Statistical analysis

Data analysis and statistical testing was performed in GraphPad. Five replicate devices were used for the 0.5 million cells/mL and 1 million cells/mL densities, and two for the 2.5 million cells/mL density. The replicates correspond to the number of devices used for growing spheroids in each cell density. Only spheroids located in areas with good image quality and free from bubble interference were selected for analysis. Furthermore, only microwells containing a single spheroid were considered. Spheroids with clearly incomplete formation or overlapping with device walls were excluded, while morphologically irregular spheroids were retained in the analysis to avoid selection bias. The one-way ANOVA test and Tukey's multiple comparison test were conducted to assess differences between experimental groups. Significance levels were set at $P < 0.05$. Results were reported as mean ± standard deviation (SD) unless otherwise specified.

Chapter 4
Results

4.1 THP-1 spheroids optimization

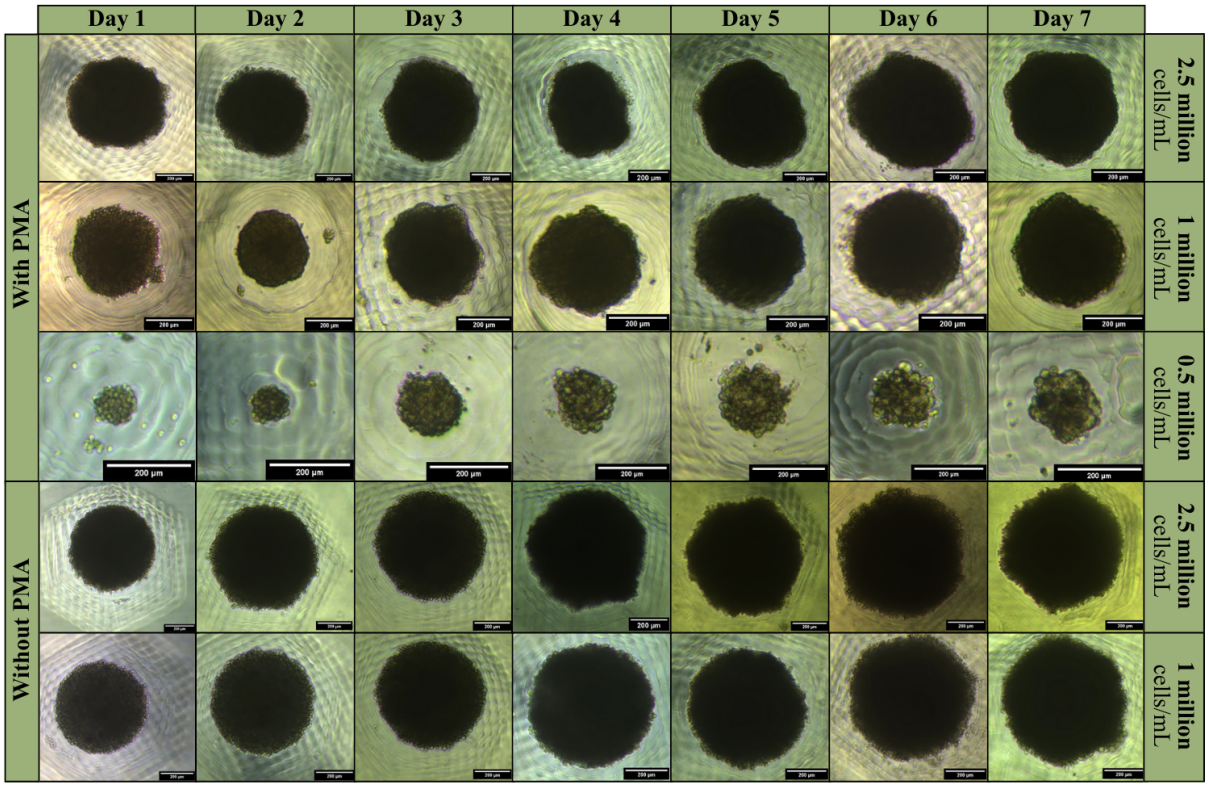


Figure 32: **Development and observation of spheroids of THP-1.**
Microscope imaging of spheroids formation from day 1 to day 7 under different conditions. The first three rows are the groups tested with PMA, the last two rows the groups without PMA. The first, second and third rows with PMA corresponds to cell densities of 0.5 million, 1 million and 2.5 million cells/mL, respectively. For the groups without PMA, the first row corresponds to 1 million cells/mL and the second to 2.5 million cells/mL. Scale bars are equal to 200 µm.

Figure 32 shows the formation of the THP-1 spheroids throughout 7 days of culture. A comparison between the groups with PMA with the ones without PMA indicates that the ones without PMA occupied most of the space of the pins of the culture devices, while the ones with PMA, even at day 7, did not fill the

entire available space. Regarding the different densities, as expected, the group with 0.5 million cells/mL presented spheroids with smaller diameters as seen in Figure 33C.

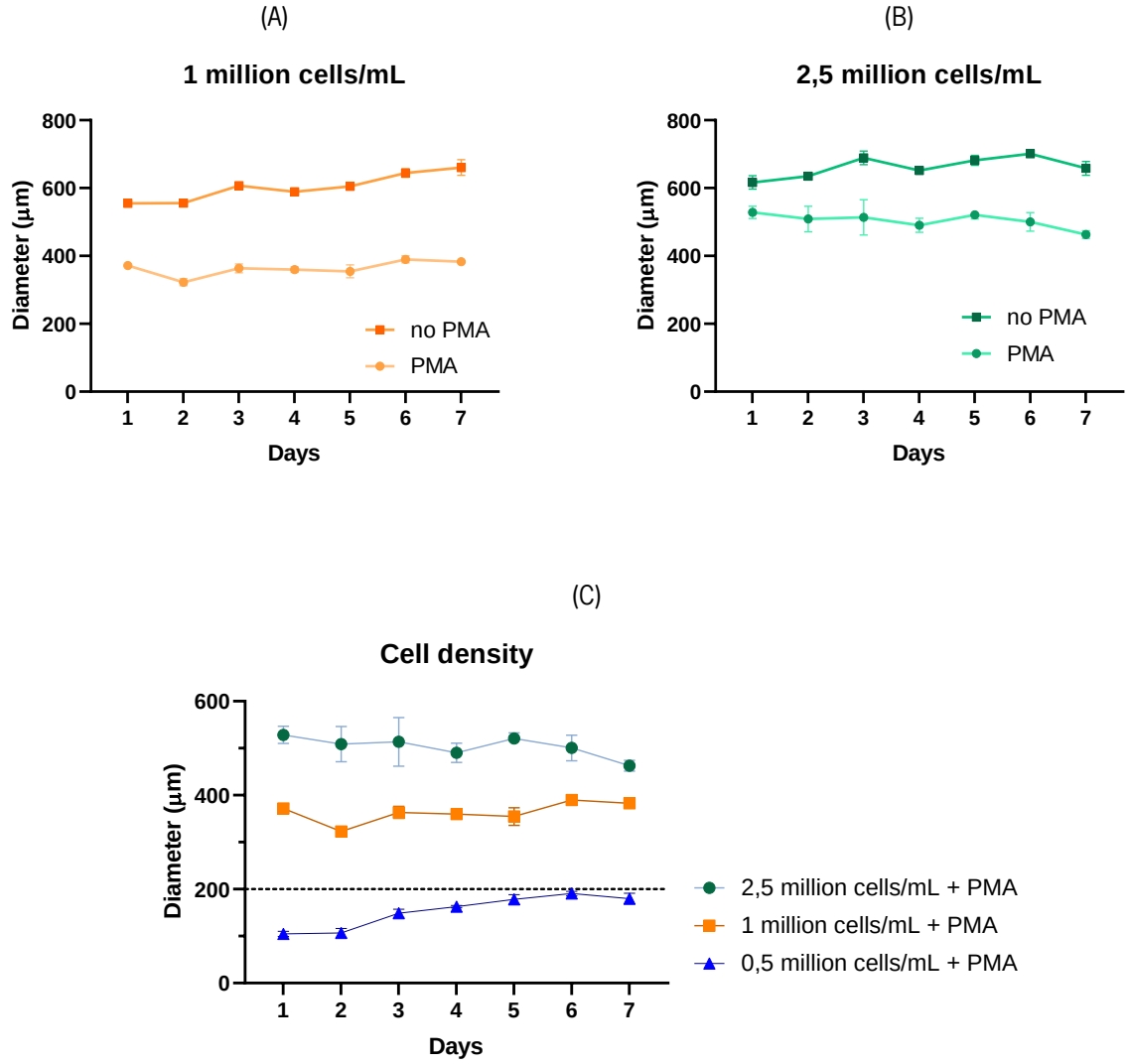


Figure 33: **Diameter comparison between spheroids of THP-1 with and without PMA at different initial cellular seeding.**
(A) Mean diameter of spheroids generated from 1 million cells/mL over 7 days of culture, with and without PMA treatment; (B) Mean diameter of spheroids generated from 2.5 million cells/mL over 7 days of culture, with and without PMA treatment; (C) Mean diameter of spheroids generated from 0.5 million, 1 million, and 2.5 million cells/mL across 7 days with PMA.

Figures 33A and 33B show the comparison between the groups with and without the addition of PMA. In both cases, the group without PMA presented a diameter around 600 µm stable over time. In the groups with PMA, the 2.5 million cells/mL group had a diameter around 500 µm, presenting a stable size with a slight decrease on day 6. Regarding the 1 million cells/mL with PMA, the diameter was similar during the seven days, measuring approximately 350 µm. Figure 33C reports the comparison of the diameters

between different cell densities. In this case, the diameter of 0.5 million cells/mL group is also presented, and reveals a diameter around 150 µm, with an increase from day 2 to day 3 and then with more stable plateaux until day 7. The dotted line in Figure 33C indicates the threshold of 200 µm, suitable for 3D bioprinting and to avoid the formation of necrotic core. Within this framework, only the 0.5 million cells/mL with PMA group diameter respected the threshold [41].

Overall, PMA treatment was essential for stable spheroid formation, and the 0.5 million cells/mL condition generated spheroids with diameters below 200 µm, making it the most suitable condition for subsequent bioprinting applications.

4.2 THP-1 spheroid structural integrity and morphological analysis

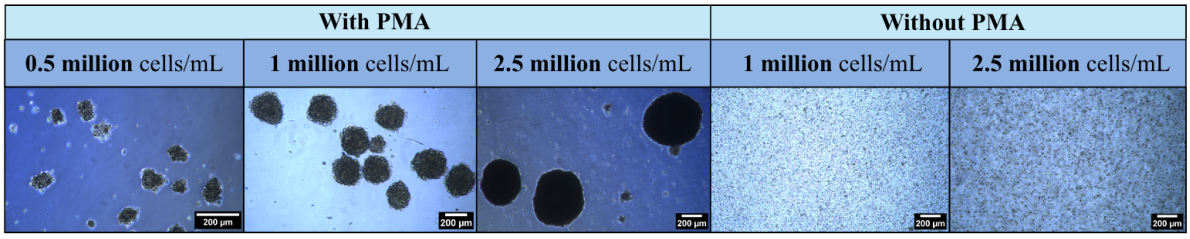


Figure 34: **Removal of the THP-1 spheroids.**
Spheroids removed at day 7 of culture, grouped according to cell density and the presence or absence of PMA. The first three columns correspond to spheroid produced with PMA and with 0.5 million, 1 million and 2.5 million cells/mL, respectively. The last two columns correspond to the removal of the spheroids without PMA and with 1 million and 2.5 million cells/mL. Scale bars are equal to 200 µm.

The data, figure 34, indicates that the groups with PMA addition were successfully removed, presenting compact structures. However, the groups without PMA disassembled upon removal, revealing single cells instead of intact spheroids.

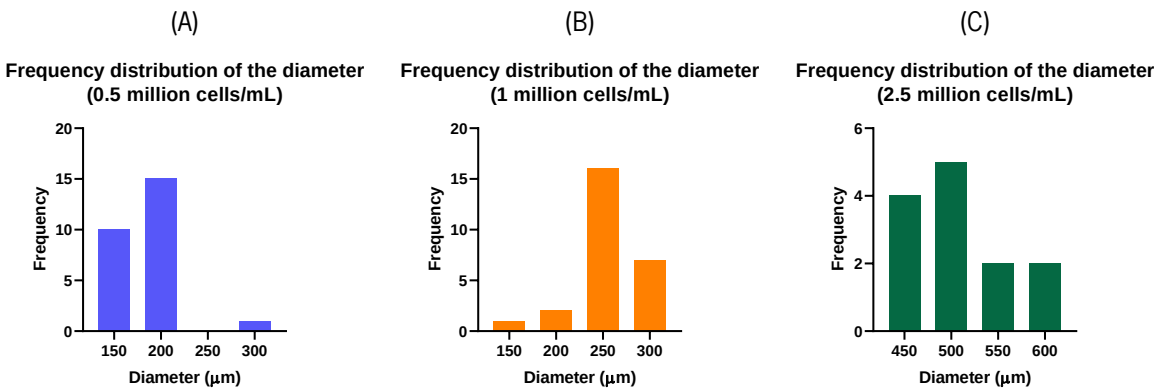


Figure 35: **Diameter distribution of the spheroids of 0.5 million, 1 million and 2.5 million cells/mL cell densities with PMA.**

(A) Frequency distribution of the diameter after removal for spheroids of 0.5 million cells/mL, 73 spheroids were measured for this analysis; (B) Frequency distribution of the diameter after removal for spheroids of 1 million cells/mL, 25 spheroids were measured for this analysis; (C) Frequency distribution of the diameter after removal for spheroids of 2.5 million cells/mL, 13 spheroids were measured for this analysis.

After the removal of the spheroids from the culture devices, their diameters were measured again. The frequency distribution of the diameters for each initial seeding density is presented in Figure 35.

For the 0.5 million cells/mL group the diameter of the spheroids after removal was 150 - 200 µm (Figure 35A). In the 1 million cells/mL the prevalence was 250 µm (Figure 35B) and for the last group, a diameter between 450 - 500 µm (Figure 35C).

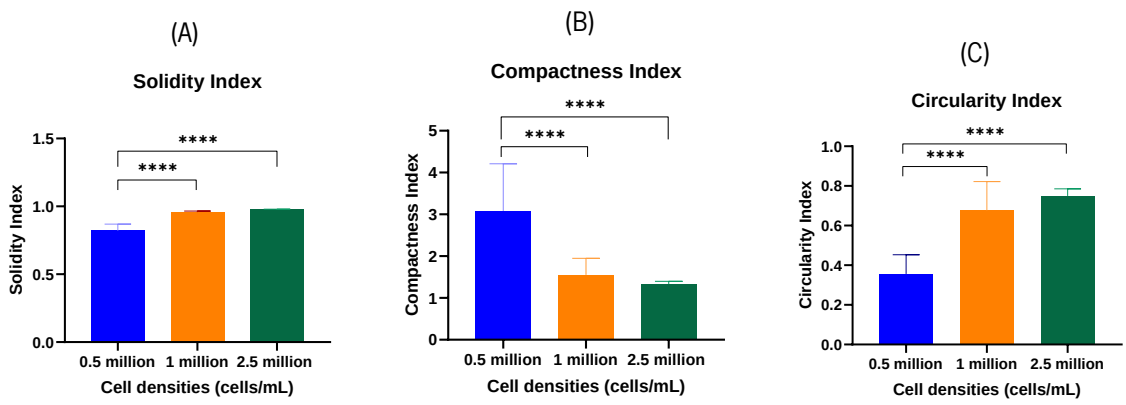


Figure 36: **Solidity, compactness, and circularity evaluation for the groups with 0.5 million, 1 million and 2.5 million cells/mL cell densities and PMA, after removal.**
(A) Solidity index from spheroids of 0.5 million, 1 million and 2.5 million cells/mL, after removal; (B) Compactness index from spheroids of 0.5 million, 1 million and 2.5 million cells/mL, after removal; (C) Circularity index from spheroids of 0.5 million, 1 million and 2.5 million cells/mL, after removal. For the 0.5 million cells/mL 26 spheroids were taken into consideration, for 1 million and 2.5 million cells/mL, 29 and 9 spheroids were considered, respectively. Significant differences were determined using the one-way ANOVA test and Tukey's multiple comparison test, with $p<0.0001$ denoted by ****.

In Figure 36A, the solidity index is reported, depicting values close to 1 in all the groups. In this case, since the indexes are around 1, the spheroids were without deformities or irregularities. Despite the 2.5 million and 1 million cells/mL groups not having a statistical difference ($p < 0.0001$, one-way ANOVA and Tukey's multiple comparison test) between them, both present a significant statistical difference ($p < 0.0001$, one-way ANOVA and Tukey's multiple comparison test) with the 0.5 million cells/mL group. This means that the solidity only varies when a lower cell density (0.5 million) is used. However, this difference might be due to the small standard deviations in the groups with higher density.

The compactness index evaluates how small the perimeter of the spheroid is when compared to the area occupied. In other words, indexes close to 1, represent well enclosed spheroids. Therefore, concerning compactness (Figure 36B) the values of the 2.5 million and 1 million cells/mL are closer to 1 while the 0.5 million cells/mL presents a higher index of 3, demonstrating again statistical difference ($p < 0.0001$, one-way ANOVA and Tukey's multiple comparison test). In this way, the 0.5 million cells/mL density presents a significantly different compactness when compared to the other two groups, which means that the difference in density provokes an impact on compactness of the spheroids.

The circularity index indicates how close the spheroid is to a perfect circle. Thus, in terms of circularity, Figure 36C, the 2.5 million cells/mL presents an index of 0.8 while the 1 million cells/mL group has a lower value of 0.7. In both cases, the values are still considered similar to 1, which means there are still

some resemblances to a perfect circle. However, the 0.5 million cells/mL group presents an index of around 0.4, suggesting again a statistical difference ($p < 0.0001$, one-way ANOVA and Tukey's multiple comparison test) from the other groups, which emphasizes the impact of a lower density on morphological aspects.

These results further support the previous section, confirming that THP-1 spheroids generated with PMA maintained their structural integrity after removal, and the 0.5 million cells/mL density provided reproducible spheroids with adequate morphology and dimensions for bioprinting despite exhibiting lower compactness and circularity.

4.3 Bioprinting

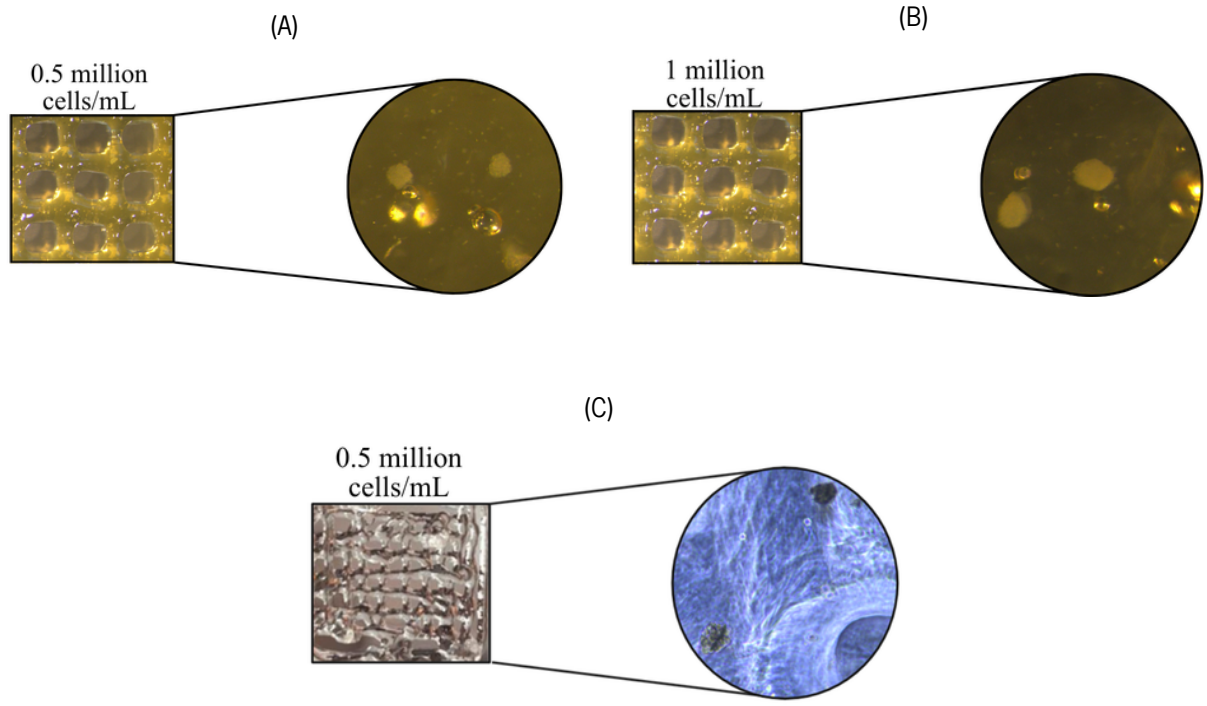


Figure 37: **Bioprinting of THP-1 spheroids with tyramine-conjugated alginate granular ink and GelMA.**
(A) Bioprinted structure with tyramine-conjugated alginate granular ink of the THP-1 spheroids with a 0.5 million cells/mL density and the spheroids within the grid shape structure. (B) Bioprinted structure with tyramine-conjugated alginate granular ink of the spheroids with a 1 million cells/mL density and the spheroids within the structure. (C) Bioprinted construct with GelMA of THP-1 spheroids with a 0.5 million cells/mL density within the grid shape structure.

As demonstrated in Figure 37A and 37B, spheroids from both 0.5 million and 1 million cells/mL densities were successfully printed using tyramine-conjugated alginate granular ink. The spheroids remained assembled and visible within the construct.

Moreover, the 0.5 million cells/mL spheroids were also successfully printed with GelMA (Figure 37C). The spheroids remained assembled within this structure.

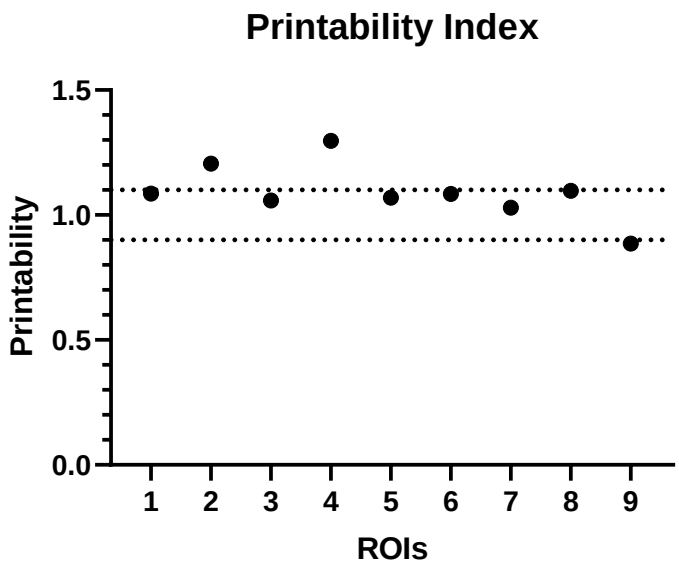


Figure 38: **Printability index of GelMA.**
Printability index evaluation of the printed structure with GelMA. 9 ROIs were considered.

The graph above displays the printability index of the construct obtained in Figure 37. The dotted lines in Figure 38 delimit the optimal range of 0.9 and 1.1. The majority of the ROIs matched the optimal range for high geometric accuracy.

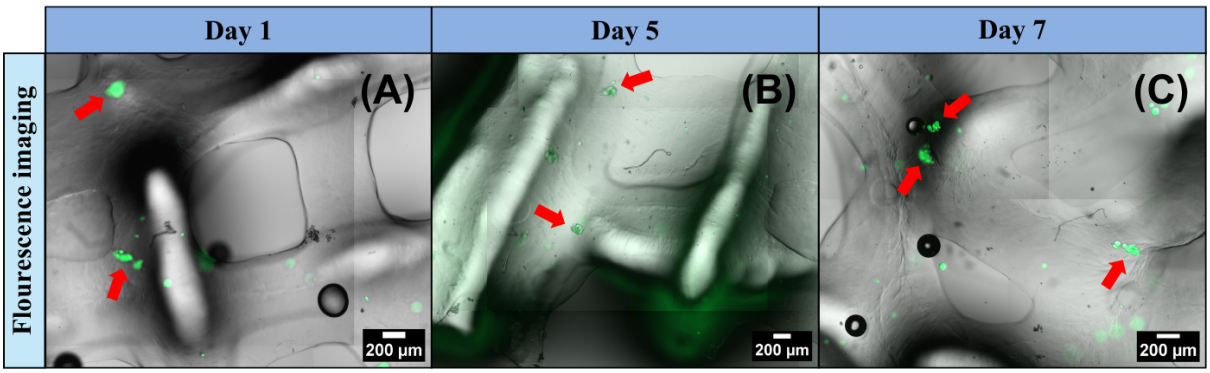


Figure 39: **Fluorescence imaging of the bioprinted constructs.**
Fluorescence imaging, with 10x magnifications, of 0.5 million cells/mL spheroids after printing with GelMA in different timepoints, day 1 (A), day 5 (B) and day 7 (C), to localise the spheroids within the structure. Red arrows point to different spheroids within the constructs. The calcein signal is shown in green. Scale bars are equal to 200 µm.

As illustrated in figure 39 fluorescence imaging enabled the identification of spheroid locations,

highlighted with the red arrows, before going with the confocal imaging. In this way, the spheroids were visible confirming their presence after printing and allowing the viability assay.

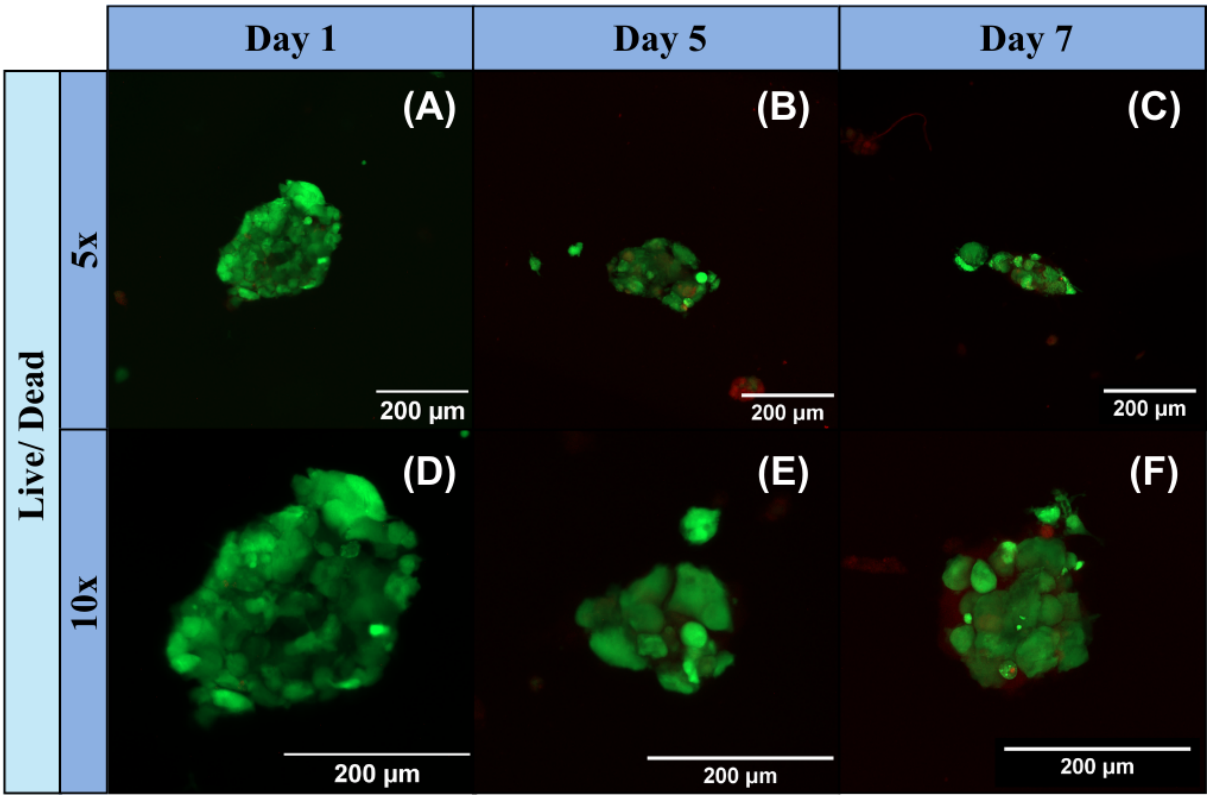


Figure 40: **Live/Dead assay of the printed THP-1 spheroids at day 1, 5 and 7.** Confocal imaging, with 5x (A, B and C) and 10x magnifications (D, E and F), of 0.5 million cells/mL spheroids after printing with GelMA in different timepoints, day 1 (A and D), day 5 (B and E) and day 7 (C and F). The green fluorescence corresponds to the calcein signal in viable cells, whereas the red signal indicates SYTOX staining in non-viable cells. Scale bars are equal to 200 µm.

Regarding the Live/Dead assay, the confocal imaging was performed on day 1, day 5 and day 7. As presented in Figure 40, the spheroids presented mainly live cells throughout the seven days of culture, without showing signs of necrotic core formation.

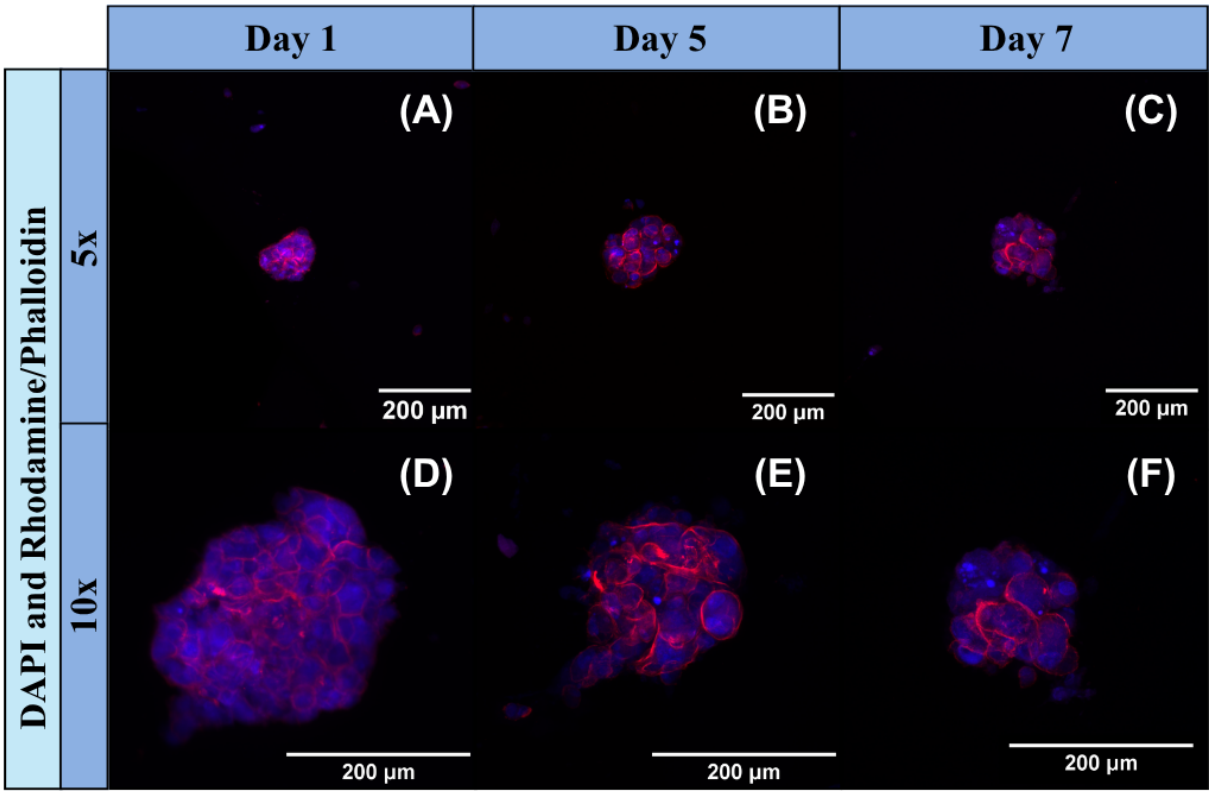


Figure 41: **DAPI and Rhodamine/Phalloidin staining of the printed spheroids at day 1, 5 and 7.** Confocal imaging, with 5x (A, B and C) and 10x magnifications (D, E and F), of 0.5 million cells/mL spheroids after printing with GelMA in different timepoints, day 1 (A and D), day 5 (B and E) and day 7 (C and F). The blue channel is for DAPI and the red channel for the filaments of actin. Scale bars are equal to 200 µm.

DAPI and Rhodamine/Phalloidin staining was performed at day 1, day 5, and day 7, to assess the morphology of the THP-1 spheroids over time. A clear trend is observed in figure 41, the nuclei (DAPI) remained regular throughout the seven days. The actin filaments (Rhodamine/Phalloidin) remained continuous and organized, although the signal was weaker on day 7.

All in all, THP-1 spheroids were successfully bioprinted while preserving their structural integrity, viability, and morphology. This demonstrates the suitability of GelMA as a bioink for spheroid-based constructs and the bioprintability of THP-1 spheroids.

4.4 THP-1 and HDF combined spheroids development

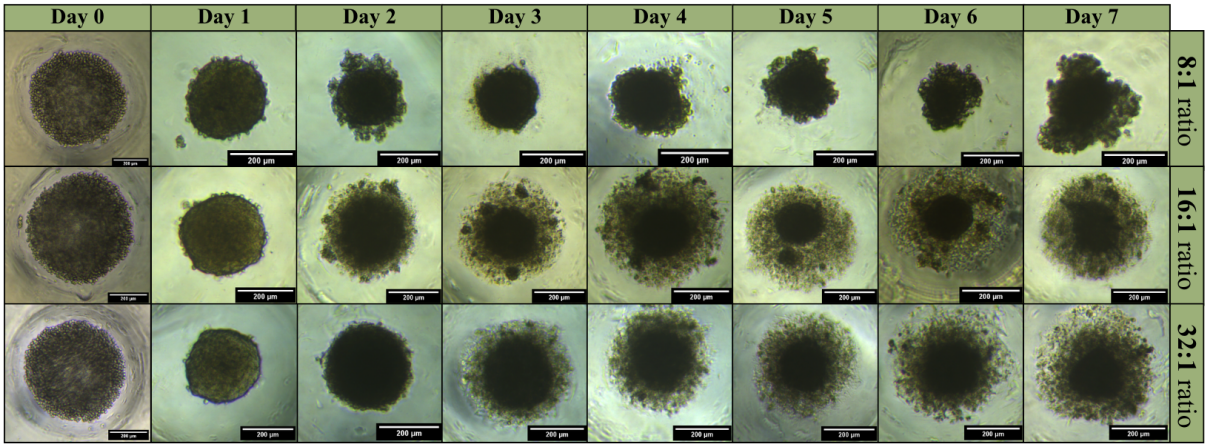


Figure 42: **Development and observation of combined spheroids of THP-1 and HDF.** Microscope imaging of spheroids formation from day 1 to day 7 with different ratios of fibroblasts and macrophages. The first row corresponds to a ratio of 8:1 ratio of fibroblasts and macrophages. The second row corresponds to 16:1 ratio. The last row is the 32:1 ratio. Scale bars are equal to 200 µm.

Figure 42 compares the development of three different ratios of fibroblasts and macrophages spheroids across seven days. Each group had a cell density of 0.5 million cells/mL with different ratios of fibroblasts and macrophages. Neither of the groups occupied the entire space of the pin of the culture device, even at day 7. However, the spheroids in all groups get progressively less regular and with debris around the center that formed a halo.

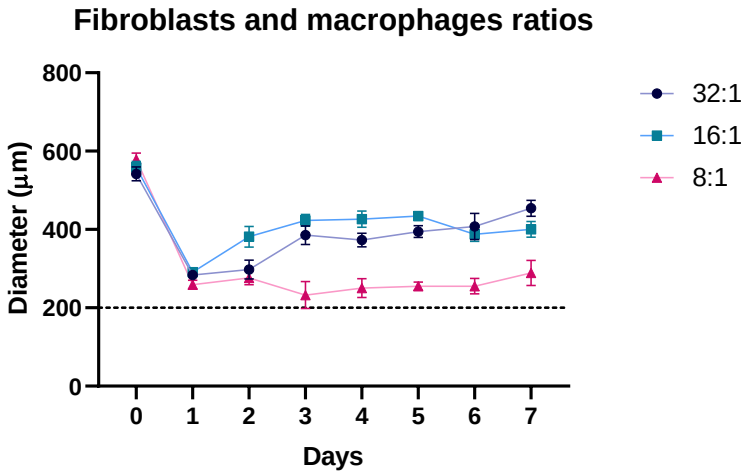


Figure 43: **Comparison of the diameters between combined spheroids of THP-1 and HDF developed with different ratios of fibroblasts and macrophages.** Mean spheroid diameter measured in spheroids formed from 8:1, 16:1 and 32:1 ratios across 7 days.

Regarding the spheroids diameter, all groups presented values above 200 µm (marked as a dotted line in Figure 43). After a decrease in diameter observed at day 1, the diameter increased until day 3 and reached a stable plateau until day 5. The group with 8:1 ratio presented a lower diameter, around 250 µm, while the other two groups presented similar diameters, around 400 µm, as seen in Figure 43.

In summary, all fibroblast-to-macrophage ratios supported combined spheroid formation, although all groups presented an irregular shape and diameters above the 200 µm mark.

4.5 THP-1 and HDF spheroids structural integrity and morphological analysis

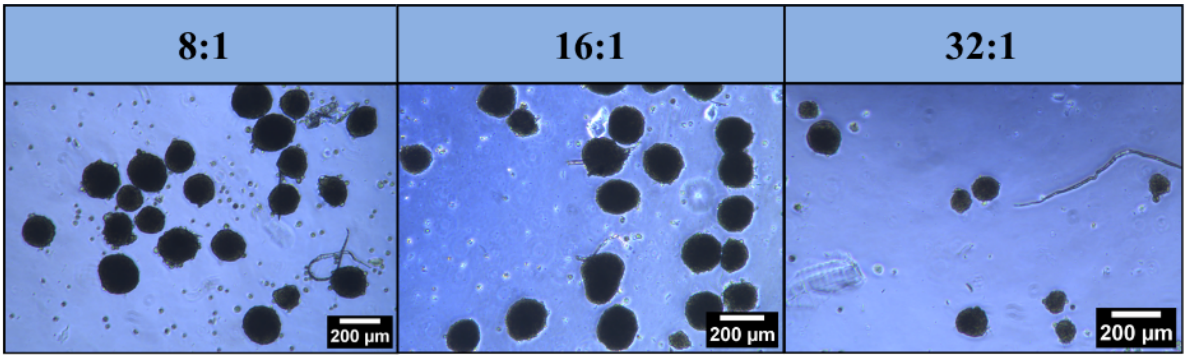


Figure 44: **Removal of combined spheroids of THP-1 and HDF.**
Spheroids removed on day 7 of the experiment, grouped according to fibroblasts and macrophages ratios. (A) Removed spheroids with 8:1 ratio. (B) Removed spheroids with 16:1 ratio. (C) Removed spheroids with 32:1 ratio. Scale bars are equal to 200 µm.

The removal of the spheroids (Figure 44) was made on day 7, for the three groups. The removal of the spheroids was possible in all ratios, revealing compact aggregated spheroids. However, the 8:1 group also displayed some single cells among the spheroids.

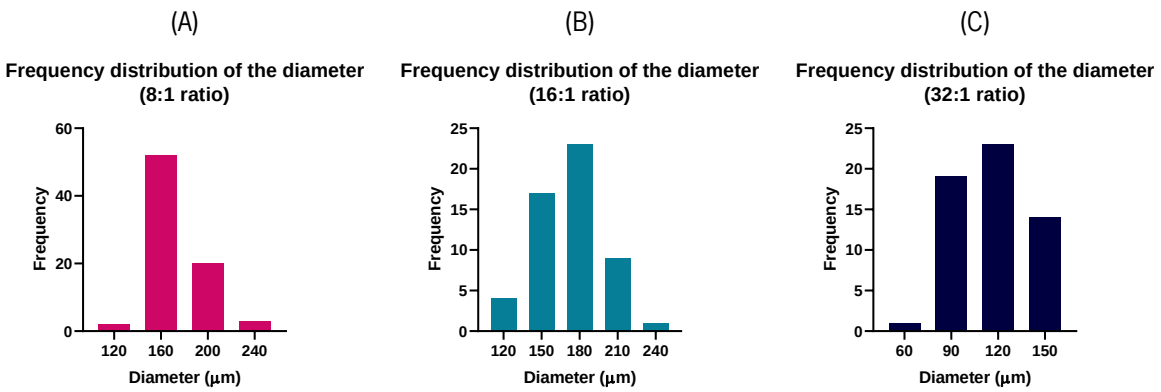


Figure 45: **Diameter distribution of the combined spheroids of THP-1 and HDF for 8:1, 16:1 and 32:1 ratio.**

(A) Frequency distribution of the diameter after removal for spheroids in 8:1 ratio of fibroblasts and macrophages, 77 spheroids were measured for this analysis; (B) Frequency distribution of the diameter after removal for spheroids in 16:1 ratio, 54 spheroids were measured for this analysis; (C) Frequency distribution of the diameter after removal for spheroids in 32:1, 57 spheroids were measured for this analysis.

After the removal of the spheroids from the culture devices, their diameters were measured again, and the frequency distribution of the diameters for each initial seeding density is presented in Figure 45. For the 8:1 group the diameter of the spheroids after removal was mainly 160 µm. In the 16:1 the prevalence was 150-180 µm and for the last group, a diameter between 90 and 120 µm.

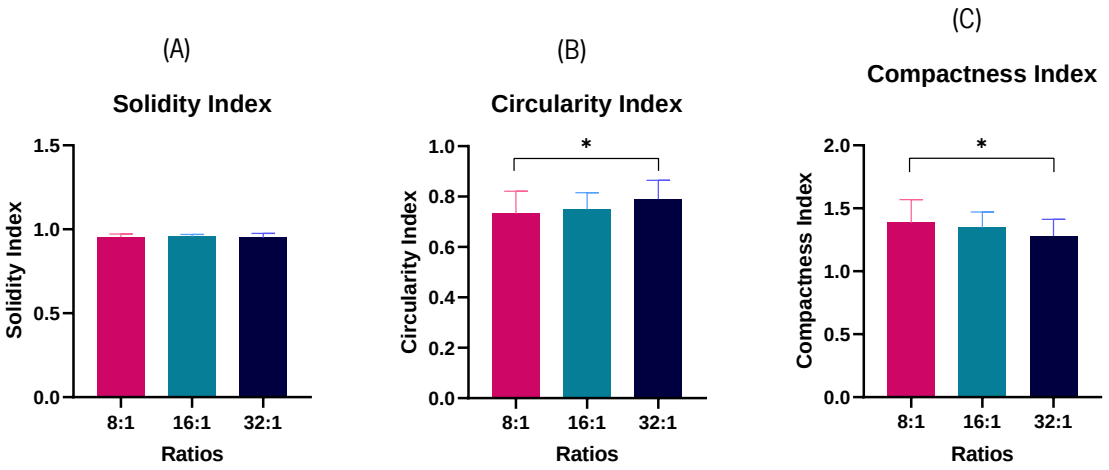


Figure 46: **Solidity, compactness, and circularity analysis for the combined spheroids of THP-1 and HDF for 8:1, 16:1 and 32:1 ratio.**

(A) Solidity index from spheroids of 8:1, 16:1 and 32:1 ratios, after removal; (B) Compactness index from spheroids of 8:1, 16:1 and 32:1 ratios, after removal; (C) Circularity index from spheroids of 8:1, 16:1 and 32:1 ratios, after removal. For the 8:1 ratio 49 spheroids were taken into consideration, for 16:1 and 32:1, 42 and 21 spheroids were considered, respectively. Significant differences were determined using the one-way ANOVA test and Tukey's multiple comparison test, with $p<0.05$ denoted by *.

In terms of morphology, the solidity, circularity and compactness indexes were again evaluated. Regarding solidity (Figure 46A), an index of 1, was clear in all groups, with no statistical difference ($p < 0.05$, one-way ANOVA and Tukey's multiple comparison test) between the groups. The circularity index (Figure 46B) was close to 0.8 for the 32:1 ratio and 0.7 for the other two, expressing statistical difference ($p < 0.05$, one-way ANOVA and Tukey's multiple comparison test) between 8:1 and 32:1 group. Finally, regarding compactness (Figure 46C), for 8:1 and 16:1 the index was close to 1.4 and 1.3 for the remaining group, which also revealed statistical difference ($p < 0.05$, one-way ANOVA and Tukey's multiple comparison test) when compared to the first group.

Overall, the combined THP-1/HDF spheroids remained intact after removal and exhibited good morphological characteristics, with smaller diameters compared to before the removal.

4.6 Viability assay of THP-1 and HDF combined spheroids

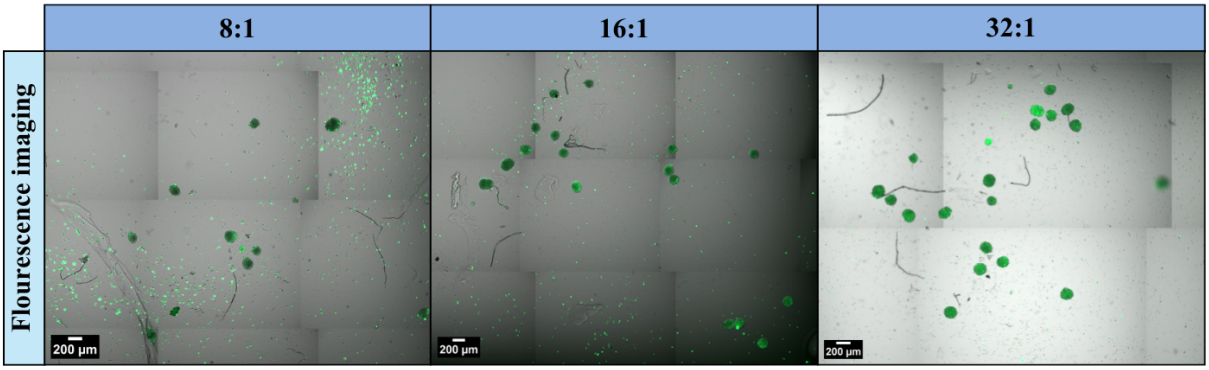


Figure 47: **Fluorescence imaging of the removed spheroids.**
(A) Fluorescence imaging, with 10x magnifications, of combined spheroids of fibroblasts and macrophages after removal with 8:1 ratio. (B) Fluorescence imaging, with 10x magnifications, of combined spheroids of fibroblasts and macrophages after removal with 16:1 ratio. (C) Fluorescence imaging, with 10x magnifications, of combined spheroids of fibroblasts and macrophages after removal with 32:1 ratio. The green fluorescence corresponds to the calcein signal in viable cells. Scale bars are equal to 200 µm.

Fluorescence pictures, Figure 47, of the removed spheroids were taken to find their location, before proceeding to confocal imaging.

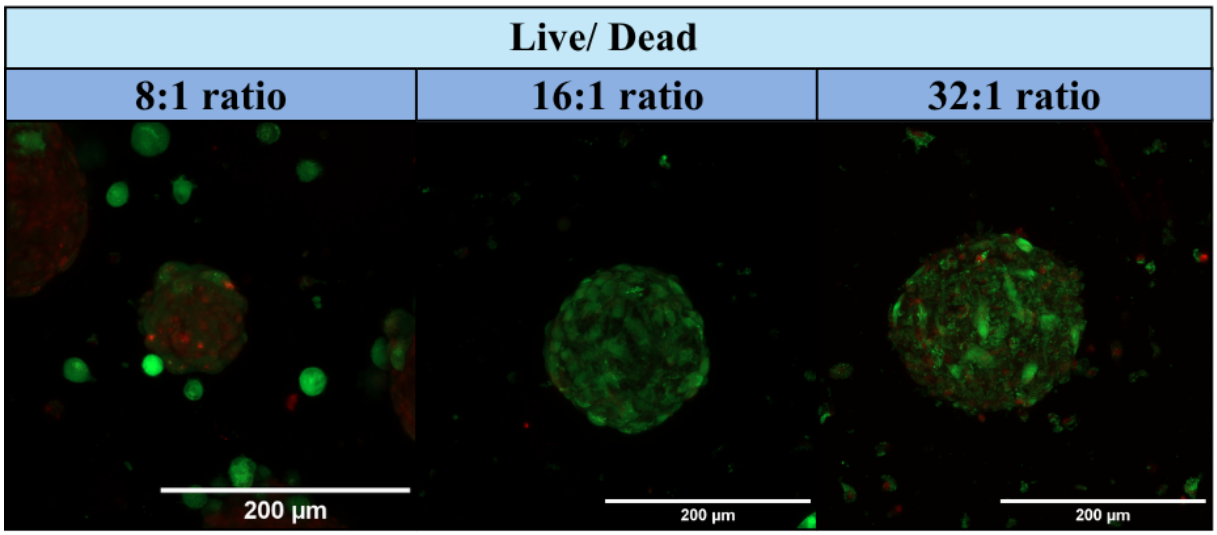


Figure 48: **Live/Dead assay of the combined spheroids after removal.**
(A) Confocal imaging, with 10x magnifications, of combined spheroids of fibroblasts and macrophages after removal with 8:1 ratio. (B) Confocal imaging, with 10x magnifications, of combined spheroids of fibroblasts and macrophages after removal with 16:1 ratio. (C) Confocal imaging, with 10x magnifications, of combined spheroids of fibroblasts and macrophages after removal with 32:1 ratio. The green fluorescence corresponds to the calcein signal in viable cells, whereas the red signal indicates SYTOX staining in non-viable cells. Scale bars are equal to 200 µm.

Considering the Live/Dead assay, the confocal imaging was performed after the removal of the spheroids from the culture devices. As seen in Figure 48, the spheroids in the 8:1 ratio present more dead cells (stained red) specially in the centre of the spheroid, indicating the formation of a necrotic core. Moreover, the presence of single cells surrounding the spheroid indicates spheroid disaggregation. The 16:1 ratio, showed both fewer dead cells and single cells. On the other hand, the 32:1 ratio indicated again more dead cells and single cells.

These results support that the 16:1 fibroblast-to-macrophage ratio exhibited the highest viability and the lowest degree of spheroid disaggregation.

Chapter 5
Discussion

5.1 THP-1 spheroids

As modern medicine extends human longevity, the prevalence of age-related degenerative conditions that require biomaterial implants capable of replacing lost biological functions continues to grow. A primary obstacle to these technologies remains the FBR, the complications of which can lead to severe health consequences and implant failure. Given the insufficiency of 2D models in capturing complex cellular communication and the fidelity gaps in current 3D methodologies, developing novel approaches is imperative.

The primary objective of this research was to engineer a reliable platform to study these immune-material interactions under biomimetic conditions. Therefore, this study focuses on the creation of a 3D bioprinted model that utilizes the structural organization of spheroids and their bioprintability to overcome barriers in reproducibility and physiological realism, allowing for a detailed investigation of the FBR within a highly controlled environment.

To achieve a robust and standardized model, a critical phase of this work involved the optimization of THP-1 spheroids. This optimization was essential not only to facilitate large-scale production but also to guarantee morphological uniformity and reproducibility, ensuring that the subsequent bioprinted constructs yielded reliable and comparable data. According to Figure 32 and 33, groups without PMA had a bigger diameter independently of the cell density used, which was in line with the results of the removal (Figure 34) since the spheroids disassembled, resulting in single cells.

This is aligned with S. Mukundan *et al.* and T. Kitaguchi *et al.* projects, which reported that PMA treatment was essential for spheroid compaction. However, both studies used ultra-low attachment plates, whereas the present work used agarose microwells, which also suggests that physical confinement and different production methods alone are insufficient to produce THP-1 spheroids [51, 52, 93]. Furthermore, S. Mukundan *et al.* reported a reduction in spheroid area following PMA treatment, consistent with the present findings. Nevertheless, they use higher PMA concentrations (up to 100 nM), whereas in this work

2 nM was sufficient to induce compaction, indicating that a smaller concentration can be used or that the agarose microwells may reduce the PMA dose required [51, 52].

In terms of cell density, it was evaluated regarding the diameter of the spheroids produced. This means that bigger cell densities create bigger spheroids, as in accordance with S. Mukundan *et al.* [52]. Although, the spheroid ideally should have a diameter smaller than 200 µm, to reduce the risk of formation of a necrotic core and prevent damage during the bioprinting step, ensuring spheroid viability [41]. This is supported by Y. Tan *et al.*, who reported apoptosis in spheroids exceeding 300 µm, attributing it to oxygen and nutrient diffusion limitations. Therefore, the importance of working with spheroids bellow that value is highlighted [54]. In addition, Y. Tan *et al.*, despite working with hybrid spheroids, uses a cell density of 0.6 million cells/mL and is able to reach spheroids with diameters smaller than 300 µm [54]. By taking this requirement into consideration the 0.5 million cells/mL cell density reveals itself as a promising number for optimal spheroids.

Regarding morphology, Decarli *et al.* presented a solidity index above 0.96 using mesenchymal stem cell spheroids in the same agarose microwell system and the same cell densities. The present work reported comparable solidity values with THP-1 cells, suggesting the device geometry drives morphological regularity regardless of cell type. [49].

Since the value is close to 1 in all groups the spheroids are considered regular and without cavities. Despite the closeness of the indexes, the 0.5 million cell/mL density is statistically different from the other two groups which might be explained by the small SD all groups present.

In terms of compactness and circularity, they represent, respectively, the relation between the area and the perimeter of the spheroid, and the closeness to a perfect circle. Therefore, the spheroids with 2.5 million and 1 million cells/mL can still be considered close to a perfect circle. In accordance to the literature, the smaller the cell density the less compact are the spheroids [61].

Yet this contrasts with Decarli *et al.*, who reported compact spheroids even at lower stem cell densities. This is likely because mesenchymal stem cells produce abundant ECM that compensates for reduced cell number, whereas THP-1 spheroids rely more on adhesion molecules, making them more sensitive to density reductions [49].

The 0.5 million cells/mL group shows a statistical difference from the other groups and has indexes farther away from 1, therefore, corroborating the idea of an elongated and irregular shape. In the work of A. del M. B. Garnique and G. M. Machado-Santelli, the spheroids, also from THP-1, showed an altered morphology, with a more elongated shape [94]. All in all, the optimization of the THP-1 spheroids was successful, especially for the purpose of bioprinting the spheroids, since they were spherical, with the

necessary size, removable without disassembling and produced in a reproducible manner.

5.2 Good printability of spheroids

Bioprinting, despite being a promising technique, still presents some challenges, especially regarding the viability of the cells, the material chosen, printability, among others. Considering the results obtained in Figure 37, the spheroids printed with tyramine-conjugated alginate granular ink maintained their structure and did not disassemble. This emphasizes how both cell densities are printable, but the 0.5 million cells/mL is still recommended to guarantee no necrotic core formation [49]. When printing with GelMA, the spheroids also remained assembled, as data indicates in Figure 37C. Regarding the Pr calculated (Figure 38), most of the ROIs are within the optimal range [69]. This index could have been improved with a better regulation of the temperature when printing. Since GelMA is very sensible to temperature, even minor thermal fluctuations or extended residence times within the cartridge directly alter the bioink's viscosity and rheological behavior. This leads to irregular extrusion flow and varying shear stress, which can negatively impact spheroid distribution and the Pr. A more precise thermal stabilization would ensure a constant flow rate, preserving the intended architecture of the 3D construct and preventing unintended voids or over-compression around the cellular spheroids.

Taking into consideration Figure 37C and 39, it is noticeable that there were very few spheroids inside each construct, however, they were visible before printing which means that a considerable amount was lost when printing. It is most likely that during the pressure test, before bioprinting, some of the spheroids were lost since they naturally deposit at the exit of the cartridge. Therefore, a better optimization of the printing procedure, as shaking the cartridge in between calibrations and tests, should be considered to avoid losing spheroids during the process.

While the viability of THP-1 spheroids post-printing remains unexplored in the literature, studies by S. Mukundan *et al.* on non-printed cultures reported a rise in cell death between days 3 and 5 [52]. This result differs from the one achieved, probably due to the method used to form the spheroids and the application of GelMA, a biocompatible material. In other methods the spheroids were cultivated together or very close to each other which may impact the viability of the spheroids. Therefore, achieving live bioprinted spheroids after 7 days was a positive result.

This is consistent with S. Villata *et al.*, who reported high viability in lung tumor spheroids bioprinted with GelMA over 18 days. Yet those spheroids were derived from epithelial cancer cell lines with strong intercellular adhesion, whereas the spheroids in this project depend on PMA for cohesion, making their survival post-printing a less predictable outcome and thus a more notable result in the present context [66].

The DAPI and rhodamine/phalloidin staining was done with the goal of further analysing the effects of the bioprinting step on the quality of the cells in the spheroids. Thus, according to Figure 41, it is visible that in every timepoint the actin filaments remained assembled in the cells in a continuous and organized manner. In addition, the nuclei also remained regular emphasizing the viability of the cells in the spheroids. Therefore, the shape remained similar across time, differing from the sprouting seen in spheroids originating from fibroblasts.

In conclusion, the spheroid production and bioprinting showed no necrotic core formation, the presence of live cells, with a regular morphology, highlighting their printability. While the bioprinting parameters require further refinement, the successful creation of printable spheroids validates the efficacy of their production protocol.

5.3 Combined spheroids

Regarding the combined spheroids, from THP-1 and HDF, there was an irregular behaviour across the 7 days of development (Figure 42) in all ratios. Especially in the 16:1 and 32:1 ratios, considerable cellular debris can be seen around the center of the spheroid, while in the 8:1 ratio an irregular border was prevalent. Regardless, the difference in diameter before the removal and after the removal indicates that this debris must have been lost in the removal and should be the reason for such a difference in the diameters calculated. For the 16:1 and 32:1 ratio the diameter drops from around 400 μm to 120 – 180 μm, obtaining a diameter suitable for printing. In case of the 8:1 ratio, the diameter before printing is lower (around 250 μm) and suffers a slight drop to 160 - 200 μm, as expected since the halo around the centre is not visible in this ratio. Despite the irregularities seen inside the devices, after removal, all ratios presented a good solidity and average circularity and compactness (Figure 46). This indicates that few cavities and irregularities were visible, but the spheroids were not perfect circles portrait a more elongated shape as seen previously in the spheroids just from THP-1.

In this case, the spheroids viability was analysed without printing and only the Live/Dead assay was performed, as seen in Figure 48. In the 8:1 ratio, some dead cells were visible specially in the core of the spheroid, increasing the possibility of having developed a necrotic core. Moreover, some alive single cells were present which goes in hand with what was observed in Figure 44A, where a lot of single cells surround the spheroids.

However, since the calcein signal appears to be weak, the dye might not have penetrated the nuclei, so it would be recommended to repeat this parameter to further understand this behaviour. Furthermore, using a higher number of macrophages might have created instability between the macrophages and the

fibroblast. In other words, the fibroblast ratio was not high enough to guarantee a regular structure, leading to the need of reducing the number of macrophages. In terms of the 16:1 ratio, there were no signals of dead cells within the spheroid and much less single cells around the spheroid. This goes in hand with what Y. Tan *et al.* observed in a similar work reporting optimal viability and structural integrity at a 16:1 fibroblast/macrophage ratio in collagen-embedded spheroids [54].

Lastly, the 32:1 ratio also presented some dead cells and single cells around the spheroids with a more disform morphology. This might have happened since it has lower number of macrophages which, consequently, limits cytokine secretion and leads to reduced deposition of collagen. As Figure 42 shows, the halo around the centre of the spheroids from the 32:1 ratio is much more disform and unorganized than the one from the 16:1 ratio, and that can be caused by lack of collagen.

Overall, the results obtained were in line with previous research's, highlighting the 16:1 ratio as the most promising. Nonetheless, further molecular characterization would be necessary to determine whether this effect is associated with changes in macrophage phenotype or ECM production. Also, since the staining was performed inside the agarose devices, the signal in the Live/Dead assay might have been weakened by it. Therefore, it would be recommended to increase the incubation time of the dyes or to perform the staining outside of the devices to get a stronger signal in the Live/Dead assay.

5.4 Study limitations

Despite the successful development of THP-1 and THP-1/HDF spheroids and incorporation of the THP-1 spheroids into bioprinted GelMA constructs, several limitations should be acknowledged.

Firstly, the number of spheroids incorporated into each bioprinted construct was relatively low. While this approach facilitated the fabrication of the construct and its morphological assessment, it may not fully reproduce the cellular density and spatial complexity observed *in vivo* during the FBR. This means that an optimized bioprinting strategy is needed to achieve the desired result.

Moreover, the developed model includes only macrophages and fibroblasts, which represents a simplified version of the FBR. Therefore, other relevant cell populations, such as neutrophyls, lymphocytes, and additional immune cell subsets, should also be considered. Consequently, the model would better capture the complexity of the cellular interactions that occur *in vivo*. In addition, it would be recommended to further investigate the possibility of integrating macrophages and fibroblasts within the model separately. In this way, instead of trying to merge them, they could be printed in the same construct along with other relevant immune cell types. Consequently, the co-culturing process could be avoided, facilitating the spheroid formation process.

Finally, the biological characterization was mainly limited to morphological and viability assessments. As no protein-level validation was performed, the macrophage phenotype could not be confirmed, preventing the determination of whether the cells predominantly exhibited M0, M1, or M2 characteristics. In addition, further investigation of the debris observed around the spheroids would be valuable to clarify its origin and potential impact on spheroid stability. Assessing the effects of PMA exposure on fibroblasts would also help to better interpret the results obtained in the co-culture spheroids. Therefore, future studies should incorporate complementary techniques, such as immunostaining, enzyme-linked immunosorbent assay (ELISA), western blotting, metabolic activity assays, and gene expression analysis, to provide a more comprehensive understanding of the cellular behaviour and biological processes occurring within the spheroids and bioprinted constructs.

Therefore, while the proposed model represents a promising platform for studying cell-cell interactions relevant to the FBR, further optimization and biological validation are required before it can fully reproduce the complexity of the *in vivo* environment.

Chapter 6
Conclusions and suggestions for further research

In this project, a 3D *in vitro* bioprinted spheroid model was established to study key cellular mechanisms related to the FBR. THP-1 spheroids were first differentiated and optimized for size, compactness, and structural integrity for bioprinting. Therefore, aggregates with diameters below 200 μm were developed, which is suitable for maintaining viability and minimizing necrotic core formation during printing. The Live/Dead assay, confirmed high cell viability after bioprinting, while DAPI and rhodamine/phalloidin staining demonstrated preserved architecture and cytoskeletal organization, highlighting the prospects of these results. Afterwards, combined THP-1 and HDF spheroids were generated, revealing that a 16:1 ratio of fibroblast-macrophages produced the most structurally robust and morphologically regular constructs, with fewer single cells and reduced necrotic core formation compared to the other ratios, as seen in the Live/Dead assay.

Having taken these results into consideration, it would be recommended to further investigate the possibility of integrating macrophages, fibroblasts and cell types involved in the FBR within the model. This inclusion allied with an optimized bioprinting process would allow for better representation of an *in vivo* reaction. Finally, a more in-depth biological validation and characterization is crucial to better understand and improve this model. Despite the positive results, it still requires a lot of work in order to obtain a more realistic, complex and useful product.

Overall, these findings show that the proposed bioprinted spheroid platform can integrate key immune cells in a controllable 3D microenvironment. This provides a promising basis for future studies on modulating the FBR and a way of improving the preclinical evaluation of biomaterials.

Bibliography

[1] U.S. Census Bureau. An Aging World: Percentage of the Population age 65+ in 2015 and 2050. Technical report, U.S. Department of Commerce, Washington, DC, USA.

[2] Kathleen B. Watson, Jennifer L. Wiltz, Kunthea Nhim, Rachel B. Kaufmann, Craig W. Thomas, and Kurt J. Greenlund. Trends in Multiple Chronic Conditions Among US Adults, By Life Stage, Behavioral Risk Factor Surveillance System, 2013–2023. *Preventing Chronic Disease*, 22:E15, April 2025. ISSN 1545-1151. doi: 10.5888/pcd22.240539.

[3] Abid Haleem, Mohd Javaid, and Ravi Pratap Singh. Exploring biomaterials for healthcare: An extensive insight into capabilities and applications. *Cure & Care*, 1(1):100003, September 2025. ISSN 30510627. doi: 10.1016/j.ccwv.2025.100003.

[4] Alejandro Carnicer-Lombarte, Shao Tuan Chen, George G. Malliaras, and Damiano G. Barone. Foreign Body Reaction to Implanted Biomaterials and Its Impact in Nerve Neuroprosthetics. *Frontiers in Bioengineering and Biotechnology*, 9:622524, April 2021. ISSN 22964185. doi: 10.3389/FBIOE.2021.622524/FULL.

[5] European Society of Cardiology. Cardiovascular Disease Statistics: Number of pacemaker Implantations. `https://eatlas.escardio.org/Atlas/ESC-Atlas-of-Cardiology`.

[6] Simone Capuani, Gulsah Malgir, Corrine Ying Xuan Chua, and Alessandro Grattoni. Advanced strategies to thwart foreign body response to implantable devices. *Bioengineering & Translational Medicine*, 7(3):e10300, March 2022. ISSN 2380-6761. doi: 10.1002/btm2.10300.

[7] Bhushan N. Kharbikar, Gauree S. Chendke, and Tejal A. Desai. Modulating the Foreign Body Response of Implants for Diabetes Treatment. *Advanced drug delivery reviews*, 174:87, July 2021. ISSN 18728294. doi: 10.1016/J.ADDR.2021.01.011.

[8] World Health Organization. Diabetes. Technical report, 2024.

[9] Lilah Fones, Amir R. Kachooei, and Pedro K. Beredjiklian. Trends in Orthopaedic Surgery on Patients 90 Years Old and Older 2014-2023. *The Archives of Bone and Joint Surgery*, 13(3):157–163, 2025. ISSN 2345-4644. doi: 10.22038/ABJS.2024.82754.3768.

[10] M. M. Morlock and M. Jäger. Endoprothetik des älteren Menschen. *Der Orthopäde*, 46(1):4–17, January 2017. ISSN 1433-0431. doi: 10.1007/s00132-016-3361-7.

[11] Yuji Sato, Noboru Kitagawa, and Akio Isobe. Current Consensus of Dental Implants in the Elderly—What Are the Limitations? *Current Oral Health Reports*, 7(3):321–326, September 2020. ISSN 2196-3002. doi: 10.1007/s40496-020-00268-0.

[12] American Joint Replacement Registry (AJRR). Annual Report 2024. Technical report, American Academy of Orthopaedic Surgeons (AAOS), 2024.

[13] Mélisande Bernard, Emile Jubeli, Michael D Pungente, and Najet Yagoubi. Biocompatibility of polymer-based biomaterials and medical devices – regulations, in vitro screening and risk-management. *Biomaterials Science*, June 2018. doi: 10.1039/c8bm00518d.

[14] Başak Şen and Banu Balcı-Peynircioğlu. Cellular models in autoinflammatory disease research. *Clinical & Translational Immunology*, 13(1):e1481, 2024. ISSN 20500068. doi: 10.1002/CTI2.1481.

[15] Nina Antunes, Banani Kundu, Subhas C. Kundu, Rui L. Reis, and Vítor Correlo. In Vitro Cancer Models: A Closer Look at Limitations on Translation. *Bioengineering*, 9(4):166, April 2022. ISSN 23065354. doi: 10.3390/BIOENGINEERING9040166.

[16] Renjian Xie, Vaibhav Pal, Yanrong Yu, Xiaolu Lu, Mengwei Gao, Shijie Liang, Miao Huang, Weijie Peng, and Ibrahim T. Ozbolat. A comprehensive review on 3D tissue models: Biofabrication technologies and preclinical applications. *Biomaterials*, 304:122408, January 2024. ISSN 01429612. doi: 10.1016/j.biomaterials.2023.122408.

[17] Andrew I. Morrison, Mirthe J. Sjoerds, Leander A. Vonk, Susan Gibbs, and Jasper J. Koning. In vitro immunity: An overview of immunocompetent organ-on-chip models. *Frontiers in Immunology*, 15: 1373186, May 2024. ISSN 1664-3224. doi: 10.3389/fimmu.2024.1373186.

[18] Jennifer B. Parker, Michelle F. Griffin, Amanda F. Spielman, Derrick C. Wan, and Michael T. Longaker. Exploring the Overlooked Roles and Mechanisms of Fibroblasts in the Foreign Body Response. *Advances in Wound Care*, 12(2):85, February 2022. ISSN 21621934. doi: 10.1089/WOUND.2022.0066.

[19] James M. Anderson, Analiz Rodriguez, and David T. Chang. FOREIGN BODY REACTION TO BIOMATERIALS. *Seminars in Immunology*, 20(2):86–100, April 2008. doi: 10.1016/j.smim.2007.11.004.

[20] Rihan Li, Dongdong Feng, Siyuan Han, Xiaoyue Zhai, Xinmiao Yu, Yuanyuan Fu, and Feng Jin. Macrophages and fibroblasts in foreign body reactions: How mechanical cues drive cell functions? *Materials Today Bio*, 22:100783, October 2023. ISSN 25900064. doi: 10.1016/j.mtbio.2023.100783.

[21] Patricia Rodríguez-Morales and Ruth A. Franklin. Macrophage phenotypes and functions: Resolving inflammation and restoring homeostasis. *Trends in Immunology*, 44(12):986–998, December 2023. ISSN 14714906. doi: 10.1016/j.it.2023.10.004.

[22] Jennifer Baum and Heather S. Duffy. Fibroblasts and Myofibroblasts: What are we talking about? *Journal of cardiovascular pharmacology*, 57(4):376, April 2011. ISSN 01602446. doi: 10.1097/FJC.0B013E3182116E39.

[23] Simone Capuani, Nathanael Hernandez, Jocelyn Nikita Campa-Carranza, Nicola Di Trani, Takuma Yoshikawa, Marco Farina, Ashley L. Joubert, Camden A. Caffey, Alessio Simeone, Seo Won Cho, Patrick S. Stayton, Corrine Ying Xuan Chua, and Alessandro Grattoni. The effect of the foreign body response on drug elution from subdermal delivery systems. *Biomaterials*, 317:123110, June 2025. ISSN 0142-9612. doi: 10.1016/j.biomaterials.2025.123110.

[24] Jan Brancewicz, Natalia Wójcik, Zuzanna Sarnowska, Julia Robak, and Magdalena Król. The Multifaceted Role of Macrophages in Biology and Diseases. *International Journal of Molecular Sciences*, 26(5):2107, March 2025. ISSN 14220067. doi: 10.3390/IJMS26052107.

[25] Uwe Lendeckel, Simone Venz, and Carmen Wolke. Macrophages: Shapes and functions. *Chemtexts*, 8(2):12, April 2022. ISSN 21993793. doi: 10.1007/S40828-022-00163-4.

[26] Phani Krishna Sudarsanam, Els C. Alsema, Nick R.M. Beijer, Theo Van Kooten, and Jan De Boer. Beyond Encapsulation: Exploring Macrophage-Fibroblast Cross Talk in Implant-Induced Fibrosis. *Tissue Engineering Part B: Reviews*, 30(6):596–606, December 2024. ISSN 1937-3368, 1937-3376. doi: 10.1089/ten.teb.2023.0300.

[27] Tiezhu Liu, Tao Huang, Jiajia Li, Aqian Li, Chuan Li, Xiaoxia Huang, Dexin Li, Shiwen Wang, and Mifang Liang. Optimization of differentiation and transcriptomic profile of THP-1 cells into macrophage by PMA. *PLoS ONE*, 18(7 July), July 2023. ISSN 19326203. doi: 10.1371/journal.pone.0286056.

[28] Maksim V. Plikus, Xiaojie Wang, Sarthak Sinha, Elvira Forte, Sean M. Thompson, Erica L. Herzog, Ryan R. Driskell, Nadia Rosenthal, Jeff Biernaskie, and Valerie Horsley. Fibroblasts: Origins, definitions, and functions in health and disease. *Cell*, 184(15):3852, July 2021. ISSN 10974172. doi: 10.1016/J.CELL.2021.06.024.

[29] European Medicines Agency. Committee for Medicinal Products for Human Use (CHMP) Committee for Medicinal Products for Veterinary Use (CVMP) Guideline on the principles of regulatory acceptance of 3Rs (replacement, reduction, refinement) testing approaches. 2016.

[30] The 3Rs. https://www.hpra.ie/regulation/scientific-animal-protection/the-3rs.

[31] Centre for Human Specific Research. 2D In Vitro Models. `https://humanspecificresearch.org/2d-in-vitro-models/`.

[32] Julia C. Fontoura, Christian Viezzer, Fabiana G. dos Santos, Rosane A. Ligabue, Ricardo Weinlich, Renato D. Puga, Dyeison Antonow, Patricia Severino, and Cristina Bonorino. Comparison of 2D and 3D cell culture models for cell growth, gene expression and drug resistance. *Materials Science and Engineering: C*, 107:110264, February 2020. ISSN 0928-4931. doi: 10.1016/J.MSEC.2019.110264.

[33] Understanding 3D In Vitro Models. https://bico.com/applications/3d-in-vitro-models/.

[34] Yae Sol Cha, Alvin Michaels, Janney Z. Wang, Yihe Niu, Yipeng Lin, Ling Zhu, Xue Zhu, Ke Wang, Michael Murray, and Fanfan Zhou. Recent advances in 3D cell culture models in cancer drug development. *Journal of Pharmaceutical Investigation*, 55(4):557–573, July 2025. ISSN 20936214. doi: 10.1007/s40005-025-00740-y.

[35] Negar Farhang Doost and Soumya K. Srivastava. A Comprehensive Review of Organ-on-a-Chip Technology and Its Applications. *Biosensors*, 14(5):225, May 2024. ISSN 20796374. doi: 10.3390/BIOS14050225.

[36] Andrea Esposito, Alessandra Ferraresi, Letizia Vallino, Beatrice Garavaglia, Danny N. Dhanasekaran, and Ciro Isidoro. Three-Dimensional In Vitro Cell Cultures as a Feasible and Promising Alternative to Two-Dimensional and Animal Models in Cancer Research. *International Journal of Biological Sciences*, 20(13):5293, 2024. ISSN 14492288. doi: 10.7150/IJBS.96469.

[37] Carolina Momoli, Beatrice Costa, Lorenzo Lenti, Matilde Tubertini, Marco Daniele Parenti, Elisa Martella, Greta Varchi, and Claudia Ferroni. The Evolution of Anticancer 3D In Vitro Models: The

Potential Role of Machine Learning and AI in the Next Generation of Animal-Free Experiments. *Cancers 2025, Vol. 17, Page 700*, 17(4):700, February 2025. ISSN 2072-6694. doi: 10.3390/CANCERS17040700.

[38] Siqi Yang, Haijie Hu, Hengchung Kung, Ruiqi Zou, Yushi Dai, Yafei Hu, Tiantian Wang, Tianrun Lv, Jun Yu, and Fuyu Li. Organoids: The current status and biomedical applications. *MedComm*, 4(3): e274, June 2023. ISSN 26882663. doi: 10.1002/MCO2.274.

[39] Tomasz Górnicki, Jakub Lambrinow, Afsaneh Golkar-Narenji, Krzysztof Data, Dominika Domagała, Julia Niebora, Maryam Farzaneh, Paul Mozdziak, Maciej Zabel, Paweł Antosik, Dorota Bukowska, Kornel Ratajczak, Marzenna Podhorska-Okołów, Piotr Dzięgiel, and Bartosz Kempisty. Biomimetic Scaffolds—A Novel Approach to Three Dimensional Cell Culture Techniques for Potential Implementation in Tissue Engineering. *Nanomaterials*, 14(6):531, March 2024. ISSN 20794991. doi: 10.3390/NANO14060531.

[40] Waad H. Abuwatfa, William G. Pitt, and Ghaleb A. Husseini. Scaffold-based 3D cell culture models in cancer research. *Journal of Biomedical Science 2024 31:1*, 31(1):7–, January 2024. ISSN 1423-0127. doi: 10.1186/S12929-024-00994-Y.

[41] Monize Caiado Decarli, Robson Amaral, Diogo Peres Dos Santos, Larissa Bueno Tofani, Eric Katayama, Rodrigo Alvarenga Rezende, Jorge Vicente Lopes Da Silva, Kamilla Swiech, Claudio Alberto Torres Suazo, Carlos Mota, Lorenzo Moroni, and Ângela Maria Moraes. Cell spheroids as a versatile research platform: Formation mechanisms, high throughput production, characterization and applications. *Biofabrication*, 13(3), July 2021. ISSN 17585090. doi: 10.1088/1758-5090/abe6f2.

[42] Kamila Białkowska, Piotr Komorowski, Maria Bryszewska, and Katarzyna Miłowska. Spheroids as a Type of Three-Dimensional Cell Cultures—Examples of Methods of Preparation and the Most Important Application. *International Journal of Molecular Sciences*, 21(17):6225, September 2020. ISSN 14220067. doi: 10.3390/IJMS21176225.

[43] Carlos Mateos-Sánchez, Beatriz González, Gisela de Miguel-García, Aida Font-Cugat, Iris Marcote-Corral, and Sergio Alonso. Comparative analysis of 3D-culture techniques for multicellular colorectal tumour spheroids and development of a novel SW48 3D-model. *Scientific Reports*, 15(1), December 2025. ISSN 20452322. doi: 10.1038/S41598-025-13588-X.

[44] Parul Benien and Archana Swami. 3D tumor models: History, advances and future perspectives. *Future Oncology*, 10(7):1311–1327, 2014. ISSN 17448301. doi: 10.2217/FON.13.274.

[45] Na Eun Ryu, Soo Hong Lee, and Hansoo Park. Spheroid Culture System Methods and Applications for Mesenchymal Stem Cells. *Cells*, 8(12):1620, December 2019. ISSN 20734409. doi: 10.3390/CELLS8121620.

[46] Juliana Trindade Caleffi, Mirian Carolini Esgoti Aal, Helena de Oliveira Manacorda Gallindo, Gabriel Henrique Caxali, Bruno Pereira Crulhas, Amanda Oliveira Ribeiro, Glauco R. Souza, and Flávia Karina Delella. Magnetic 3D cell culture: State of the art and current advances. *Life Sciences*, 286:120028, December 2021. ISSN 0024-3205. doi: 10.1016/J.LFS.2021.120028.

[47] Christoph Eilenberger, Mario Rothbauer, Florian Selinger, Anna Gerhartl, Christian Jordan, Michael Harasek, Barbara Schädl, Johannes Grillari, Julian Weghuber, Winfried Neuhaus, Seta Küpcü, and Peter Ertl. A Microfluidic Multisize Spheroid Array for Multiparametric Screening of Anticancer Drugs and Blood–Brain Barrier Transport Properties. *Advanced Science*, 8(11):2004856, June 2021. ISSN 21983844. doi: 10.1002/ADVS.202004856;WGROUP:STRING:PUBLICATION.

[48] Eileen Reidy, Niamh A. Leonard, Oliver Treacy, and Aideen E. Ryan. A 3D view of colorectal cancer models in predicting therapeutic responses and resistance. *Cancers*, 13(2):1–22, January 2021. ISSN 20726694. doi: 10.3390/CANCERS13020227.

[49] Monize Caiado Decarli, Mateus Vidigal de Castro, Júlia Adami Nogueira, Mariana Harue T. Nagahara, Cecília Buzatto Westin, Alexandre Leite R. de Oliveira, Jorge Vicente L. da Silva, Lorenzo Moroni, Carlos Mota, and Ângela Maria Moraes. Development of a device useful to reproducibly produce large quantities of viable and uniform stem cell spheroids with controlled diameters. *Biomaterials Advances*, 135, April 2022. ISSN 27729508. doi: 10.1016/j.msec.2022.112685.

[50] Baiyang Sun, Zihe Liang, Yupeng Wang, Yue Yu, Xiaobing Zhou, Xingchao Geng, and Bo Li. A 3D spheroid model of quadruple cell co-culture with improved liver functions for hepatotoxicity prediction. *Toxicology*, 505, June 2024. ISSN 18793185. doi: 10.1016/j.tox.2024.153829.

[51] Shilpaa Mukundan, Rachana Bhatt, John Lucas, Matthew Tereyek, Theresa L. Chang, Selvakumar Subbian, and Biju Parekkadan. 3D host cell and pathogen-based bioassay development for testing anti-tuberculosis (TB) drug response and modeling immunodeficiency. *Biomolecular Concepts*, 12 (1):117–128, January 2021. ISSN 1868503X. doi: 10.1515/bmc-2021-0013.

[52] Shilpaa Mukundan, Pooja Singh, Aditi Shah, Ranjeet Kumar, Kelly C. O'neill, Claire L. Carter, David G. Russell, Selvakumar Subbian, and Biju Parekkadan. In vitro miniaturized tuberculosis spheroid model. *Biomedicines*, 9(9), September 2021. ISSN 22279059. doi: 10.3390/biomedicines9091209.

[53] So Dam Jang, Jeeyeun Song, Hyun Ah Kim, Chang Nim Im, Iftikhar Ali Khawar, Jong Kook Park, and Hyo Jeong Kuh. Anti-cancer activity profiling of chemotherapeutic agents in 3D co-cultures of pancreatic tumor spheroids with cancer- associated fibroblasts and macrophages. *Cancers*, 13(23), December 2021. ISSN 20726694. doi: 10.3390/cancers13235955.

[54] Yu Tan, Allister Suarez, Matthew Garza, Aadil A. Khan, Jennifer Elisseeff, and Devin Coon. Human fibroblast-macrophage tissue spheroids demonstrate ratio-dependent fibrotic activity for: In vitro fibrogenesis model development. *Biomaterials Science*, 8(7):1951–1960, April 2020. ISSN 20474849. doi: 10.1039/c9bm00900k.

[55] Laura Mendoza-Cerezo, Jesús M. Rodríguez-Rego, Antonio Macías-García, Alfonso C. Marcos-Romero, and Antonio Díaz-Parralejo. Evolution of bioprinting and current applications. *International Journal of Bioprinting*, 9(4):742, 2023. ISSN 24248002. doi: 10.18063/IJB.742.

[56] Alessandra Dellaquila, Chau Le Bao, Didier Letourneur, and Teresa Simon-Yarza. In Vitro Strategies to Vascularize 3D Physiologically Relevant Models. *Advanced Science*, 8(19):2100798, October 2021. ISSN 21983844. doi: 10.1002/ADVS.202100798.

[57] Jessica Hoarau-Véchot, Arash Rafii, Cyril Touboul, and Jennifer Pasquier. Halfway between 2D and Animal Models: Are 3D Cultures the Ideal Tool to Study Cancer-Microenvironment Interactions? *International Journal of Molecular Sciences*, 19(1):181, January 2018. ISSN 14220067. doi: 10.3390/IJMS19010181.

[58] Jianhua Zhang, Esther Wehrle, Marina Rubert, and Ralph Müller. 3D Bioprinting of Human Tissues: Biofabrication, Bioinks, and Bioreactors. *International Journal of Molecular Sciences*, 22(8):3971, April 2021. ISSN 14220067. doi: 10.3390/IJMS22083971.

[59] Min Tang, Jeremy N. Rich, and Shaochen Chen. Biomaterials and 3D Bioprinting Strategies to Model Glioblastoma and Blood-Brain Barrier. *Advanced materials (Deerfield Beach, Fla.)*, 33(5):e2004776, February 2021. ISSN 0935-9648. doi: 10.1002/adma.202004776.

[60] Ekaterina D. Minaeva, Artem A. Antoshin, Nastasia V. Kosheleva, Polina I. Koteneva, Sergey A. Gonchukov, Svetlana I. Tsypina, Vladimir I. Yusupov, Peter S. Timashev, and Nikita V. Minaev. Laser Bioprinting with Cell Spheroids: Accurate and Gentle. 14(6):1152. ISSN 2072-666X. doi: 10.3390/mi14061152.

[61] Dishary Banerjee, Yogendra Pratap Singh, Pallab Datta, Veli Ozbolat, Aaron O'Donnell, Miji Yeo, and Ibrahim T. Ozbolat. Strategies for 3D bioprinting of spheroids: A comprehensive review. *Biomaterials*, 291, December 2022. ISSN 18785905. doi: 10.1016/j.biomaterials.2022.121881.

[62] Xiaoling Yu, Tian Zhang, and Yuan Li. 3D Printing and Bioprinting Nerve Conduits for Neural Tissue Engineering. *Polymers*, 12:1637, July 2020. doi: 10.3390/polym12081637.

[63] Bugra Ayan, Dong Nyoung Heo, Zhifeng Zhang, Madhuri Dey, Adomas Povilianskas, Corina Drapaca, and Ibrahim T. Ozbolat. Aspiration-assisted bioprinting for precise positioning of biologics. 6(10): eaaw5111. ISSN 2375-2548. doi: 10.1126/sciadv.aaw5111.

[64] Maedeh Rahimnejad, Narges Nasrollahi Boroujeni, Sepideh Jahangiri, Navid Rabiee, Mohammad Rabiee, Pooyan Makvandi, Omid Akhavan, and Rajender S. Varma. Prevascularized Micro-/Nano-Sized Spheroid/Bead Aggregates for Vascular Tissue Engineering. *Nano-Micro Letters*, 13(1):182, December 2021. ISSN 21505551. doi: 10.1007/S40820-021-00697-1.

[65] Andrew M. Blakely, Kali L. Manning, Anubhav Tripathi, and Jeffrey R. Morgan. Bio-Pick, Place, and Perfuse: A New Instrument for Three-Dimensional Tissue Engineering. *Tissue Engineering. Part C, Methods*, 21(7):737–746, July 2015. ISSN 1937-3392. doi: 10.1089/ten.TEC.2014.0439.

[66] Simona Villata, Marta Canta, Désirée Baruffaldi, Ignazio Roppolo, Candido Fabrizio Pirri, and Francesca Frascella. 3D bioprinted GelMA platform for the production of lung tumor spheroids. *Bioprinting*, 36: e00310, December 2023. ISSN 2405-8866. doi: 10.1016/j.bprint.2023.e00310.

[67] Kaivalya A. Deo, Kanwar Abhay Singh, Charles W. Peak, Daniel L. Alge, and Akhilesh K. Gaharwar. Bioprinting 101: Design, Fabrication, and Evaluation of Cell-Laden 3D Bioprinted Scaffolds. *Tissue Engineering. Part A*, 26(5-6):318–338, March 2020. ISSN 1937-335X. doi: 10.1089/ten.TEA.2019.0298.

[68] A. Yahia, S. Mantellato, and Robert J. Flatt. Concrete rheology: A basis for understanding chemical admixtures. *Science and Technology of Concrete Admixtures*, pages 97–127, 2016. doi: 10.1016/B978-0-08-100693-1.00007-2.

[69] Jennika Karvinen and Minna Kellomäki. Design aspects and characterization of hydrogel-based bioinks for extrusion-based bioprinting. *Bioprinting*, 32:e00274, July 2023. ISSN 2405-8866. doi: 10.1016/j.bprint.2023.e00274.

[70] Vivian H. M. Mouser, Ferry P.W. Melchels, Jetze Visser, Wouter J.A. Dhert, Debby Gawlitta, and Jos Malda. Yield stress determines bioprintability of hydrogels based on gelatin-methacryloyl and gellan gum for cartilage bioprinting. *Biofabrication*, 8(3):035003, September 2016. ISSN 1758-5082. doi: 10.1088/1758-5090/8/3/035003.

[71] Srikanthan Ramesh, Ola L. A. Harrysson, Prahalada K. Rao, Ali Tamayol, Denis R. Cormier, Yunbo Zhang, and Iris V. Rivero. Extrusion bioprinting: Recent progress, challenges, and future opportunities. *Bioprinting*, 21:e00116, March 2021. ISSN 2405-8866. doi: 10.1016/j.bprint.2020.e00116.

[72] Andrea Schwab, Riccardo Levato, Matteo D'Este, Susanna Piluso, David Eglin, and Jos Malda. Printability and Shape Fidelity of Bioinks in 3D Bioprinting. *Chemical Reviews*, 120(19):11028–11055, October 2020. ISSN 15206890. doi: 10.1021/acs.chemrev.0c00084.

[73] P. A. Amorim, M. A. d'Ávila, R. Anand, P. Moldenaers, P. Van Puyvelde, and V. Bloemen. Insights on shear rheology of inks for extrusion-based 3D bioprinting. *Bioprinting*, 22:e00129, June 2021. ISSN 2405-8866. doi: 10.1016/j.bprint.2021.e00129.

[74] Slesha Tuladhar, Scott Clark, and Ahasan Habib. Tuning Shear Thinning Factors of 3D Bio-Printable Hydrogels Using Short Fiber. *Materials*, 16(2):572, January 2023. ISSN 19961944. doi: 10.3390/MA16020572.

[75] Yavuz Ertas, Asma Vaziri, Keyvan Abedi Dorcheh, Fereshteh Kazemi-Aghdam, Masoume Sohrabinejad, Rumeysa Tutar, Fatemeh Rastegar Adib, and Nureddin Ashammakhi. Ian Situ Tissue Engineering: A New Dimension. pages 325–350. October 2021. ISBN 978-981-16-4419-1. doi: 10.1007/978-981-16-4420-7_13.

[76] Amin GhavamiNejad, Nureddin Ashammakhi, Xiao Yu Wu, and Ali Khademhosseini. Crosslinking Strategies for Three-Dimensional Bioprinting of Polymeric Hydrogels. *Small (Weinheim an der Bergstrasse, Germany)*, 16(35):e2002931, September 2020. ISSN 16136829. doi: 10.1002/SMLL.202002931.

[77] Subrata Das and Gayathri Natarajan. Silk fiber composites in biomedical applications. *Materials for Biomedical Engineering: Biopolymer Fibers*, pages 309–338, January 2019. doi: 10.1016/B978-0-12-816872-1.00011-X.

[78] Roghayeh Khoeini, Hamed Nosrati, Abolfazl Akbarzadeh, Aziz Eftekhari, Taras Kavetskyy, Rovshan Khalilov, Elham Ahmadian, Aygun Nasibova, Pallab Datta, Leila Roshangar, Dante C. Deluca, Sood-

abeh Davaran, Magali Cucchiarini, and Ibrahim T. Ozbolat. Natural and Synthetic Bioinks for 3D Bioprinting. *Advanced NanoBiomed Research*, 1(8):2000097, 2021. ISSN 2699-9307. doi: 10.1002/anbr.202000097.

[79] Claire Benwood, Josie Chrenek, Rebecca L. Kirsch, Nadia Z. Masri, Hannah Richards, Kyra Teetzen, and Stephanie M. Willerth. Natural Biomaterials and Their Use as Bioinks for Printing Tissues. *Bioengineering*, 8(2):27, February 2021. ISSN 2306-5354. doi: 10.3390/bioengineering8020027.

[80] P. Selcan Gungor-Ozkerim, Ilyas Inci, Yu Shrike Zhang, Ali Khademhosseini, and Mehmet Remzi Dokmeci. Bioinks for 3D bioprinting: An overview. *Biomaterials science*, 6(5):915, May 2018. ISSN 20474849. doi: 10.1039/C7BM00765E.

[81] Jana Stepanovska, Monika Supova, Karel Hanzalek, Antonin Broz, and Roman Matejka. Collagen Bioinks for Bioprinting: A Systematic Review of Hydrogel Properties, Bioprinting Parameters, Protocols, and Bioprinted Structure Characteristics. *Biomedicines*, 9(9):1137, September 2021. ISSN 22279059. doi: 10.3390/BIOMEDICINES9091137.

[82] Saad Asim, Tanveer A. Tabish, Usman Liaqat, Ibrahim T. Ozbolat, and Muhammad Rizwan. Advances in gelatin bioinks to optimize bioprinted cell functions. *Advanced healthcare materials*, 12(17): e2203148, July 2023. ISSN 2192-2640. doi: 10.1002/adhm.202203148.

[83] Bioink Selection for 3D Bioprinting. https://www.sigmaaldrich.com/NL/en/technical-documents/technical-article/cell-culture-and-cell-culture-analysis/3d-cell-culture/3d-bioprinting-bioinks.

[84] Anushree Nagaraj, Alaitz Etxeberria, Rafea Naffa, Ghada Zidan, and Ali Seyfoddin. 3D-Printed Hybrid Collagen/GelMA Hydrogels for Tissue Engineering Applications. *Biology*, 11:1561, October 2022. doi: 10.3390/biology11111561.

[85] Mingyue Sun, Xiaoting Sun, Ziyuan Wang, Shuyu Guo, Guangjiao Yu, and Huazhe Yang. Synthesis and Properties of Gelatin Methacryloyl (GelMA) Hydrogels and Their Recent Applications in Load-Bearing Tissue. *Polymers*, 10(11):1290, 2018. ISSN 20734360. doi: 10.3390/POLYM10111290.

[86] Laura Mendoza-Cerezo, Jesús M. Rodríguez-Rego, Antonio Macías-García, Antuca Callejas-Marín, Luís Sánchez-Guardado, and Alfonso C. Marcos-Romero. Three-Dimensional Bioprinting of GelMA Hydrogels with Culture Medium: Balancing Printability, Rheology and Cell Viability for Tissue Regeneration. *Polymers*, 16(10):1437, May 2024. ISSN 20734360. doi: 10.3390/POLYM16101437.

[87] Mariangela Rea, Luana Di Lisa, Giorgia Pagnotta, Nunzia Gallo, Luca Salvatore, Federica D'Amico, Noelia Campilio, José Manuel Baena, Juan Antonio Marchal, Arrigo F. G. Cicero, Claudio Borghi, and Maria Letizia Focarete. Establishing a Bioink Assessment Protocol: GelMA and Collagen in the Bioprinting of a Potential In Vitro Intestinal Model. *ACS Biomaterials Science & Engineering*, 11(4): 2456–2467, April 2025. ISSN 23739878. doi: 10.1021/ACSBIOMATERIALS.5C00034.

[88] CELLINK AB. Specification Sheet: GelMA Bioink LAP 0.25%, 2021.

[89] CELLINK AB. Bioprinting Protocol: GelMA Bioink, 2023.

[90] Nimal Raveendran, Kanchan Vaswani, Pingping Han, Saraswat Basu, Corey S. Moran, and Sašo Ivanovski. Modeling inflammatory response using 3D bioprinting of polarized macrophages. *International Journal of Bioprinting*, 10(2):398–412, 2024. ISSN 24248002. doi: 10.36922/IJB.2116.

[91] Monize Caiado Decarli, Adrián Seijas-Gamardo, Francis L. C. Morgan, Paul Wieringa, Matthew B. Baker, Jorge Vicente L. Silva, Ângela Maria Moraes, Lorenzo Moroni, and Carlos Mota. Bioprinting of Stem Cell Spheroids Followed by Post-Printing Chondrogenic Differentiation for Cartilage Tissue Engineering. *Advanced Healthcare Materials*, 12(19):2203021, July 2023. ISSN 21922659. doi: 10.1002/ADHM.202203021;WGROUP:STRING:PUBLICATION.

[92] Lise De Moor, Sélina Fernandez, Chris Vercruysse, Liesbeth Tytgat, Mahtab Asadian, Nathalie De Geyter, Sandra Van Vlierberghe, Peter Dubruel, and Heidi Declercq. Hybrid Bioprinting of Chondrogenically Induced Human Mesenchymal Stem Cell Spheroids. *Frontiers in Bioengineering and Biotechnology*, 8:526351, May 2020. ISSN 22964185. doi: 10.3389/FBIOE.2020.00484/BIBTEX.

[93] Takanori Kitaguchi, Taichi Matsumoto, Kazumasa Yoshida, Yuriko Hamaguchi, Gen Maruta, Hisanori Maeoka, Shuhei Ishikura, Michitaka Nakano, Yusuke Ishida, Fumihito Hirai, Mikiko Aoki, Shohta Kodama, Senji Shirasawa, and Toshiyuki Tsunoda. Inhibitory Effect of Pyra–Metho–Carnil on the Differentiation and Maturation of Macrophages in Normal and Cancer Microenvironments. *Anticancer Research*, 44(8):3557–3565, August 2024. ISSN 0250-7005, 1791-7530. doi: 10.21873/anticanres.17178.

[94] Anali del Milagro Bernabe Garnique and Glaucia Maria Machado-Santelli. Characterization of 3D NSCLC Cell Cultures with Fibroblasts or Macrophages for Tumor Microenvironment Studies and Chemotherapy Screening. *Cells*, 12(24):2790, January 2023. ISSN 2073-4409. doi: 10.3390/cells12242790.